Computer Simulations of Martensitic Transition in Zirconium

Udomsilp Pinsook

A thesis submitted in fulfilment of the requirements
for the degree of Doctor of Philosophy
to the
University of Edinburgh
1999

Mommy, I love you.

Abstract

The martensitic transition in zirconium is a first order solid-to-solid transition which transforms from body-centred-cubic (bcc) to hexagonal close-packed (hcp) structure. By using a Finnis-Sinclair type many-body interatomic potential derived for zirconium and molecular dynamics (MD) methods, a large number of simulations have been studied with the implementation of Nosé-Hoover thermostat and Parrinello-Rahman scheme. We found that the transition is a result of the instability of a transverse N-point phonon in the bcc lattice which can be stabilised by the large fluctuation of the anharmonic effect above the transition temperature via extra vibrational entropy. The transition temperature in our calculations is 1,333K. With the concept of 'local atomic structure', the microstructure can be studied at the atomic level. The kinetics of the transition is dominated by the strain energy. Stripes of $(10\bar{1}1)$ twins are formed as a consequence. The twins contain some stacking faults. Stacking faults cause steps in the twin boundary. After the martensitic microstructure is deformed, we found that the twinning deformation occurs by the aid of the 'twin boundary steps' and their associated stacking faults, and the interchange of neighbouring atoms. The interchange of neighbouring atoms leads to the term 'plastic atoms'. We believe that these plastic atoms cause a microscopic irreversible process and the absence of the shape memory effect in zirconium.

Acknowledgement

I would like to thank my best supervisor ever Dr. Graeme Ackland for his enthusiastic and invaluable guidance.

Many thanks to Eleanor McKirdy for being the best secretary in the world and Liz McIvor for a lot of helps. Thousands thanks to Stewart Reed for reading and correcting the draft of my thesis.

Thanks to Thai friends, Ajarn Gorn&p'Hnoi, p'Tui, p'Ting, p'Pao&p'Eaw, na Kiem, p'Mui, p'Jo, p'Ped, p'Jum&p'Kung, p'A, p'Jib, Ton&Ple, Poom+, Buay, nong Ek, to name a few, who have been wandering around Edinburgh, keeping me company, cooking me good Thai food and seeking for the best barley juice in the world.

Special thanks to my parents and my brother for all being sources of encouragement, support and love.

Finally, I would like to gratify the Development and Promotion of Science and Technology Talents Project (DPST) for the financial support.

Contents

Abstract i

Declaration ii

Acknowledgement iii

1 Introduction **1**

1.1 Martensitic Transition 1

1.2 Zirconium 3

1.2.1 α-ω Transformation 4

1.2.2 β-α Transformation 5

1.3 Previous Limitations 10

2 Molecular Dynamics **13**

2.1 Potential 14

2.1.1 Finnis-Sinclair Potential 15

2.1.2 Potential for Zirconium 16

2.2 Initial and Boundary Conditions 17

2.3 Ensembles 18

2.3.1 Microcanonical Ensemble (NVE) 19

2.3.2 Canonical Ensemble (NVT) 19

2.3.3 Parrinello Rahman Scheme (NPH) 21

2.3.4 Constant Stress and Temperature (NσT) 23

2.4 Gear Predictor-Corrector 24
2.5 Conclusions 27

3 Pretransition Phenomena **28**
3.1 Phonon Frequency Measurements 29
3.1.1 Normal Mode Calculations 29
3.1.2 Neutron Scattering Experiment 32
3.2 The bcc Phase 35
3.2.1 Anharmonicity 35
3.2.2 Phonon Dispersion Curve 39
3.2.3 Instability of $[\xi\xi 2\xi]$ and $[\xi\xi 0]$ Branches 41
3.2.4 Temperature Dependence of T_{1N} Phonon 43
3.2.5 Phonon Density and bcc-hcp Transition 45
3.3 The hcp Phase 50
3.3.1 T_{1N} Phonon in Low Temperature Phase 50
3.3.2 Perturbative Normal Mode Calculation 55
3.3.3 Induced Reverse Transition 56
3.4 Conclusions 59

4 Elastic Theory of the Martensitic Phase **61**
4.1 A Single hcp Variant 62
4.1.1 Nishiyama-Wessermann Rules 63
4.1.2 Computational Setups 66
4.1.3 Stacking Faults 69
4.1.4 Density of Stacking Faults 72
4.2 Twinning 75
4.2.1 Perfect Twins 76
4.2.2 Twins and Stacking Faults 79
4.2.3 Effect of Stacking Faults on the Twinning Angle 82

4.2.4 Microstructure Formation 84
4.2.5 Energy Balance 87
4.3 Conclusions 87

5 Martensitic Microstructural Evolution **89**
5.1 Microstructure Illustrations 90
5.1.1 Neighbour Distribution Functions 92
5.1.2 Body-centered Cubic (bcc) Structure 93
5.1.3 Close-packed (cp) Structures 95
5.1.4 Quenching Atomic Configuration to Absolute Zero 98
5.1.5 Thermal Fluctuation Removing Procedures 100
5.2 Natural Evolution 102
5.2.1 Transition Temperature 103
5.2.2 Nucleation Theory and Growth Kinetics 106
5.2.3 Twin Boundary and Twin Boundary Steps 113
5.2.4 Microstructure Evolution 116
5.3 Conclusions 119

6 Twinning Deformation **122**
6.1 Deformation Simulations 123
6.2 Elastic Deformation 125
6.3 Twinning Deformation 127
6.3.1 Martensitic Microstructure 127
6.3.2 Perfect Twins 137
6.4 Conclusions 140

7 Conclusions **142**

A Smoothing Spectrum and Maximum Entropy **147**

B Rotational Operations **150**

C Published Papers **153**

References **154**

Chapter 1

Introduction

> ... The regimented manner in which atoms change position in this (martensitic) transformation has led to it being termed *military*, in contrast to diffusion-controlled transformations which are termed *civilian* ...
>
> D.A.Porter and K.E.Easterling,
> Phase Transformations in Metals and Alloys.

1.1 Martensitic Transition

A martensitic transition is a solid-to-solid phase transition [1]. It was first recognised as the hardening and softening in iron by temperature. The transition happens when materials microscopically change their structures. The parent lattice requires little distortion and hence little movement of atoms or molecules is involved. This can be described as an elastic deformation in the sense that the deformation is locally continuous. No diffusion of atoms or molecules or discontinuous movement of atomic planes occurs. The local transition strain is well-defined. Macroscopically the kinetics and morphology of the martensitic transition are dominated by the energy of this strain and a microstructure is formed

as a result [2]. The examples of this phase transition are found in many metals and alloys, for instance, transition metals in group-IV (bcc-hcp), Fe (fcc-bcc), Li (bcc-hcp, bcc-9R), Tl (bcc-hcp) and Co (fcc-hcp) [3]. Martensitic transition is the fundamental principle of shape memory materials and superelastic materials.

Shape Memory Effect (SME)

There are a number of alloys, for example CuAlNi, CuZnAl and NiTi, which can recover their shape from large deformations by temperature treatment [3]. This effect - the Shape Memory Effect (SME) - results from an appropriate martensitic transition which in this particular case is induced by temperature. The transition can generate several martensite variants, for example 24 variants in CuZnAl from a high symmetry parent phase. These variants form a microstructure which is twin-related and self-accommodating in order to minimise change in the macroscopic strain. When the martensite microstructures are deformed, those variants which reduce the stress will become dominant. As a consequence, these materials allow large deformations before any plastic damage begins to operate. In the reverse process, even though there is an interchange between variants by deformations, those variants still transform back exactly to the same parent structure with the same orientation. The macroscopic shape is recovered as a consequence. The forward and reverse processes might not happen at the same temperature and may cause a hysteresis loop in the temperature-strain curve. This is called the thermoelastic property [3]. Typically, the martensite phase occurs at lower temperature and shape deformations are recovered by heating the material.

Superelastic Materials

The martensitic transition can be induced also by hydrostatic pressure, hydrostatic compression, tensile stress and uniaxial load. With the same principle, several martensite variants can be generated from the parent phase by applying

a stress. This transformation can yield large deformations. When the stress disappears, those martensite variants transform back to the parent structure and the shape is again recovered. This effect is called superelasticity or pseudoelasticity. The transition also causes a hysteresis loop in the stress-strain curve. By analogy to magnetic systems, this is termed ferroelasticity [3].

1.2 Zirconium

Zirconium [4, 5] is a transition metal in group-IV, the same as titanium, and hafnium. It was discovered in 1789 by M.H.Klaproth and first isolated from its ores in 1824 by J.J.Berzelius. Zirconium is a hard, lustrous, silvery coloured metal. The atomic number is 40 and its weight is 91.22amu. The electronic structure is [Kr] $4d^2 5s^2$. It has a hexagonal close-packed structure at room temperature. Zirconium is extremely corrosion resistant due to the formation of a stable oxide film. It is unaffected by alkalis, caustics, salt solutions, molten salts or strong acids, except hydrofluoric. It is nontoxic and biocompatible. Zirconium also has many interesting physical properties. It has a very small neutron scattering cross section and hence it is highly transparent to thermal neutrons. It has relatively low density and a high thermal conductivity. The linear expansion coefficient at 273K - 373K is 5.9×10^{-6} K^{-1} which is comparatively low. The melting point is 2,125K. In polycrystalline form, the bulk modulus is 90GPa, the Young's modulus is 98GPa, the shear modulus is 36GPa and Poisson's ratio is 0.38. With all these physical properties, zirconium can be used in nuclear reactors, surgical appliances, vacuum tubes and lamp filaments. It is also used as an alloying agent to improve the mechanical properties of resultant alloys.

Zirconium has two modes of martensitic phase transition. The first one is a transformation from body centered cubic (β phase) to hexagonal close-packed (α phase), triggered by lowering temperature. Another mode is a transformation from α phase to another close-packed structure, called ω phase, induced by

extreme pressure. The phase diagram is shown in fig.1.1.

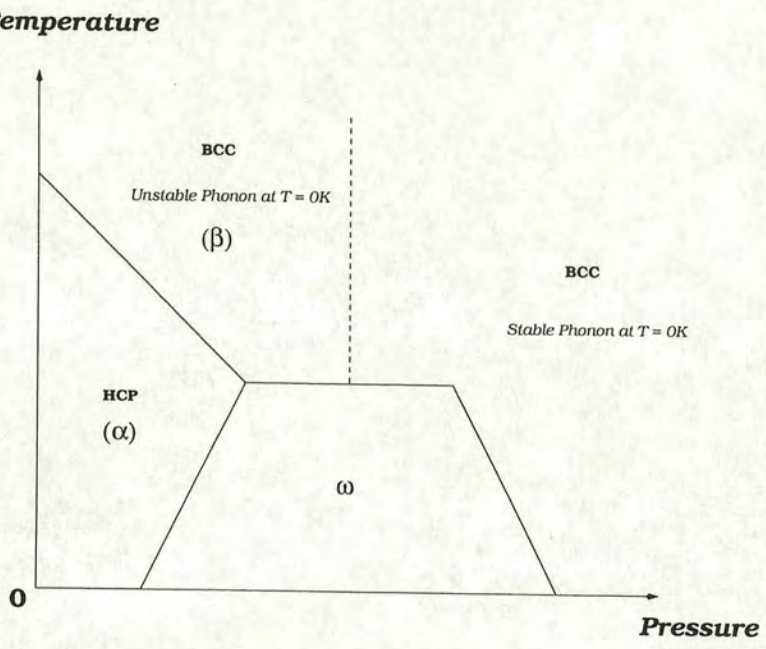

Figure 1.1: Phase diagram of group-IV transition metals, adapted from [6].

1.2.1 α-ω Transformation

The α-ω martensitic transition is beyond the scope of the present work. We mention it here briefly for completeness. In all group-IV transition metals, the phonon in $\frac{2}{3}[111]_{bcc}$ has an anomalous behaviour, i.e. the phonon frequency is approaching zero [7]. This is because of the inner electronic structure of these metals. When the pressure is higher, the d-band structure gets broadened. This stabilises a new phase, called ω phase [6]. In this phase, the structure is unequally densely packed in $(0001)_\omega$ planes, i.e. a sequence of open packed planes stacking alternatively with more densely packed planes. The local charge density of the more densely packed atom has a directional preferential character [6]. The c/a ratio in the ω phase is 0.60. The ω phase is technologically unfavourable because it embrittles in some alloys [8].

1.2.2 β-α Transformation

In the present study we consider only the β to α martensitic transition. We chose zirconium as a model case for all group-IV transition metals because, unlike titanium, zirconium has no magnetic moment which might also affect the phase transition. The phase transition is purely mechanical [6]. It is possible to study the phase transition by using classical means. The transition temperature T_0 is 1,138K [4].

Origin of the Transition

The nature of the kinetics of this type of transition has been widely investigated. In 1947 Zener [9] studied β-brass and proposed a soft mode model in which the frequency of a particular phonon decreases as the transition approaches and is equal to zero at the transition temperature. Below the transition temperature each unit cell in the lattice becomes mechanically unstable and a phase transition occurs. In this case one of the single crystal elastic constants, i.e. $\frac{1}{2}(C_{11} - C_{12})$ will tend to zero at the transition, but there is no local phonon instability.

However, the mechanism is not always so simple. Using inelastic neutron scattering, the phonon dispersion curves of zirconium have been measured [10, 11] and revised [7]. The T_{1N} phonon in the bcc phase is softened a little towards the transition temperature with a slope of 0.0008THz/K. Although this softening is consistent with the soft mode model in which T_{1N} is the cause of the transition, this phonon has a finite frequency of about 1.08THz at the transition temperature [7]. In general the phonon mode will have lower symmetry than the crystal and hence will couple to the macroscopic strain. The neutron-measured phonon does not incorporate coupling to an infinite wavelength strain, this coupling explains the occurrence of the transition prior to the T_{1N} mode frequency going to zero. The T_{1N} phonon in real space is shown in fig.1.2.

Several theoretical models have been proposed in order to describe the experi-

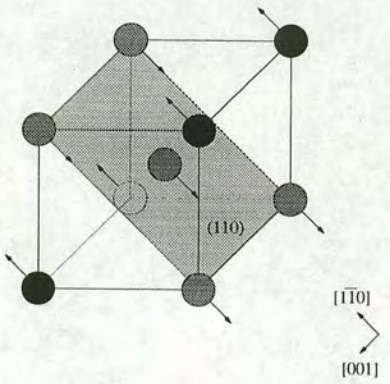

Figure 1.2: Shows the T_{1N} phonon in real space. The shaded plane is $(110)_{bcc}$ and the amplitude of vibration is in $[1\bar{1}0]_{bcc}$ direction.

mental results. May, *et al.* [12] studied the vibrational properties of zirconium by using a Born-Mayer type potential. They concluded that zirconium manifests line broadening, line shifts and interference which are the main features of a strongly anharmonic system. Ab initio work by Ye, *et al.* [13] employed the frozen phonon method and discovered that the modes along this particular phonon branch, i.e. $\mathbf{k} = [\xi\xi 0]_{bcc}$, are strongly coupled. Willaime and Massobrio [14] derived a 4-parameter embedded atom method (EAM) potential for zirconium. In harmonic and quasiharmonic regimes, the T_{1N} phonon becomes unstable, but using molecular dynamics they found that the phonon is dynamically stable and has a finite frequency at higher temperature. From the fact the that anharmonic effect is fully included via the interatomic potential, this result confirms that the anharmonic effect has an important role for stabilising the bcc lattice.

From the thermodynamic point of view, theoretical approaches such as Landau theory, mean field theory [15] and self-consistent phonon theory [16, 17] led to the same conclusion that the excess vibrational entropy stabilises the high temperature phase. This can be explained as follows. Firstly, the T_{1N} phonon has a peculiarly low frequency and thus can be excited easily [16, 17]. Consequently, the vibrational entropy of the system becomes large enough to stabilise the bcc

structure. Experimentally, Heiming, *et al.* [7] calculated the entropy difference between the bcc and hcp phases and found that the vibrational entropy has 65% contribution. Even though *ab initio* calculations have shown that the density of states at the Fermi energy in bcc is higher than in hcp [6, 18, 19] and there is a possibility that the phase transition is due to excess electronic entropy, it has been shown that the electronic entropy has a minor effect [7, 14].

Secondly, at the transition temperature, the frequency of the phonon is still finite but the magnitude of the fluctuations is decreasing and therefore its vibrational entropy is no longer sufficient to stabilise the bcc structure and the transition to hcp structure takes place. This is in good agreement with the experimental results. The phonon density of states in a low frequency region around 1.69THz is lowered with decreasing temperature [7].

The argument of excess entropy stabilising the high temperature phase is also applied to the similar martensitic transition in lithium [20] and NiAl alloys [21]. However, since the transition in zirconium occurs above the Debye temperature the phonon entropy argument should be treated with caution.

Path of the Transformation

This transformation can be regarded as an orthorhombic distortion of the bcc lattice. The 109.47° bond angle changes to 120° and $(110)_{bcc} \rightarrow (0001)_{hcp}$. This is associated with an acoustic transverse N-point phonon (the T_{1N} phonon) in the bcc lattice. This phonon mode cause $(110)_{bcc}$ to move up and down alternatively in $[1\bar{1}0]_{bcc}$ direction to obtain the ABABAB close-packed structure along $[110]_{bcc}$ direction. In the case of zirconium every second $(110)_{bcc}$ displaces by 0.94Å in $[1\bar{1}0]_{bcc}$ direction. The maximum displacement of individual atoms in this perfect transition path relative to their previous sites is 0.47Å. This distance is very small compared to the nearest neighbour distance. So the mechanism is considered as martensitic rather than diffusive.

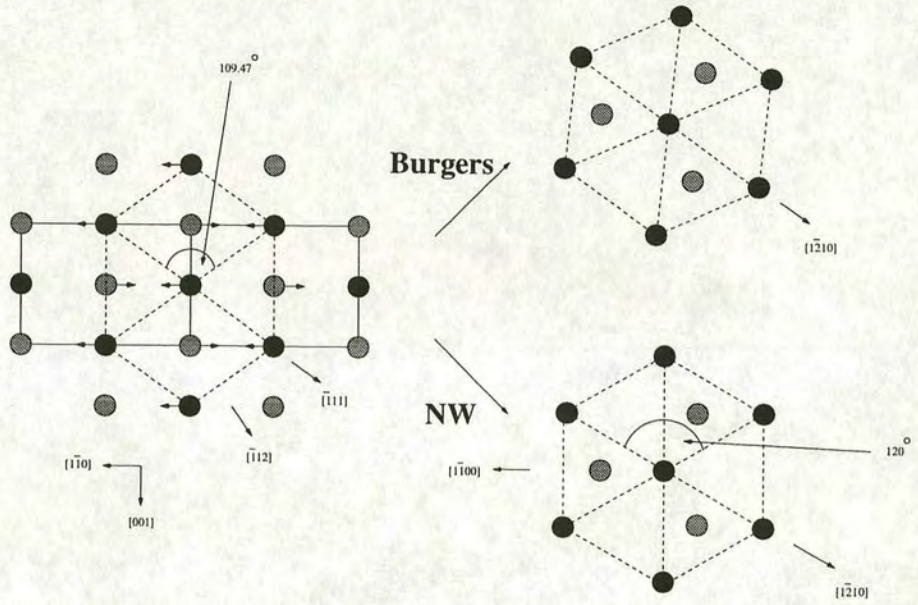

Figure 1.3: Illustrates Burgers [23] and Nishiyama-Wessermann (NW) [1] paths for bcc (left) to hcp (right) transformation.

It is worth mentioning that the way to obtain the orthorhombic distortion is not unique. A few different mechanisms have been proposed for this type of transition [22]. The first candidate involves the T_{1N} phonon mode and the orthorhombic distortion through shear strain in $[1\bar{1}\bar{2}]_{bcc}$. The orientation relations are

$$(110)_{bcc} \parallel (0001)_{hcp}, \tag{1.1}$$

and,

$$[\bar{1}11]_{bcc} \parallel [1\bar{2}10]_{hcp}. \tag{1.2}$$

Burgers [23] first studied this transformation path in zirconium alloys. The bcc-hcp transformation in lithium also obeys this mechanism. On the other hand, the Nishiyama-Wessermann rules which require a few components of long wavelength strain for the distortion and also the same phonon mode [1] give slightly different

orientation relations, which are

$$(110)_{bcc} \parallel (0001)_{hcp}, \tag{1.3}$$

and,

$$[1\bar{1}0]_{bcc} \parallel [1\bar{1}00]_{hcp}. \tag{1.4}$$

The transformation mechanisms of both paths are illustrated in figure 1.3. Note that different shaded circles label different layers of the $(110)_{bcc}$ planes.

In the presence of interfaces, these mechanisms will produce different habit planes. In zirconium, it has been confirmed by experiment that the path of the transformation proceeds via the Burgers mechanism [23, 26, 27, 28, 29]. In fact, the habit planes are dependent on the twin modes. In zirconium, the habit planes [3] are $(596)_{bcc}$, $(8, 12, 9)_{bcc}$, $(334)_{bcc}$ and $(441)_{bcc}$.

Microstructure

As we have already seen the phase transition occurs by a distortion involving both the phonon and the strain, which is in general accommodated by the formation of a microstructure. Electron microscopy shows that the final microstructure is dependent upon the cooling rate. At slow cooling rates, of the order of 1-100°C per second, pure zirconium has laths structure [26, 27, 28] and zirconium alloys have a Widmanstätten structure [28, 29]. In contrast, at fast cooling rate, i.e. 2000°C per second, it forms a martensitic microstructure [29]. Therefore, twinning via the phase transition rarely occurs in zirconium [26, 30]. However, studying the martensitic microstructure is important because it gives an understanding of the shape memory effect and superelasticity in a number of materials. It has been investigated mostly by theoretical models [31, 32, 33, 34]. In contrast, it is impracticable to examine experimentally because the typical martensite growth speed is close to the speed of sound in metals [1].

Deformation Modes

Zirconium is ductile [35]. Therefore the deformation in zirconium is also of interest. The primary deformation is a prismatic slip [26, 35, 36] in $\frac{1}{3} < 1\bar{2}10 > \{1\bar{1}00\}_{hcp}$ and a secondary slip [35] is $\frac{1}{3} < \bar{1}\bar{1}23 > \{10\bar{1}1\}_{hcp}$. Twinning has 10%-15% contribution [4, 37]. Typical twins in real zirconium occur via strain deformation. By using molecular simulations, Serra and Bacon [38] calculated possible twin structures in zirconium which are $\{10\bar{1}1\}_{hcp}$, $\{10\bar{1}2\}_{hcp}$, $\{11\bar{2}1\}_{hcp}$ and $\{11\bar{2}2\}_{hcp}$ twins. This agrees very well with electron transmission microscope (TEM) experiments. At room temperature, $\{10\bar{1}2\}_{hcp}$, $\{11\bar{2}1\}_{hcp}$ and $\{11\bar{2}2\}_{hcp}$ twins are common [26, 30] and in a combination of high stress and temperature, $\{10\bar{1}1\}_{hcp}$ twins are dominant [39]. Stacking faults are also observed in twinning deformation [30].

1.3 Previous Limitations

Our primary aim is to study the martensitic transition in a complex system, such as in zirconium. Thus, it needs sophisticated models and careful treatment unlike the Bain transformation which requires only one order parameter, i.e. c/a ratio [40]. Lindgård and Mouritsen [24, 31] used strain components as order parameters in Landau theory to study martensitic transition in zirconium. A similar method was applied by Gooding and Krumhansl [32] to study the bcc $\rightarrow$ 9R transition in Li. They used a corresponding phonon as an order parameter and combined the phonon with strain components. Both works show that the transition is first order and stacking faults can be formed in a metastable state. The development of martensitic microstructure during the transition has been investigated [24, 33]. Anharmonic effects were included, but the existence of hcp variants was limited to two possible orientations. In real zirconium, the symmetry of the phase transition allows for up to six equivalent hcp variants.

We employed an atomistic simulation which has many advantages over other methods because it includes anharmonicity, long range strain, exact number of variants, correct lattice orientations, anisotropic elasticity, twins boundaries, and lattice defects. Atoms are treated individually, and so the appropriate symmetries of the transition are automatically included. With suitable potentials, it is widely used for studying structures and phase transitions in a large number and various kinds of metals and alloys, for example, zirconium [14, 25], iron [41], titanium-vanadium alloys [34], nickel-aluminium alloys [21] and copper-based shape memory alloys [42]. The twinned microstructure in titanium has been simulated by using static relaxation the energetics and relaxed structure of twins and twinning dislocations in the hcp phase [38, 43]. It correctly reproduced the structure as obtained by electron microscopy [44]. Nevertheless, previous simulational work at the atomistic level has been rather limited. Anomalies in vacancy and self diffusion migration have been reported [45], and these have been shown to be associated with the non-ideal c/a ratio of zirconium. [46]. The evolution of the transition in a titanium-vanadium alloy has also been simulated at a low temperature [34], but no twinned microstructure was observed. Likewise, the martensitic transition in iron has also been investigated using molecular dynamics (MD). This differs from zirconium in that it is between face centered cubic (fcc) and bcc rather than hcp and fcc. Again no microstructure was observed.

Major requirements for studying such a phase transition and examining its microstructure are a suitable choice of potential that accurately represents the interesting material, zirconium in this case, and computation methods that allow large numbers of atoms and provide correct solutions in a reasonably long timescale. Solutions to these requirements will be reviewed in the next chapter. In the current research, several large scale simulations with 75,000 atoms and several tens of thousands of integral timesteps have been used. The pretransition phenomena, such as the T_{1N} phonon frequency and its temperature dependency and the phonon instability is studied in chapter 3. In chapter 4 we investigate the

path of the bcc to hcp transformation. The strain released from the transformation can be calculated. This leads to formation of martensitic microstructures. General properties of stacking faults and their effects on the microstructures will be discussed. In chapter 5 the kinetics of the phase transition at a finite temperature is studied. The nucleation and the growth mechanism are discussed. Further evolution of martensite microstructure is illustrated. In chapter 6, we study deformation mechanism in perfect twins compared with twinning obtained by the phase transition. The overall conclusions are set out in chapter 7.

Some parts of this thesis have been published as :

- "Evolution of Microstructure in the bcc-hcp Martensitic Phase Transition in Zirconium [47]",
  G.J.Ackland and U.Pinsook, *MRS Symposium* **S7.7**, (1997).

- "Simulation of Martensitic Microstructural Evolution in Zirconium [25]",
  U.Pinsook and G.J.Ackland, *Phys. Rev. B* **58**, 11252 (1998).

- "Calculation of Anomalous Phonons and the hcp-bcc Phase Transition in Zirconium [48]",
  U.Pinsook and G.J.Ackland, *Phys. Rev. B* **59**, 13642 (1999).

Chapter 2

Molecular Dynamics

> .., the computational physicist needs a working knowledge of numerical analysis and computer programming. Beyond mastering these basic tools, a physicist must know how to use them to achieve the ultimate goal: *to understand the physical universe...*
>
> P.L.DeVries,
> A First Course in Computational Physics.

Molecular dynamics (MD) is a powerful method to study the classical motion of many-body systems. The objects in this simulation are regarded as point particles interacting with each other via a certain potential. The trajectory of each particle can be obtained by solving Newton's equations. Hence, MD requires a suitable potential and a reasonable integration scheme. It allows one to compute the time average of interesting physical properties, for example phonon frequency, lattice expansion or stress. Conventionally, MD simulation conserves the total energy and linear momentum. However, several thermodynamic variables are constrained in experiments, i.e. phonon frequency is measured in a constant temperature environment, lattice expansion is measured in a constant temperature and a constant pressure. The need of proper ensembles to match

simulation and experimental results emerges. We discuss the potential in section 2.1, the initial and boundary conditions in section 2.2, all relevant ensembles in section 2.3, and the integration scheme in section 2.4.

2.1 Potential

The interatomic potential is the most important key to simulate the properties of materials. In transition metals, the density of states (DOS), $\mathcal{D}(E)$, is characterised by a partially filled d band. This band is comparatively narrower with more occupied electrons than the next sp band and hence it has higher density. Friedel [49] originated the idea that filling d bands is responsible for variation in properties across the transition metals series. By using the second moment, $\mu^{(2)}$, of $\mathcal{D}(E)$, a number of predictions can be made. The cohesive energy which is the energy gained when atoms are condensed from infinity can be estimated. The trends of equilibrium cohesive energy, equilibrium bond length, bandwidth and bulk modulus are in a good agreement with experimental results. Bonding in Friedel's model is unsaturated. This is the characteristic of the metallic bonding where the number of valence electrons required to fill the band is fewer than the number of nearest neighbours. It also adequately describes non-ideal c/a ratio and anisotropic nature of hcp metals which are direct effects of d-d bonding [50].

However, there is some weakness in this model [50, 51]. Firstly, the cohesive energy is about 2eV smaller than found from experiment due to neglecting sp band and spd hybridisation. It is not a good model for high pressure phase transition which is caused by transferring electrons from s band to d band. The ω to bcc phase in zirconium is an example of this phase transition. Secondly, it might not be a good model for 3d transition metal series because these metals have magnetic moments which affect the crystal structure [51] but the magnetic effect is completely absent from the model.

2.1.1 Finnis-Sinclair Potential

Finnis and Sinclair [52, 53] use the second moment approximation to suggest a functional form of potentials for transition metals. The physics of this potential is clear and understandable. The potential is composed of two parts as follows,

$$E_{coh} = E_{rep} + E_{bond}. \tag{2.1}$$

The repulsive part arises from Coulomb repulsion between two neighbouring charge densities. It is sometimes regarded as a pair potential. It is short range because the screening effect in metals is extremely efficient. The bonding part arises from d band interaction as discussed earlier. By ensuring the local charge neutrality in each atom, the bonding energy is related to the second moment as

$$E_i^{bond} \propto \sqrt{\mu_i^{(2)}}. \tag{2.2}$$

From quantum mechanics, $\mu_i^{(2)}$ is the sum of first neighbour hopping parameters, β_{ij}^2, between atom i and its neighbours. β_{ij}^2 is averaged over d states as

$$\beta_{ij}^2 = \frac{dd\sigma_{ij}^2 + 2dd\pi_{ij}^2 + dd\delta_{ij}^2}{5}. \tag{2.3}$$

Consequently, the form of the bonding energy can be suggested as a function of a hopping integral, $\rho(r)$ where $\rho(r)$ is a function of the interatomic separation r. It must be a smooth, well-behaved and positive definite integral, instead of discontinuous hopping parameter β^2. The bond energy is now

$$E_i^{bond} \propto \sqrt{\rho_i(r)}. \tag{2.4}$$

The desired crystal structure can be stabilised by extending the range of the potential to the third neighbouring shell [54]. With the idea of local densities

of states, one can study defects in crystals [50]. The interatomic force can be obtained by differentiating this potential with respect to the atomic coordinates.

2.1.2 Potential for Zirconium

We use the Finnis-Sinclair potential [52, 53] which has assumed a cubic spline form [55] for close-packed metals in order to obtain an acceptable vacancy formation energy and reasonable cutoff parameters. Both repulsive and cohesive parts are short ranged, which are written as,

$$E_i = \frac{1}{2}\sum_j V(r_{ij}) \; - \sqrt{\rho_i}, \tag{2.5}$$

where

$$V(r) = \sum_{k=1}^{6} A_k (R_k - r)^3 H(R_k - r), \tag{2.6}$$

and

$$\rho_i = \sum_j \phi(r_{ij}) = \sum_j \sum_{k=1}^{2} a_k (r_k - r_{ij})^3 H(r_k - r_{ij}), \tag{2.7}$$

where $H(x)$ is the Heaviside step function, r_{ij} is the separation between atoms i and j. In the Finnis-Sinclair potential, some elastic criteria have to be satisfied [56], i.e.

$$\frac{C_{33} + C_{13}}{C_{11} + C_{12}} = 1, \tag{2.8}$$

and

$$\frac{C_{12} + C_{44}}{C_{13} + C_{66}} = 1. \tag{2.9}$$

The metals that meet these criteria are, for example, Mg, Zr, Ti, Hf and Ru.

In this study, the potential is aimed to represent the hcp phase in zirconium only and thus it was fitted to the 5 independent elastic constants in order to describe the anisotropic properties, the non-ideal c/a ratio which is 1.595, the cohesive energy of the hcp crystal structure relative to other possible structures and the energetics of vacancies and stacking faults [25, 57]. It has been shown to

k	A_k $(eV/\mathring{A}^3)$	R_k $(\mathring{A})$	a_k $(eV^2/\mathring{A}^3)$	r_k $(\mathring{A})$
1	-0.61248219	5.5763004	0.50569395	5.5763004
2	0.87645549	5.4848856	-0.00890725	4.7992749
3	-0.21947820	5.2106413	-	-
4	-0.01371379	4.3422011	-	-
5	0.68830444	3.6565904	-	-
6	1.45995293	3.1995166	-	-

Table 2.1: Parameters for zirconium, derived by Ackland *et al.* [57].

give a good description of other point defect properties [57] and twin boundary energies [38]. This is important since defects may be generated during the phase transition, and the scale of the energy minimising microstructure is governed by the relative energies of twin boundaries and strain. Although fitted only to the hcp phase, the potential is known to reproduce a good description of both bcc and hcp phases. The potential also gives a good description of elastic constants, cohesive energy and lattice parameter in the bcc phase. In particular the transition temperature observed by classical molecular dynamics at large system size lies between 1,330K and 1,390K [25], depending slightly on choice of boundary conditions and thermostats. The fitted parameters for zirconium are shown in table 2.1.

2.2 Initial and Boundary Conditions

In MD simulation, all information, such as particle positions and velocities, at the starting time, i.e. $t = 0$, are required to calculate particle trajectories at the next time step, δt. There is an initial value problem. A trivial choice for solid state simulations is that particles are situated at lattice sites of a particular structure. We avoid a perfect lattice because this configuration represents a minimum in energy and will produce a large fluctuation when the system moves toward an equilibrium state. The velocity of particles could be generated from

the Maxwell-Boltzmann distribution. However, this is not necessary since the MD itself will bring the system into an equilibrium very quickly [58] and hence the Maxwell-Boltzmann velocity distribution will be reproduced. Nevertheless the initial particle velocities must obey conservation of linear momentum, i.e. $\sum_i m_i v_i = 0$.

The length scale of the system is a crucial limitation of MD. Typical MD can be operated in the size of several hundred Ångström. The problem becomes more serious when one tries to study a phase transition for many reasons. Firstly, in free surface, the final microstructure will be affected by sample geometry and sample boundary. To reduce this effect, we introduce periodic boundary conditions where particles reenter the simulation box when they leave the box boundary from the opposite side. However, in a small system, periodic pattern will be generated in the microstructure. Thus the length scale must be carefully taken to avoid the finite size effect and periodic boundary effect. In the present work, we found that no periodic pattern persists in a system with length scale of 100Å. Unfortunately, there is no rigorous and general criterion for this. One must perform a preliminary test for a suitable length scale.

2.3 Ensembles

In most experiments the major macroscopic variables, such as temperature, T and pressure, P are fixed. The total energy is no longer a constant quantity. As we discussed earlier, a number of algorithms for generating various ensembles are needed in order to compare the calculation results with experiments. In this section we will discuss details of each ensemble using different Lagrangians, $\mathcal{L}$. The constant quantity of each ensemble is illustrated. The equation of motion can be derived directly from least action principle [59] as

$$\frac{d}{dt}\left(\frac{\partial \mathcal{L}}{\partial \dot{\mathbf{r}}_i}\right) - \left(\frac{\partial \mathcal{L}}{\partial \mathbf{r}_i}\right) = 0, \tag{2.10}$$

where $\mathcal{L}$ is an appropriate Lagrangian, $\mathbf{r}_i$ and $\dot{\mathbf{r}}_i$ are atomic position vector and atomic velocity vector respectively.

2.3.1 Microcanonical Ensemble (NVE)

In conventional MD, the number of particles and the volume of the system are fixed. The Lagrangian can be written as

$$\mathcal{L}_{NVE} = \frac{1}{2}\sum_{i}^{N} m_i \dot{r}_i^2 - \sum_{i}^{N} \mathcal{V}(\mathbf{r}_i) \tag{2.11}$$

where m_i is the mass of particle i and $\mathcal{V}(\mathbf{r}_i)$ is a suitable potential, equation (2.5) for example. The total energy in this ensemble is conserved. The particle trajectories are always on the surface of constant energy in phase space [58]. The averaged value of a dynamical variable A is equivalent to microcanonical ensemble average $< A >_{NVE}$, providing that the time scale is long enough. This is known as the ergodic hypothesis.

Practically, physical quantities in this simulation are not comparable with experimental results. Nonetheless, it is very useful for examining the accuracy of an integration algorithm. A sensible integration algorithm must produce the time independence of the total energy.

2.3.2 Canonical Ensemble (NVT)

Nosé [60, 61] derived the extended Lagrangian for a canonical ensemble using an extra dynamical variable, α, as

$$\mathcal{L}_{NVT} = \frac{1}{2\alpha^2}\sum_{i}^{N} m_i \dot{r}_i^2 - \sum_{i}^{N} \mathcal{V}(\mathbf{r}_i) + \frac{1}{2\mathcal{Q}} p_\alpha^2 - (f+1) k_B T \ln \alpha, \tag{2.12}$$

where T is the required temperature, f is the degree of freedom of the system and $\mathcal{Q}$ is equivalent to a mass and affects the rate of heat transfer. This can be

regarded as a coupling between a heat bath and the system by α and its conjugate momentum, p_α via the equation,

$$\dot{p}_\alpha = \sum_i^N \frac{p_i^2}{m_i \alpha^2} - (f+1)k_B T, \tag{2.13}$$

where $p_i^2 = m_i^2 \dot{r}_i^2$. The total energy is allowed to fluctuate to keep constant temperature. The system stays in a true canonical phase space [61]. The instantaneous temperature of the system is defined as

$$T_{instan} = \frac{1}{3Nk_B} \sum_i^N m_i \dot{r}_i^2(t). \tag{2.14}$$

As a consequence, the thermal properties of the system can be simulated. However, the major disadvantage of this algorithm is that the position vector and the time evolution of Nosé's equations of motion are scaled by a factor of α. It is impractical to implement. This led Hoover [62] to modify the Lagrangian in equation (2.12) by using the variable ξ instead of the variable α, and the Lagrangian can be written as

$$\mathcal{L}_{NVT} = \mathcal{L}_{NVE} + \frac{1}{2}\mathcal{Q}\dot{\xi}^2 - (f+1)k_B T\xi, \tag{2.15}$$

where $\xi = p_\alpha/\mathcal{Q}$. The equations of motion from Hoover's Lagrangian are,

$$\ddot{\mathbf{r}}_i = \mathbf{F}_i/m_i - \dot{\mathbf{r}}_i\xi, \tag{2.16}$$

and

$$\dot{\xi} = \frac{1}{\mathcal{Q}} \sum_i^N m_i \dot{r}_i^2 - (f+1)k_B T \tag{2.17}$$

where

$$\mathbf{F}_i = -\frac{\partial \mathcal{V}(\mathbf{r}_1, ..., \mathbf{r}_N)}{\partial \mathbf{r}_i}. \tag{2.18}$$

From Hoover's equations of motion, every variable represents the true and unscaled quantities. The configuration is still sampling the canonical ensemble [62]. The equation (2.17) is often regarded as a thermostat. Moreover, it is straightforward to integrate these equations of motion by using a typical numerical method.

2.3.3 Parrinello Rahman Scheme (NPH)

Andersen [63] derived an extended Lagrangian for a constant pressure simulation. This algorithm allows the volume of the simulation box to change without change in shape. It is useful for phase transition simulation of liquids. The generalised version of this scheme was later derived by Parrinello and Rahman [64]. The Parrinello-Rahman (PR) scheme, sometimes regarded as constant stress method, allows the change in the shape of the box as well as the volume.

In the periodic boundary condition, it is convenient to redefine the position vector, $\mathbf{r}_i$, as a unit vector, $\mathbf{s}_i$, related by

$$\mathbf{r}_i = \underline{B}_o \cdot \mathbf{s}_i \tag{2.19}$$

where $\mathbf{s}_i$ are in the range of $\begin{pmatrix} -0.5, 0.5 \\ -0.5, 0.5 \\ -0.5, 0.5 \end{pmatrix}$, and $\underline{B}_o$ is the box matrix,

$$\underline{B}_o = (\mathbf{a}, \mathbf{b}, \mathbf{c}) = \begin{pmatrix} a_x & b_x & c_x \\ a_y & b_y & c_y \\ a_z & b_z & c_z \end{pmatrix}, \tag{2.20}$$

where $(\mathbf{a}, \mathbf{b}, \mathbf{c})$ are a set of vectors describing the edges of the simulation box. Let us assume that each component of $\underline{B}_o$ is also a dynamical variable which results from a phase transition or external pressure. We can construct an extended Lagrangian as

$$\mathcal{L}_{NPH} = \frac{1}{2}\sum_{i}^{N} m_i \dot{\mathbf{s}}_i^T \underline{B}_o^T \underline{B}_o \dot{\mathbf{s}}_i - \sum_{i}^{N} \mathcal{V}(\underline{B}_o \mathbf{s}_i) + \frac{1}{2} W \mathrm{Tr}(\dot{\underline{B}}_o^{\,T} \dot{\underline{B}}_o) - P_{ext}\Omega \qquad (2.21)$$

where $\Omega = \det \underline{B}_o$ = volume of the system, P_{ext} = external pressure and W is equivalent to a mass, so-called box mass. This mass affects the rate of shape and volume changes.

The first two terms in equation (2.21) are of $\mathcal{L}_{NVE}$, the third term is the kinetic part of the components of $\underline{B}_o$, i.e. $\frac{1}{2}W\dot{B}_{\alpha\beta}^2$ and the last term is analogous to the potential part of the box matrix. This allows the volume of the system to fluctuate. The total energy is not conserved. The constant quantity in this scheme is enthalpy. In a solid state simulation, the system is allowed to undergo a phase transition and avoid having a highly stressed configuration. The derivation of the equations of motion for the PR scheme is straightforward,

$$\ddot{\mathbf{r}}_i = \mathbf{F}_i/m_i - (\underline{B}_o^T)^{-1} \dot{\underline{B}}_o^T \dot{\mathbf{r}}_i, \qquad (2.22)$$

and

$$W\ddot{\underline{B}}_o = (\underline{\Pi} - \underline{\mathbf{1}} P_{ext})\Omega(\underline{B}_o^{-1})^T, \qquad (2.23)$$

where

$$\Pi_{\alpha\beta} = \frac{1}{\Omega}\sum_i [m_i(\underline{B}_o \dot{\mathbf{s}}_i)_\alpha^T (\underline{B}_o \dot{\mathbf{s}}_i)_\beta + \sum_{j>i} (\mathbf{r}_{ij})_\alpha \mathbf{F}(\mathbf{r}_{ij})_\beta], \qquad (2.24)$$

$\mathbf{r}_{ij} = (\mathbf{r}_j - \mathbf{r}_i)$ and $\underline{\Pi}$ is the internal stress tensor which relates the kinetics of the system with its virial. The equation (2.23) can be referred as a barostat. The instantaneous pressure can be evaluated by

$$P_{instan} = \frac{1}{3} Tr\underline{\Pi}. \qquad (2.25)$$

It is worth noting that if $W \to \infty$, equation (2.23) vanishes and the particle trajectory in this Lagrangian is exactly the same as that of equation (2.11) and

the conventional molecular dynamics is recovered.

2.3.4 Constant Stress and Temperature (NσT)

This is the combination of NVT and NPH algorithms. This method is a powerful method for studying phase transitions. It allows the system to have a minimum strain energy and also to regulate latent heat caused by the phase transition itself. The Lagrangian is

$$\mathcal{L}_{NVT} = \mathcal{L}_{NVE} + \frac{1}{2}\mathcal{Q}\dot{\xi}^2 - (f+1)k_B T\xi + \frac{1}{2}W\mathrm{Tr}(\underline{\dot{B}_o}^T\underline{\dot{B}_o}) - P_{ext}\Omega, \qquad (2.26)$$

and the equation of motion can derived as

$$\ddot{\mathbf{r}}_i = \mathbf{F}_i/m_i - (\underline{B_o^T})^{-1}\dot{\underline{B_o^T}}\dot{\mathbf{r}}_i - \dot{\mathbf{r}}_i\xi. \qquad (2.27)$$

The thermostat and barostat are controlled by equations (2.17) and (2.23).

In a special case, if $\underline{B}_o$ is diagonalised, overall instantaneous strain can be calculated from the box matrix via

$$\underline{B}(t) = \underline{B}_o(\underline{I} + \underline{\varepsilon}(t)), \qquad (2.28)$$

where $\underline{\varepsilon}(t)$ is a matrix representation of strain at the time t. This evolution of strain can result from thermal expansion, external pressure or a phase transition.

Important factors in NVT and NPH ensembles are the fluctuation of temperature and volume. In fact, the fluctuation frequency is dependent on $\mathcal{Q}$ and W, temperature and the degree of freedom of the system [62, 65, 66] as follows:

$$\omega_{\mathcal{Q}} = \sqrt{\frac{fk_BT}{\mathcal{Q}}}, \qquad (2.29)$$

and,

$$\omega_W = \sqrt{\frac{fk_BT}{W}}, \tag{2.30}$$

where ω_Q and ω_W are the fluctuation frequency of temperature and the fluctuation frequency of volume respectively. If the fluctuation frequency is too high, the dynamics of the system will be dominated by the thermostat and barostat. In addition the system might be unstable in a long simulation. If the frequency is too low, the system would be unable to sample a correct ensemble. There is no certain criteria for these frequencies. One must perform some preliminary tests. It has been suggested that ω_Q [67] and ω_W [54] should be of order of 1.0THz. These frequencies should be fixed if one wishes to compare results from different setups.

2.4 Gear Predictor-Corrector

A good integration algorithm which is accurate within the MD timescale and conserves energy and momentum of the system is the heart of the MD method. We choose fourth-order Gear predictor-corrector because it has a simple form and it is reasonably fast. As discussed by Press, *et al.* [68], this algorithm is suitable for a problem which involves high-precision solution of very smooth and complicated functions. At each timestep, δt, the atomic trajectories are evolved as follows. Firstly, the positions, velocities and accelerations are estimated by using Taylor expansion about the current time t. This can be written in a vector form as

$$\begin{pmatrix} \mathbf{r}^p(t+\delta t) \\ \dot{\mathbf{r}}^p(t+\delta t) \\ \ddot{\mathbf{r}}^p(t+\delta t) \\ \dddot{\mathbf{r}}^p(t+\delta t) \end{pmatrix} = \begin{pmatrix} 1 & \delta t & \frac{1}{2}\delta t^2 & \frac{1}{6}\delta t^3 \\ 0 & 1 & \delta t & \frac{1}{2}\delta t^2 \\ 0 & 0 & 1 & \delta t \\ 0 & 0 & 0 & 1 \end{pmatrix} \begin{pmatrix} \mathbf{r}(t) \\ \dot{\mathbf{r}}(t) \\ \ddot{\mathbf{r}}(t) \\ \dddot{\mathbf{r}}(t) \end{pmatrix}. \tag{2.31}$$

The superscript p denotes the predicted values. These values do not produce correct trajectories since the interatomic forces have not yet been introduced. This leads to the next step in which we calculate the true force at the time $t + \delta t$ by using the predicted positions (and velocities if required). In our MD, the force evaluation in equation (2.18) together with (2.5) is the most time consuming process. The difference between the predicted and the corrected accelerations can be written as

$$\Delta\ddot{\mathbf{r}}(t+\delta t) = \ddot{\mathbf{r}}^c(t+\delta t) - \ddot{\mathbf{r}}^p(t+\delta t). \tag{2.32}$$

The superscript c denotes the corrected values. This equation can be regarded as an error in the prediction step. To obtain true trajectories, one must correct the predicted values by this error term as

$$\begin{pmatrix} \mathbf{r}^c(t+\delta t) \\ \dot{\mathbf{r}}^c(t+\delta t) \\ \ddot{\mathbf{r}}^c(t+\delta t) \\ \dddot{\mathbf{r}}^c(t+\delta t) \end{pmatrix} = \begin{pmatrix} \mathbf{r}^p(t+\delta t) \\ \dot{\mathbf{r}}^p(t+\delta t) \\ \ddot{\mathbf{r}}^p(t+\delta t) \\ \dddot{\mathbf{r}}^p(t+\delta t) \end{pmatrix} + \begin{pmatrix} C_0 \\ C_1 \\ C_2 \\ C_3 \end{pmatrix} \Delta\ddot{\mathbf{r}}(t+\delta t). \tag{2.33}$$

In this equation, $\mathbf{C}$ is a constant vector. The choice of $\mathbf{C}$ depends on the orders of the method and results in stability properties [68]. Gear [69] derived $(C_0, C_1, C_2, C_3) = (\frac{1}{6}, \frac{5}{6}, 1, \frac{1}{3})$ in the fourth-order scheme by considering the optimum stability and the accuracy of the solutions.

Notice that in equation (2.13) and (2.17) the equation of motion is controlled by the velocity term rather than the acceleration term. The predictor-corrector scheme is slightly different. Firstly, the corrected values must be calculated from atomic velocities as

$$\Delta\dot{\mathbf{r}}(t+\delta t) = \dot{\mathbf{r}}^c(t+\delta t) - \dot{\mathbf{r}}^p(t+\delta t). \tag{2.34}$$

Then the correction step can proceed as

$$\begin{pmatrix} \mathbf{r}^c(t+\delta t) \\ \dot{\mathbf{r}}^c(t+\delta t) \\ \ddot{\mathbf{r}}^c(t+\delta t) \\ \dddot{\mathbf{r}}^c(t+\delta t) \end{pmatrix} = \begin{pmatrix} \mathbf{r}^p(t+\delta t) \\ \dot{\mathbf{r}}^p(t+\delta t) \\ \ddot{\mathbf{r}}^p(t+\delta t) \\ \dddot{\mathbf{r}}^p(t+\delta t) \end{pmatrix} + \begin{pmatrix} C_0 \\ C_1 \\ C_2 \\ C_3 \end{pmatrix} \Delta\dot{\mathbf{r}}(t+\delta t), \tag{2.35}$$

where, $(C_0, C_1, C_2, C_3) = (\frac{3}{8}, 1, \frac{3}{4}, \frac{1}{6})$ [58].

Choice of Timestep

The optimum choice of δt is also important because for too large δt the system would be unstable, i.e. E is not conserved but for too small δt it would take unnecessary long time to produce an accurate ensemble. In the simulations of solid state, δt should be much shorter than the period of the typical phonon, for example Debye frequency of zirconium has a period of 26fs. Ackland [54] discussed the stability of predictor-corrector scheme with various δt. He found that δt should be smaller than 5fs. In this work, we choose $\delta t = 1$fs.

Neighbour List and Link Cell Method

As we mention above, the force evaluation is the most time consuming step. Fortunately, our potential is short ranged and drops to zero at a certain cutoff distance, r_c, for example the cutoff is 5.7Å in zirconium. Hence a simplification can be done. It is called 'Neighbour list and Link cell method [58, 70]' which can be compiled as follows. At a certain period, the list of neighbour atoms is constructed within a sphere of radius r_l a little larger than r_c. This list is used for evaluating the force. In each period, it must be ensured that no atom moves further than r_l. Otherwise, the updating period must be kept shorter. The neighbour list reduces the number of force evaluations from $\mathcal{O}(N^2)$ to $\mathcal{O}(N)$. When the list is updated, it is not necessary to examine every pair of atoms in the sys-

tem. Thus further simplification can be applied by dividing the whole simulation into small boxes with length $\geq r_l$ and indexing each box by an appropriate number and linking nearest boxes together. By this link cell method, the neighbour atoms can be considered within nearest boxes only. This reduces the number of pair examinations required from N^2 to $27NN_c$ where N_c is the number of atoms in each box.

2.5 Conclusions

In this chapter we have reviewed computational methods, i.e. molecular dynamics which will be used throughout the whole research. The MD provides numerical solutions of a many-body system by solving Newton's equation of motion. Various ensembles, such as constant energy, constant temperature and constant stress, have been discussed. These ensembles are important when we need to compare our results with experiments. With principle of d band interaction, Finnis-Sinclair suggested a functional form of a potential for a transition metal. We use this potential parameterised to represent zirconium. The properties of phonons in β zirconium at finite temperature and pressure are examined in chapter 3. The static structure in a constant stress configuration at 0K is calculated and analysed in chapter 4. The evolution of the phase transition and the microstructure at finite temperature and constant pressure is investigated in chapter 5. The deformation mechanism of martensitic microstructure by applied stress or strain is studied in chapter 6.

Chapter 3

Pretransition Phenomena

I know how you feel inside, I've .. I've been there before.
Something's changing inside you, and don't you know??..

from *Don't Cry* by Guns n' Roses.

In this chapter, we discuss the mechanism of the phase transition - both for the bcc-hcp transition and the hcp-bcc transition. We will discuss in more detail how the transitions happen, what are the causes and what pretransition phenomena are the precursor effects prior to those transitions.

As we discussed in chapter 1, the origin of the bcc-hcp transition in zirconium involves the instability of the T_{1N} phonon in the bcc phase. We will show later that this phonon is also involved in the hcp-bcc transition. Thus some methods for examining phonon properties are required. In section 3.1, we explain how to extract phonon frequencies from the MD simulations using the normal mode calculation and why this calculation can be compared directly with some experimental data. In section 3.2, we study the phonon properties in the bcc phase, such as anharmonicity, the phonon dispersion curve, the temperature dependence of the T_{1N} phonon, the phonon density and the link to the bcc-hcp transition. In section 3.3, the T_{1N}-equivalent modes are examined further in the hcp phase.

The phonon density is calculated. The way to obtain the hcp-bcc transition is suggested. The conclusions are laid out in section 3.4.

3.1 Phonon Frequency Measurements

In this section, we will show how the vibrational frequencies of a lattice can be calculated by using classical simulations and the normal mode method. A quantum excitation in the lattice vibration, i.e. phonon, is measured by neutron scattering experiment. We will show that the classical vibration and the phonon are analogous objects.

3.1.1 Normal Mode Calculations

Firstly, we start by considering a harmonic system in standard lattice dynamics because it is simple and manageable and it can be modified further later. The atomic arrangement is treated as a perfect lattice. The interatomic forces are approximately linearly proportional to the atomic displacements from their equilibrium positions. This is the case at low temperature where the displacements are small compared to the atomic separations. The vibrational displacements $\mathbf{u}_l(t)$ of atoms can be derived in terms of independent coordinates [71] as

$$\mathbf{u}_l(t) = \frac{1}{\sqrt{Nm}} \sum_{\mathbf{q}} \sum_{s} \alpha_{\mathbf{q}s}(t) \mathbf{e}_{\mathbf{q}s}, \tag{3.1}$$

where N is the total number of atoms in the system, m is the mass of an individual atom, the independent coordinates $\alpha_{\mathbf{q}s}$ are the normal mode coordinates, $\mathbf{q}$ labels all possible wavevectors allowed in the lattice, $\mathbf{e}_{\mathbf{q}s}$ are corresponding eigenvectors of each $\mathbf{q}$ and s labels the possible eigenvectors of $\mathbf{q}$, and $\mathbf{u}_l$ is the atomic displacement from equilibrium lattice site $\mathbf{l}$. The position vector $\mathbf{r}_l$ is then written in terms of $\mathbf{u}_l$ as

$$\mathbf{r}_l = \mathbf{u}_l + \mathbf{l}. \tag{3.2}$$

In the molecular dynamics method all measurable quantities, such as position and momentum, are real. Therefore we can consider only the real part of the phase factor $e^{i(\mathbf{q}\cdot\mathbf{l}-\omega t)}$. Therefore, the solution $\alpha_{\mathbf{q}s}$ of equation (3.1) can be written in the form [72],

$$\alpha_{\mathbf{q}s}(t) = A_s \cos(\mathbf{q}\cdot\mathbf{l} - \omega_s t + \theta_s), \tag{3.3}$$

where ω_s is the frequency corresponding to a particular mode $\mathbf{q}$ with the eigenstate s, A_s and θ_s are an arbitrary amplitude and an arbitrary phase factor respectively. We are free to choose the real part of $e^{i(\mathbf{q}\cdot\mathbf{l}-\omega t)}$ to be $\cos(\mathbf{q}\cdot\mathbf{l}-\omega t)$ which is an even function. One obvious advantage is that the Fourier transform will have this symmetry; if the function of time $\alpha_{\mathbf{q}s}(t)$ is real and even, then its Fourier transform $F(\omega)$ is also real and even [68].

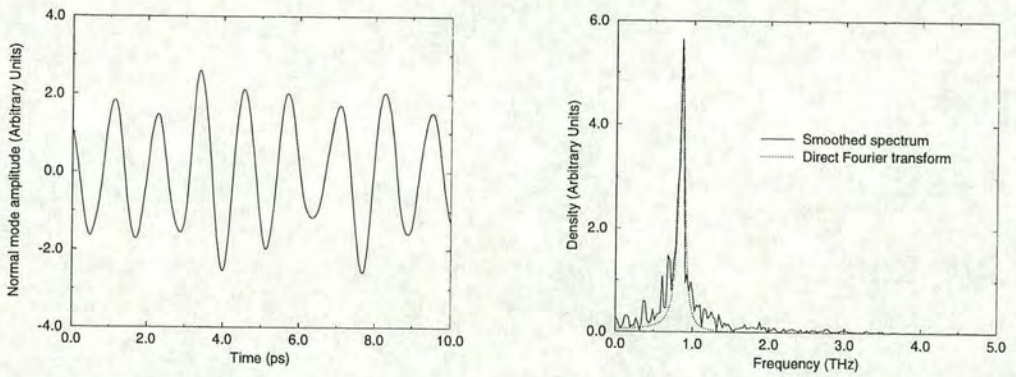

Figure 3.1: a) A typical evolution of a normal mode coordinate of which $\mathbf{q} = \frac{1}{16}[112]_{bcc}$, $\mathbf{e}_{\mathbf{q}s} = [11\bar{1}]_{bcc}$ taken from the MD simulation with 8,192 atoms at 600K. b) The Fourier transform of the normal mode. The sharp peak at $\omega = \omega_s$ reflects the strongly harmonic nature.

An alternative definition of $\alpha_{\mathbf{q}s}$ is the discrete spatial Fourier transform of $\mathbf{u}_l$ [72], which is

$$\alpha_{\mathbf{q}s}(t) = \sum_l \cos(\mathbf{q}\cdot\mathbf{l})\{\mathbf{u}_l(t)\cdot\mathbf{e}_{\mathbf{q}s}\}. \tag{3.4}$$

According to this equation, the lattice vibration of a particular wavevector $\mathbf{q}$ and a corresponding eigenvector $\mathbf{e}_{\mathbf{q}s}$ can be extracted from the atomic displacements, evolving in time via the MD with a suitable ensemble. A typical evolution of a normal mode coordinate is shown in figure 3.1 (a). The frequency of $\mathbf{q}$ can be calculated by using the square of the temporal Fourier transform of equation (3.4), the so-called power spectrum $P(\omega)$ where

$$P(\omega) = |\int_0^{t_{max}} dt\, e^{-i\omega t} \sum_l \cos(\mathbf{q}\cdot\mathbf{l})\{\mathbf{u}_l(t)\cdot\mathbf{e}_{\mathbf{q}s}\}|^2 = |\int_0^{t_{max}} dt\, e^{-i\omega t}\, \alpha_{\mathbf{q}s}(t)|^2. \quad (3.5)$$

The power spectrum can be written in terms of the atomic position autocorrelation by applying the Wiener-Khinchin theorem [68, 73] to equation (3.5), and we find that

$$\lim_{t_{max}\to\infty} \frac{1}{t_{max}} P(\omega) = \int dt\, e^{-i\omega t} \sum_l \cos(\mathbf{q}\cdot\mathbf{l}) < \{\mathbf{u}_l(t)\cdot\mathbf{e}_{\mathbf{q}s}\}\{\mathbf{u}_0(0)\cdot\mathbf{e}_{\mathbf{q}s}\} >, \quad (3.6)$$

where the symbol $< .. >$ denotes an ensemble average, the quantity $u(0)u(t)$ is called the autocorrelation of $u(t)$. This equation was also applied to the MD study of the phonon properties and the martensitic transition in FeNi alloys by Meyer and Entel [74].

Inserting equation (3.3) into either (3.5) or (3.6), we get

$$P(\omega) \propto \delta(\omega - \omega_s). \quad (3.7)$$

Thus the frequency of lattice vibration can be evaluated by either the power spectrum of a normal mode coordinate as in the equation (3.5) or the Fourier transform of the atomic position autocorrelation as in (3.6). There will be a sharp peak of the delta function at $\omega = \omega_s$ in the frequency spectrum as in equation (3.7) and shown in figure 3.1 (b). To calculate an accurate ensemble average of the position autocorrelation, one must allow sufficiently long time in the simulations.

This is reflected by the limit $t_{max} \rightarrow \infty$ in equation (3.6). The equations (3.5) and (3.6) will play the main role for examining vibrational properties in both bcc and hcp structures.

Normal mode coordinate is calculated by equation (3.4) and its Fourier transform has a sharp peak at $\omega = \omega_s$.

3.1.2 Neutron Scattering Experiment

Coherent inelastic neutron scattering experiment is the incomparable method for studying phonon dispersion curves and phonon properties. The method has been excellently reviewed by Squires [75] and Lovesey [76]. We discuss here briefly the fundamental principle and some relevant mathematical tools. This section will illustrate the equivalence between phonon frequencies obtained by the neutron scattering experiment and lattice vibrational frequencies obtained by the normal mode method.

The neutron is a neutral particle with spin $\frac{1}{2}$. Because of their neutrality, free neutrons can penetrate into atoms, close to the nuclei and interact with the nuclei via the strong nuclear force. The strong interaction affects the energy and the momentum of those free neutrons. This is called the scattering process. The de Broglie wavelength of thermal neutrons is of the same order as the atomic separation in typical lattices. The coherent scattering process provides the information about the correlation between the position of the different nuclei at different times. In a lattice, this position correlation is closely related to the lattice vibration, i.e. the phonon. Furthermore, the energy of the thermal neutrons is of the same order as the typical phonon. In the other words, the scattering by the phonon will yield noticeable change in the neutron energy. For these reasons, the coherent inelastic neutron scattering is extensively used for measuring

the phonon properties in solids. The process is inelastic because the scattered neutrons will change their momentum as well as their energy as we shall describe later.

The measurable quantity of the coherent neutron scattering process is the partial differential cross section, $\left(\frac{d^2\sigma}{d\Omega dE'}\right)_{coh}$ which assesses the number of scattered neutrons per second into a small solid angle $d\Omega$ in a particular direction with final energy between E' and $E' + dE'$, divided by incident neutron flux in the solid angle $d\Omega$ and the energy range dE'. In a Bravais lattice it can be deduced [75, 76] as

$$\left(\frac{d^2\sigma}{d\Omega dE}\right)_{coh} \propto Ne^{-K^2<u^2>} \int_{-\infty}^{\infty} dt\, e^{-i\omega t} \sum_l e^{i\mathbf{K}\cdot\mathbf{l}} < \{\mathbf{K}\cdot\mathbf{u}_0(0)\}\{\mathbf{K}\cdot\mathbf{u}_l(t)\} > \quad (3.8)$$

where $\mathbf{K}$ is the scattering wavevector of the neutrons, $\mathbf{K} = \mathbf{k} - \mathbf{k}'$, $\mathbf{k}$ is the incident wavevector, $\mathbf{k}'$ is the outgoing wavevector, $e^{-K^2<u^2>}$ is called the Debye-Waller factor, $\hbar\omega$ is the difference between initial energy E and final energy E', i.e. $\hbar\omega = E - E'$. This cross section is known as one phonon scattering process as only one quantum of phonon is involved in a single scattering.

The scattering process in equation (3.8) is a quantum process. It is obvious that $\mathbf{u}_l$ is a quantum operator. The main complication of equation (3.8) is to evaluate $\mathbf{u}_l(t)$ and its autocorrelation. In a perfect harmonic lattice $\mathbf{u}_l(t)$ can be derived in terms of a complete set of harmonic operators $\hat{a}_s$ and $\hat{a}_s^\dagger$ as [75, 76]

$$\mathbf{u}_l(t) = \sqrt{\frac{\hbar}{2mN}} \sum_{\mathbf{q}} \sum_s \frac{\mathbf{e}_{\mathbf{q}s}}{\sqrt{\omega_s}} \{\hat{a}_s e^{i(\mathbf{q}\cdot\mathbf{l}-\omega_s t)} + \hat{a}_s^\dagger e^{-i(\mathbf{q}\cdot\mathbf{l}-\omega_s t)}\}. \quad (3.9)$$

Inserting equation (3.9) into (3.8), we get two selection rules for measuring the number of scattered neutrons [75, 76]. The first rule states that the number of scattered neutrons is accessible via equation (3.8) if and only if the final energy

E' and the final wavevector $\mathbf{k}'$ satisfy,

$$E' = E - \hbar\omega_s, \tag{3.10}$$

and

$$\mathbf{k} - \mathbf{k}' = \mathbf{T} + \mathbf{q}, \tag{3.11}$$

where $\mathbf{T}$ is any reciprocal lattice vector. In this process, a scattered neutron loses energy by creating a phonon quantum, $\hbar\omega_s$. It is then called the phonon creation process.

The second rule states that the number of scattered neutrons is accessible if and only if E' and $\mathbf{k}'$ satisfy,

$$E' = E + \hbar\omega_s, \tag{3.12}$$

and

$$\mathbf{k} - \mathbf{k}' = \mathbf{T} - \mathbf{q}. \tag{3.13}$$

In this process, a scattered neutron gains energy by annihilating a phonon quantum, $\hbar\omega_s$. It is called the phonon annihilation process.

In neutron scattering experiments, $\mathbf{T}$ must be chosen so that $\mathbf{q}$ lies in the first Brillouin zone. Consequently, the frequencies of $\mathbf{q}$, if it currently exists in the lattice, can be evaluated by measuring energy gained or lost and the change in momentum of scattered neutrons in a suitable direction. This measurement allows one to construct the whole phonon dispersion curve and to study other phonon properties, such as the temperature dependence. These scattering processes are inelastic because $|\mathbf{k}'| \neq |\mathbf{k}|$.

It is worth mentioning that equation (3.6) and (3.8) share a similar form of the spatial and temporal Fourier transform of the position autocorrelation. By inserting the appropriate harmonic approximation representations of the atomic

displacements into these relations, the same frequency of the same vibration mode can be derived. These relations imply the equivalence between the normal mode calculations and the neutron scattering experiment and the analogy between the lattice vibration and the phonons. One discrepancy is that in the former case the lattice vibrations of ω_s in equation (3.3) are classical objects but in the latter case a quantum phonon is the measurement of a quantised vibrational energy $\hbar\omega_s$ in equation (3.10) and (3.12).

Neutrons probe the autocorrelation function - not the curvature of the energy surface - which is equivalent to the normal mode calculations.

3.2 The bcc Phase

Zirconium has the bcc structure at temperatures higher than 1,333K according to our potential; see how to define the transition temperature in section 5.2.1. At this temperature the atomic displacements are large and hence the anharmonic effects are enhanced. In this section, we will study the role of the anharmonicity to stabilise the bcc phase. Two pretransition phenomena, namely the temperature dependence of the T_{1N} phonon and the phonon density, will be examined. The link between these phenomena and the phase transition will be illustrated.

3.2.1 Anharmonicity

As discussed theoretically by May, *et al.* [12], Ye, *et al.* [13] and Willaime and Massobrio [14] and confirmed experimentally by Heiming, *et al.* [7], β zirconium exhibits strong anharmonicity. This means that the normal mode coordinates in equation (3.3) are no longer independent. Energy in each mode will gradually transfer to other modes. The anharmonic effects cause thermal resistivity and

the difference between constant pressure and constant volume specific heat of the lattice [71]. The most relevant effects in our study are the lattice expansion and the broadening of the peak in equation (3.7).

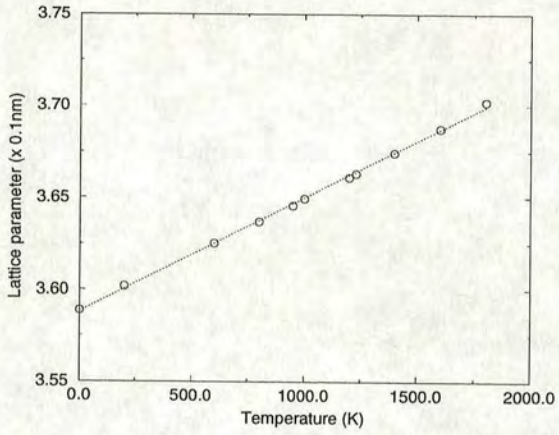

Figure 3.2: Shows the lattice expansion in the bcc phase from 0K-1,800K. The dotted line is a linear model with the linear coefficient of 6.194×10^{-5}Å/K. The simulations were done in the constant pressure and constant temperature MD mode with 8,192 atoms.

To study the lattice expansion in β zirconium, we initialise the atomic configuration by using a homogeneous bcc lattice. A preliminary series of constant pressure simulations is carried out. The variation of bcc lattice parameter with temperature is shown in figure 3.2. Note that throughout this chapter, the unit cell is oriented along $(100)_{bcc}, (010)_{bcc}$ and $(001)_{bcc}$. According to the potential, we found that lattice expansion is linear. The relation between the lattice parameter and temperature (dotted line in figure 3.2) is empirically derived between 0K-1,800K as

$$a(T) \simeq 3.588 + 6.194 \times 10^{-5} T. \tag{3.14}$$

A similar method was also applied to study the lattice expansion in iron by Osetsky and Serra [41]. The lattice expansion coefficient in our calculation is

6.194×10^{-5}Å/K compared with the experimental result of 1.9×10^{-5}Å/K. The difference arises because the Finnis-Sinclair potential assumed the fixed electronic band structure whereas the real electronic structure can be altered by the effect of temperature and pressure.

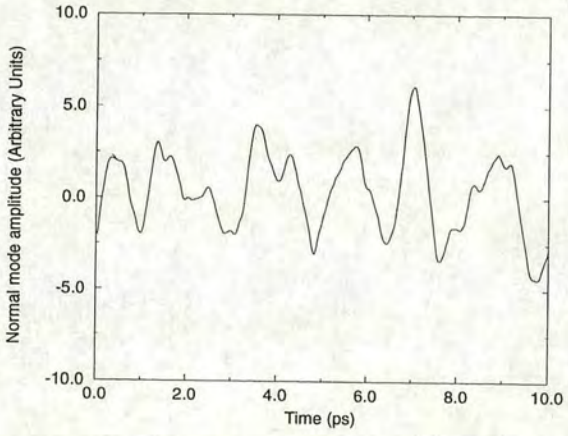

Figure 3.3: A typical evolution of a normal mode coordinate of which $\mathbf{q} = \frac{1}{2}[110]_{bcc}$, $\mathbf{e}_{\mathbf{q}s} = [1\bar{1}0]_{bcc}$ taken from the MD simulation with 8,192 atoms at 1600K.

The anharmonic effects also cause the evolution of the normal modes to depend on the excitation of other modes, especially at high temperature. A peak at ω_s in equation (3.7) will be broadened by these coupling effects. In quantum language, these coupling effects lead to the term 'scattering' where phonons are interacting with each other. The phonon-phonon scattering causes phonons to have a limited lifetime and hence a finite thermal conductivity [71].

Moreover, if the mode itself is anharmonic, i.e. the forces acting on an atom when atoms are displaced from equilibrium are proportional not only to the first power of the displacements but also to some other higher powers, further broadening will occur and the peak position will be dependent on temperature as studied in section 3.2.4. For instance, the time evolution of the T_{1N} mode at 1,600K is shown in figure 3.3 and its Fourier transform in figure 3.4 (a). It

shows that the phonon spectrum is very noisy and it is difficult to determine ω_s. Fortunately, in the present case we found that it was always possible to unambiguously identify the peak by using a smoothing spectrum method and maximum entropy method, see appendix A. The smoothed spectrum is shown in figure 3.4 (a) and (b).

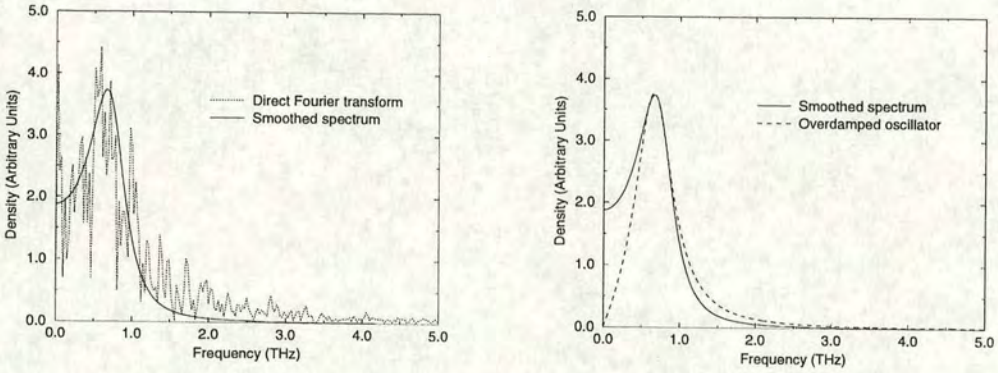

a) b)

Figure 3.4: a) The Fourier transform of the normal mode in figure 3.3. The broad peak around $\omega = \omega_s$ reflects the strong anharmonicity. b) The phonon spectrum is modelled by a damped oscillator with $\Gamma = 0.6$THz.

One important feature is that this anharmonic phonon can be modelled by a damped oscillator the displacements of which are exposed to a damping mechanism with a damping factor, Γ. The effect of Γ is to broaden a peak around ω_s by the relation [74, 75, 77]

$$P(\omega) \propto \frac{\Gamma\omega}{(\omega^2 - \omega_s^2)^2 + (\Gamma\omega)^2}. \tag{3.15}$$

The vibrational amplitude decays with a relaxation time τ, where

$$\tau = \frac{1}{\pi\Gamma}. \tag{3.16}$$

By fitting equation (3.15) to the phonon spectrum, see figure 3.4 (b), we found that the frequency of the T_{1N} mode at 1,600K is 0.7THz, Γ is 0.6THz and τ is 0.5ps. Notice that $\tau < 2\pi/\omega_s$ which indicates that T_{1N} phonon in zirconium behaves as a damped oscillator. In real zirconium [7], the damped behaviour is quite similar, i.e. $\Gamma = 0.8$THz at $\simeq$ 1,600K. In fact we found that this broadening effect happens in all phonon modes in the N-Γ branch in our simulations.

The T_{1N} phonon in zirconium exhibits strongly anharmonic nature and can be modelled by a damped oscillator with $\Gamma = 0.6$THz.

3.2.2 Phonon Dispersion Curve

In order to construct the finite temperature phonon dispersion curve, we simulate 8,192 bcc atoms at 1,400K and since our calculations are designed to study very anharmonic phonons, we avoid all difficulties and ensure the statistical reliability by calculating phonon frequencies direct from the time evolution of normal mode coordinates as in equation (3.4) from a long simulation, i.e. 40ps.

ξ	T_1	T_2	L
0.0625	0.52	0.86	1.86
0.1250	1.06	1.75	3.50
0.1875	1.56	2.84	4.57
0.2500	1.57	3.86	5.17
0.3125	1.91	4.49	4.79
0.3750	1.79	5.09	4.21
0.4375	1.20	5.40	3.60
0.5000	0.53	5.51	3.33

Table 3.1: The phonon frequencies in the $\mathbf{q}_1 = [\xi\xi 2\xi]$ branch (Γ-N in figure 3.5) calculated from the normal mode method at 1400K. Note that T_1 and T_2T denote transverse phonon modes and L denotes longitudinal phonon modes.

In the simulation box, there are only a certain number of wavevectors that are allowed due to the finite number of atoms. The possible wavenumbers $\mathbf{q}$ are

ξ	T_1	T_2	L
0.0625	0.08	1.06	0.58
0.1250	0.16	2.10	1.16
0.1875	0.32	3.14	1.69
0.2500	0.40	3.92	2.18
0.3125	0.49	4.66	2.71
0.3750	0.59	5.12	3.02
0.4375	0.56	5.38	3.19
0.5000	0.53	5.51	3.33

Table 3.2: The phonon frequencies in the $\mathbf{q}_2 = [\xi\xi 0]$ branch (N-Γ) calculated from the normal mode method at 1400K.

given by integers n_x, n_y and n_z such that [48]

$$\mathbf{q} = \left(\frac{2\pi n_x}{a}, \frac{2\pi n_y}{b}, \frac{2\pi n_z}{c}\right), \tag{3.17}$$

where a, b and c are the lengths of the axes of the orthorhombic simulation cell. The maximum allowed values of n_x, n_y and n_z are determined by the number of the bcc primitive unit cells along each axis. The present phonon dispersion relation is projected along four branches which are $\mathbf{q}_1 = [\xi\xi 2\xi]$, $\mathbf{q}_2 = [\xi\xi 0]$, $\mathbf{q}_3 = [00\xi]$ and $\mathbf{q}_4 = [\xi\xi\xi]$. The factor $2\pi/a$ is omitted from these $\mathbf{q}_i$. The eigenvectors are determined from a lattice dynamics calculation at 0K. The determination of the eigenvectors is important in the Γ-N-Γ branches, because these branches are highly anharmonic and the phonon spectra will be broad and it may become difficult to identify a correct frequency unambiguously. If $\mathbf{e}$ in equation (3.4) or (3.5) is not of a normal mode, the Fourier transform will consist of peaks at each of the normal modes of which $\mathbf{e}$ is comprised and hence it will be more difficult to extract the frequencies.

The results (dashed line) are reported in tables 3.1-3.4 and compared with the neutron scattering data (circles) [7] for zirconium at 1,188K in figure 3.5. The results are generally in good agreement with the experiments. Since the potential was not fitted to any properties of this bcc structure this gives us confidence in

ξ	T	L
0.1250	0.85	1.25
0.2500	1.69	2.46
0.3750	2.64	3.39
0.5000	3.43	4.13
0.6250	4.13	4.53
0.7500	4.49	4.65
0.8750	4.72	4.84
1.0000	4.76	4.76

Table 3.3: The phonon frequencies in the $\mathbf{q}_3 = [00\xi]$ branch (Γ-H) calculated from the normal mode method at 1400K.

ξ	T	L
0.1250	0.86	2.63
0.2500	1.97	4.43
0.3750	3.23	5.00
0.5000	4.26	4.26
0.6250	4.38	2.18
0.6666	4.60	1.79
0.7500	4.80	2.34
0.8750	5.03	4.07
1.0000	4.76	4.76

Table 3.4: The phonon frequencies in the $\mathbf{q}_4 = [\xi\xi\xi]$ branch (H-P-Γ) calculated from the normal mode method at 1400K.

the potential; the potential is a good representation for β zirconium.

3.2.3 Instability of $[\xi\xi 2\xi]$ and $[\xi\xi 0]$ Branches

An anomaly in the bcc phase is that the dispersion in the lowest N-Γ branch is unstable at 0K when anharmonicity is absolutely absent. This can be readily shown by lattice dynamics [79] because unlike the experiment and the MD, which measure the correlation functions, the lattice dynamics method directly measures the harmonic term in the potential energy surface where the anharmonic effects are not incorporated, although in the quasiharmonic approach the lattice dynamics is performed at the different lattice parameters corresponding to varying the

temperature. The lattice dynamics calculation has been done as follows. The force constants and the dynamical matrix elements can be obtained analytically from doubly differentiating the potential [80]. The frequencies are then calculated by diagonalising the dynamical matrix. This is an eigenvalue problem. By this method, the eigenfrequencies and eigenvectors can be evaluated simultaneously. The lattice dynamics results (solid line) [48] for the current potential at a bcc lattice parameter of 3.67$\AA$ (corresponding to 1,400K) are also plotted in figure 3.5. It shows a good agreement with both the experiment and the MD.

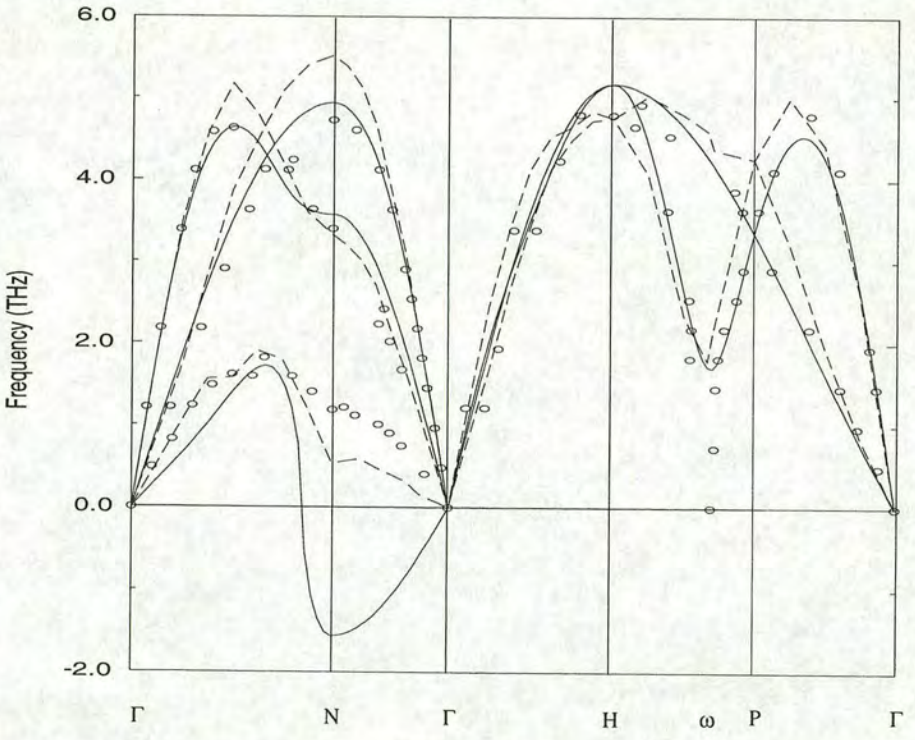

Figure 3.5: Shows the phonon dispersion curve in the bcc lattice at T = 1,400K by using the normal mode calculation (dashed line) taken from the MD, compared with the experimental data (circle) [7] at 1,188K and the results from the lattice dynamics (solid line) with volume corrections [48].

Notice that there is a dramatic exception in the $[\xi\xi 2\xi]$ and $[\xi\xi 0]$ branches, where the harmonic phonon frequency is imaginary - i.e. the expanded bcc lattice is unstable with respect to this distortion. The failure of the lattice dynamics

calculation to reproduce the experimentally observed behaviour provides crucial evidence for the essence of anharmonicity in the bcc structure stabilisation. Moreover it explains why the visualisation method used in our previous work [25] and in section 5.1.4 - quenching the structure to 0K and examining the neighbours of each atom - never gives any bcc-coordinated atoms.

It is worth emphasising that the $[\xi\xi 2\xi]$ and $[\xi\xi 0]$ branches are stabilised in the MD at high temperature where the anharmonicity is fully included via the potential. The only discrepancy is in the value of the N-Γ branch phonons which are somewhat lower than experiment. One possible explanation is that the phase transition temperature for the potential is higher than for real zirconium (see also section 5.2.1). Another explanation would be that the electronic structure, which is not fully covered by the present potential, has an effect on the frequency of the phonon branch as well as the anharmonicity. Note that a full electronic structure calculation also gives this phonon instability. These underestimated frequencies of the N-Γ branch also happen in all other forms of the zirconium potential as reported by May, *et al.* [12] using a Born-Mayer type and a Morse type potentials, and by Willaime and Massobrio [14] using a form of the embedded-atom method (EAM) potential and by Morris, *et al.* [43] using another form of the EAM potential.

By comparing the lattice dynamics method, where anharmonicity is absent, to the MD calculations, strong evidence is provided that anharmonicity plays an important role in stabilising the bcc phase.

3.2.4 Temperature Dependence of T_{1N} Phonon

The frequency of the T_{1N} phonon is calculated by the MD and equation (3.4) in the constant volume and constant temperature (NVT) mode at 1,400K, 1,600K

and 1,800K for 40ps and averaged over 12 samples. The eigenvector is determined by experiment [7] which is $\mathbf{e} = [1\bar{1}0]_{bcc}$. The results are shown in figure 3.6 and compared with some previous work [7, 13, 14]. The T_{1N} phonon appears to soften a little towards the transition temperature. The softening slope in our calculations is 0.3 THz/1,000K compared with the slope of 0.8 THz/1,000K from the experiment [7], 2.0 THz/1,000K from an *ab initio* calculation [13] and 0.15 THz/1,000K from another form of many-body potential for zirconium [14]. Apart from this unrealistically low frequency of the T_{1N} mode, the slope from the interatomic potentials using the MD simulations seems to have the same order as that from the experiment. This softening agrees with Zener's picture of the structural phase transitions [9] and is a precursor effect of the bcc-hcp transition in zirconium. However, in Zener's picture, the frequency of the phonon must drop to zero while the phase transition is occurring. This is in contrast with our finding; the frequency is finite at the phase transition as we shall see later in section 3.3.1.

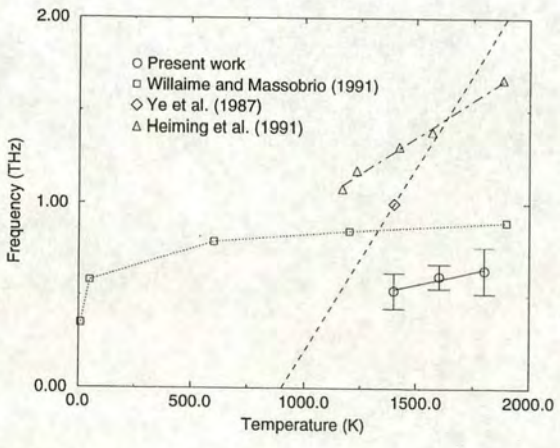

Figure 3.6: Illustrates the temperature dependence of the T_{1N} phonon between 1,400K-1,800K taken from our MD simulations [48] compared with an *ab initio* calculation by Ye, *et al.* [13], an MD simulation by Willaime and Massobrio [14] and the experimental data by Heiming, *et al.* [7].

There is an interesting point in the positive slope of the T_{1N} mode. In the harmonic regime while the crystal is expanding, the elastic energy is also increasing. This may be compensated by a lowering of the phonon frequencies which will result in decreasing the free energy of the system. This leads to a negative slope of the softening [71]. This is consistent with the quasiharmonic approach [81]. It predicts that the T_{1N} phonon in our potential becomes stiffer with reduced volume (i.e. reduced temperature). Again, when the anharmonic effects are included as in the MD, the positive slope is reestablished. This confirms the importance of the anharmonicity to correctly reproduce another behaviour of the bcc zirconium.

3.2.5 Phonon Density and bcc-hcp Transition

In this section we will illustrate the link between the anomalous low frequency phonons and the bcc-hcp transition via the phonon density curves. First of all, we must calculate the phonon density in the bcc phase at various temperatures. Dickey and Paskin [72] showed that in a classical lattice the phonon density, $\mathcal{F}(\omega)$, is related to the atomic velocity autocorrelation, $\gamma(t)$, by the relation

$$\mathcal{F}(\omega) = \frac{1}{2\pi} \int \gamma(t) \cos(\omega t) dt, \tag{3.18}$$

where the normalised $\gamma(t)$ is defined as

$$\gamma(t) = \frac{< \sum \mathbf{v}_i(t) \cdot \mathbf{v}_0(0) >}{< \sum v_0^2(0) >}, \tag{3.19}$$

where $v_0^2(0) = \mathbf{v}_0(0) \cdot \mathbf{v}_0(0)$ and $\mathcal{F}(\omega)$ must obey the normalisation condition,

$$\int \mathcal{F}(\omega) d\omega = 1. \tag{3.20}$$

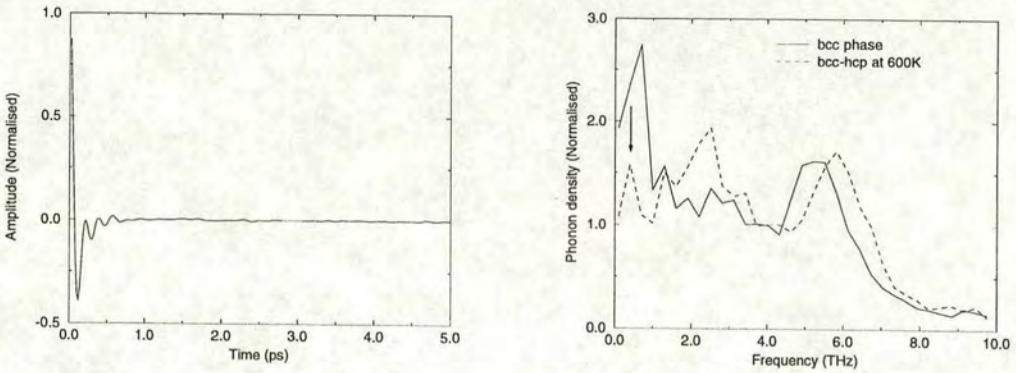

a) b)

Figure 3.7: This graph shows a) a section of typical velocity autocorrelation $\gamma(t)$ taken from the MD simulation of the bcc lattice with 8,192 atoms at 1400K, b) the Fourier transform of $\gamma(t)$ representing the phonon density in the bcc lattice at 1,400K (solid line) compared with the phonon density during the bcc-hcp transition at 600K (dashed line).

In the present case, $\gamma(t)$ is sampled in the canonical ensemble (NVT). The ensemble average of $\gamma(t)$ in equation (3.19) can be estimated from the average of the velocity autocorrelation in our MD simulations over the different time origins, t_0, [58, 82] as

$$< \sum \mathbf{v}_i(t) \cdot \mathbf{v}_0(0) > \cong \frac{1}{t_{max}} \sum_{t_0}^{t_{max}} \sum_i \mathbf{v}_0(t_0) \cdot \mathbf{v}_i(t_0 + t). \qquad (3.21)$$

The ensemble average notation $< ... >$ in this equation implies that the ergodic hypothesis must be essentially invoked by allowing large enough t_{max}. We have used $t_{max} = 10$ps. The simulation contains 8,192 atoms and the phonon density curves are averaged over 3 different runs to ensure that each mode of the phonons is sampled sufficiently and the correct phonon density is produced. This method has been used for studying the phonon density in NiAl alloys [21] and in krypton [72] and is in a good agreement with experiment.

Amplitude variation for a typical $\gamma(t)$ in the bcc phase at 1,400K is shown in

figure 3.7 (a). The Fourier transform representing the phonon density at 600K and 1,400K is shown in figure 3.7 (b). We found that at 600K the phonon density of the anomalous low frequencies around 0.5THz is considerably lowered, indicated by the downward arrow in the figure. From the dispersion curve in figure 3.5, the only branch which contains these peculiar low frequencies is the $[\xi\xi 0]$ branch. There is a corresponding phase change occurring.

Because the simulations have been done in the constant volume mode, one possible way to detect the phase transition is to monitor the time evolution of the internal stress tensor components, $\Pi_{\alpha\beta}$ in equation (2.24). The result is shown in figure 3.8 (a) after the hydrostatic pressure is subtracted. It is clearly seen that the internal stress tensor components gradually change from zero at $t = 2.0$ps to some finite values at $t = 12.0$ps showing a period of the structural change and evidencing the first order transition. The simulation box no longer behaves as a cubic system but rather as a rhombic system as illustrated diagramatically in figure 3.9 (b).

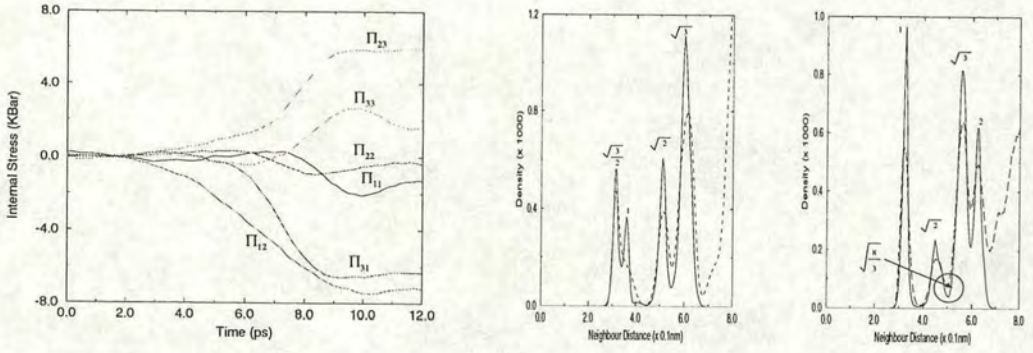

Figure 3.8: Illustrates the structural change at 800K using a) the time evolution of $\Pi_{\alpha\beta}$, defined in equation (2.24); b) RDF at t < 2.0ps; c) RDF at t > 12.0ps.

The overall lattice structure can be determined by examining the radial distribution function (RDF) of the system, see section 5.1.1 for more detail. The

coordination numbers in each coordination shell change from that of the bcc (figure 3.8 (b)) to one of the close-packed structures (figure 3.8 (c)). The dashed lines in (b) and (c) are the RDF before eliminating some thermal fluctuation in the atomic positions. The procedure for eliminating thermal fluctuation will be discussed in section 5.1.5. The numbers in figure 3.8 (b) and (c) are the marks of the coordination shells. The correct structure can not be determined directly from figure 3.8 (c) as the small peak at c_{hcp} (indicated at the position in a big circle in the figure) that distinguishes the hcp from the fcc is absorbed into nearby bigger peaks, though we shall see later that in fact the hcp is the dominant close-packed structure in the martensite phase. The detail of structural determination will be fully reviewed in section 5.1.

Once we know the normalised phonon density $\mathcal{F}(\omega)$, the vibrational entropy per atom can be estimated in the harmonic regime [77, 78] as

$$S = -3k_B \int d\omega \mathcal{F}(\omega)[n(\omega)\ln n(\omega) - (1+n(\omega))\ln(1+n(\omega))], \qquad (3.22)$$

where $n(\omega) = (e^{\hbar\omega/k_BT} - 1)^{-1}$. By using this equation and figure 3.7 (b), we found that the difference in the vibrational entropy per atom between the bcc and the hcp is $0.73k_B$. It is higher than the experimentally derived value, which is $0.26k_B$ [7]. However, this demonstrates that lowering the phonon density relates to decreasing the vibrational entropy.

The bcc-hcp transition in zirconium is driven by the excess vibrational entropy. The entropy difference in our calculations is $0.73k_B$.

As we mentioned earlier in section 1.2.2, there are several theoretical approaches studied by Kerr and Rave [15], Morris and Gooding [16, 17] explaining that the excess vibrational entropy stabilises the high temperature phase. The phase change at lower temperature is a consequence of the decreasing vibrational

entropy. This confirms that the lowering of the low-energy phonon states prior to the bcc-hcp transition has a connection with the origin of the transition which is consistent with our findings.

A distinctive contrast between the calculation and the experimentally derived phonon density curve is that the phonons in the bcc phase, as represented by our potential, occupy anomalously low-frequency states. Hence the entropy difference is quantitatively incorrect. This might be the result of the absence of the electronic entropy which has been associated with the bcc stabilisation in real zirconium. In order to obtain enough vibrational entropy the phonons must have very low frequencies because these phonons can be excited easily and as a consequence have high density of states and higher entropy. Thus the essential amount of entropy for stabilising the bcc structure can be compensated for the absence of the electronic part by these peculiar low-frequency phonons.

Theoretically the electronic entropy is calculated for perfect bcc - in practice this structure is unstable because of the gain in electronic energy when the T_{1N} phonon is excited. In fact, the electronic entropy is a minor effect [7] on the bcc stabilisation; we have seen throughout this chapter that the bcc structure is indeed stabilised by the effect of the anharmonic vibration alone, providing that the vibrational amplitude is sufficiently large, i.e. at high temperature.

Using the first-principles calculations to estimate the electronic contribution to the entropy in titanium, Craievich, *et al.* [83] found that the electronic part gives rise to 1/3 of the total entropy required for stabilising the bcc at the transition temperature and it would require temperature of 4,000K, in the absence of the mechanical part, to stabilise the bcc phase counting on the electronic entropy alone. This is impossible because in this case the transition temperature is much higher than the melting point (1,660K) of titanium.

3.3 The hcp Phase

At temperatures lower than 1,333K, zirconium has the hcp structure. As we have seen, the vibrational entropy is no longer sufficient to stabilise the bcc phase. In this section, we study the vibration of the T_{1N} phonon while the phase transition is happening until the system reaches an equilibrium in the hcp phase. The main interests will be in the frequency of the phonon and its temperature dependence and the connection between the phonon and the reverse (hcp-bcc) transition. The way to induce the reverse transition is introduced and the structural study will be established.

3.3.1 T_{1N} Phonon in Low Temperature Phase

When the system undergoes a phase transition to the low temperature hcp structure, there are six possible hcp (martensite) variants which can occur, each corresponding to the NW transformation (see section 1.2.2) involving a particular T_{1N} mode. In fact there are 12 symmetrically equivalent N-points in the bcc Brillouin zone for this mode, but because of inversion symmetry these give rise to only six inequivalent martensite variants. In the present work, it has been shown that only a subset of two or three of these variants are selected in one simulation, depending on the specific martensite growth plane, and a strain compensating the microstructure involving these three hcp variants is formed [25]. The study of the martensite microstructure will be discussed extensively in chapters 4 and 5.

While taking zirconium through the bcc-hcp transition at 200K, 600K and 1000K, we have continued to evaluate the time evolution of the coordinate $\alpha_N(t)$, which corresponds to the T_{1N} mode through equation (3.4). According to the transformation mechanisms, within a single variant, one of the $(110)_{bcc}$ planes becomes the basal plane in the hcp structure, four become pyramidal planes and one becomes a prism plane. As a result, the N-point in the bcc reciprocal space

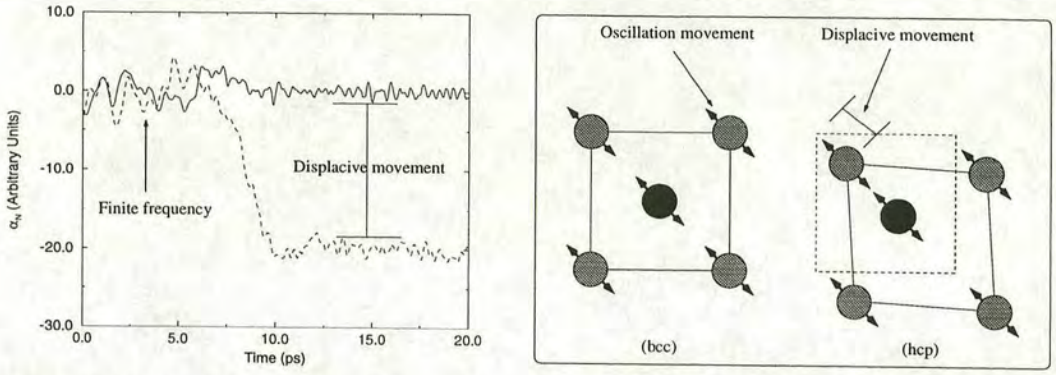

Figure 3.9: a) The time evolution of the T_{1N} modes following rapid cooling from 1,400K-1,000K in the MD simulation with 8,192 atoms. b) A construction diagram of the bcc-hcp transition.

no longer exists in the hcp phase and the α_N coordinate no longer describes a normal mode. However, the fluctuation and the displacement of the coordinate α_N can still be detected. The typical time evolution of the normal mode following rapid cooling from 1,400K-1,000K is shown in figure 3.9 (a). It exhibits several main features as follows.

Firstly, in the bcc phase just before the phase transition, large fluctuations of those planes are (by construction) around zero displacement, i.e. $< \alpha_N(t) >= 0$, and have a finite frequency. At the starting point of the transition, the fluctuation of 2 or 3 T_{1N} modes (dashed line in figure 3.9 (a)) is almost instantaneously displaced away from zero point, i.e. $< \alpha_N(t) >$ changes from zero to a finite value, indicating displacive movements in atomic planes due to a structural change as illustrated in figure 3.9 (b). In this figure, the T_{1N} phonon is reconstructed in real space and projected on $(001)_{bcc}$ plane. Different shades denote different layers of the atomic planes. It shows that the bcc lattice has been distorted and displaced during the bcc-hcp transformation. The displacement is described by the discrete shift in figure 3.9 (a) and the distortion is described by $\Pi_{\alpha\beta}$ in figure 3.8 (a). The

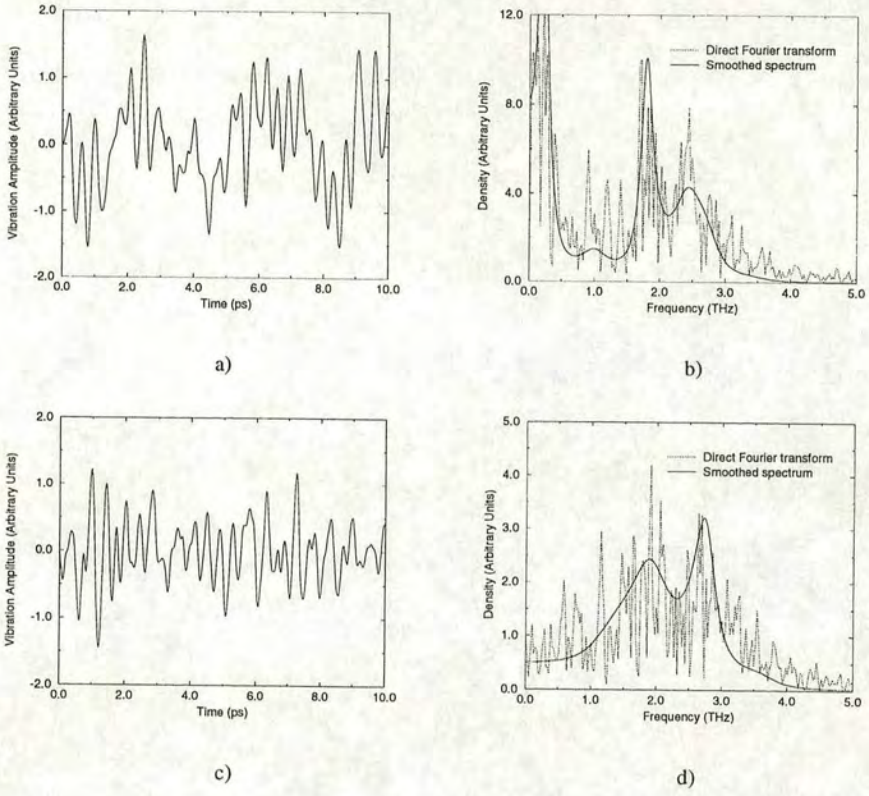

Figure 3.10: A typical time evolution of T_{1N}-equivalent modes in the hcp phase taken from the MD simulation with 8,192 atoms at 1,000K. a) This mode concerns the microstructure formation. c) This mode is not involved in the microstructure formation. The Fourier transform and smoothed spectrum of (a) and (c) are shown in (b) and (d) respectively.

oscillation movement of the atomic planes in figure 3.9 (b) is symbolised by $\leftrightarrow$. These chosen T_{1N}-equivalent modes will manifest themselves as the corresponding hcp variants in the resulting microstructure. Furthermore, the magnitude of the displacements is related to the amount of each variant in that microstructure, but not in a straightforward way because both positive and negative $< \alpha_N(t) >$ give rise to the equivalent hcp variants. After a new equilibrium is reached, these modes have a stable oscillation movement which is composed of a few higher frequencies.

On the other hand, the T_{1N} modes (solid line in figure 3.9 (a)) which are

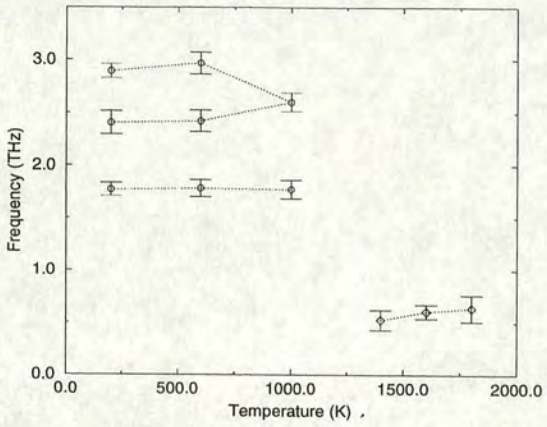

Figure 3.11: The frequency of the T_{1N} phonon in the hcp phase (circle) at 200K, 600K and 1,000K compared with the frequency of the same mode in the bcc phase (diamond). Note that the dotted lines are a guide line only.

related to variants which do not appear in the microstructure do not exhibit the discrete shift of the $< \alpha_N(t) >$. They have had large fluctuations with a finite frequency around zero displacement before the phase transition happens. After the transition, the frequency is shifted to a mixed mode of higher frequencies.

Secondly, to find whether the T_{1N} mode has an equivalent normal mode in the hcp phase after the transition, we took a Fourier transform of $\alpha_N(t)$ in the hcp phase. The data is rather noisy, so we have applied the maximum entropy method (appendix A) across 6 various runs to distinguish the peaks. Typical results at 1,000K are shown in figure 3.10. For the α_N (figure 3.10 (a)) involved in the transition its Fourier transform (figure 3.10 (b)) contains a large peak centred at zero in the frequency space corresponding to the slow evolution of the microstructure and the coupling of the mode to the strain. Additionally, there are two other distinct peaks at relatively higher frequencies, showing that the coordinate α_N no longer represents a normal mode. Notice that the discrete shift is subtracted from these modes prior to taking the Fourier transform.

Likewise, for the α_N (figure 3.10 (c)) not involved in the transition, there

are also two frequency peaks in the Fourier transform as in figure 3.10 (d). This indicates that there is no normal mode in the hcp which is equivalent to the mode in the bcc responsible for the transition.

Figure 3.11 shows the frequencies of these T_{1N}-equivalent modes evaluated at various temperatures. Unlike the T_{1N} mode in the bcc lattice the frequencies of these modes have split into a few normal modes at low temperature and no clear temperature dependence can be determined.

The T_{1N} mode has a finite frequency at the phase transition and subsequently exhibits a discrete shift reflecting a structural change. Its frequency has split into a few higher frequencies $\approx$ 2.5 THz.

In *ab initio* calculations, studied by Ostanin, Salamotov and Trubitsin [84], the frequency of T_{1N} phonon is calculated by deforming the bcc zirconium towards the hcp structure - the so-called 'frozen phonon method'. They found that near the transition temperature, the spectral peak of T_{1N} mode has split into 2 peaks, a low-frequency peak from the distorted bcc and a relatively higher frequency peak from the distorted hcp. This crystal structure is called intermediate phase. Ostanin, *et al.* [84] concluded that the peak is a contribution from the distorted hcp equivalent to the T_1 phonon at A point in the hcp structure. Using the neutron scattering experiment [78], the frequency of the A point phonon is 1.62 THz at 1007K. By using the lattice dynamics method with the present potential [81], the frequency is $\approx$ 2.4 THz. The frequency splitting of the T_{1N} mode at the phase transition is consistent with our results. The only discrepancy is that there are two more high-frequency peaks in the hcp in our findings. This is because, unlike in the MD simulations, the structure obtained by the frozen phonon method is not a regular hcp but rather a distorted hcp. That explains why there is only one high-frequency peak and a bcc-contributed peak still remains.

3.3.2 Perturbative Normal Mode Calculation

In this section we introduce the perturbative normal mode method. This method is very useful when we study the hcp-bcc transition in the next section. Conventionally, it is an alternative method to MD for examining anharmonic phonons, introduced by Dickey and Paskin [72]. The principle of the method is to artificially excite a specific phonon mode at a particular time. The perturbation is defined as

$$\mathbf{r}_i'(t) = \mathbf{r}_i(t) + \epsilon \cos(\mathbf{q} \cdot \mathbf{l}_i)\mathbf{e}_{\mathbf{q}s}, \tag{3.23}$$

where $\mathbf{r}'$ and $\mathbf{r}$ are the perturbed and the unperturbed atomic positions respectively and ϵ is the strength of the perturbation, specified in the units of a_{bcc}. Only one selective phonon mode will be examined at one time. If we attempt to excite a non-normal mode, the lattice vibration will be of the normal modes of which the non-normal mode is comprised. Owing to the anharmonic nature of zirconium, the energy is transferable between phonon modes. The additional energy of the perturbed mode is dispersed into other modes soon after the perturbation. Thus both the phonon frequency and its lifetime can be calculated within a short simulation period by using equation (3.4) and (3.5). Moreover, these coupled phonons will give rise to some certain states in the phonon density curve.

However, when Willaime and Massobrio [14] used this method to study the frequency of the T_{1N} phonon in the bcc structure they found that the strength of the perturbation must be as high as $0.09a_{bcc}$ to overcome the background vibration and the frequency extracted from this method is dependent on this strength parameter confirming that this phonon mode is strongly anharmonic. This turns out to be a disadvantage for the purpose of examining the strongly anharmonic phonon frequencies. Nevertheless, it is suitable for studying the inverse transition as we shall see in the next section. This is because our simulations concern only the magnitude of vibration and the phonon density.

3.3.3 Induced Reverse Transition

In the hcp phase, when the temperature is raised above the transition temperature T_0, one might expect a reverse (hcp-bcc) transition. Nevertheless, in our MD timescale such a transition never happens. We suspected [48] that this may be the result of the splitting of the T_{1N} phonon into 2-3 higher-frequency modes and these phonons are difficult to excite.

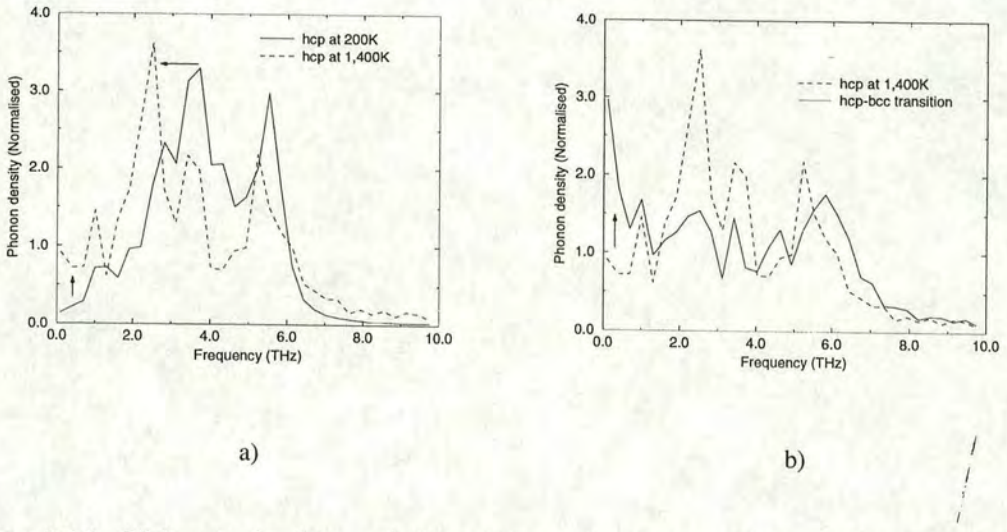

Figure 3.12: This graph shows a) the phonon density in the hcp phase at 200K (solid line) and 1,400K (dashed line); b) the phonon density during the induced hcp-bcc transition at 1,400K (solid line) compared with the density in the hcp phase at 1,400K.

To investigate the reverse transition, we calculated the phonon density in the hcp phase at 200K and 1,400K. The latter is just above T_0. The results are shown in figure 3.12 (a). The phonon density at 200K agrees very well with the quasiharmonic approach of Williame and Massobrio [14]. This reflects the harmonic nature of the hcp phase at low temperature. We found that when the temperature was raised, high-frequency states around 4.0THz of the phonon density had shifted to lower frequency states around 2.0THz indicated by the horizontal arrow in figure 3.12 (a). The low-frequency states around 0.5 THz are increased somewhat, marked by the vertical arrow. These results point out that

in fact the system is lacking in low-frequency vibrations, the bcc structure is thus not stabilised and the system does not undergo the reverse phase transition on the timescale and lengthscale of our calculation.

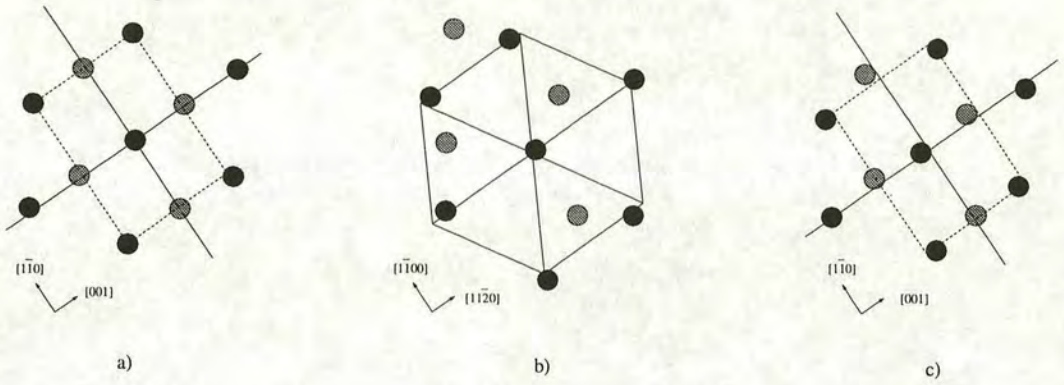

Figure 3.13: a) The initial bcc structure; b) the microstructure in equilibrium after the bcc-hcp transition showing that the structure is in fact the hcp; c) the microstructure after the induced reverse transition showing that the local structure has transformed back to the bcc. Black and grey circles label different layers. (a) and (c) are projected on $(110)_{bcc}$ whereas (b) is projected on $(0001)_{hcp}$.

This leads us to adopt equation (3.23) to artificially excite a phonon in the martensitic microstructure. We have applied $\mathbf{q}_N = 0.5[110]_{bcc}$ and the eigenvector $\mathbf{e}_{\mathbf{q}s} = [1\bar{1}0]_{bcc}$ to (3.23). This is simply the T_{1N} mode in the bcc. Even though the phonon mode is defined in the bcc system, it is also applicable in the martensitic microstructure as we know exactly which directions in the microstructure correspond to the directions in the bcc. The perturbative MD simulation is done at 1,400K where the bcc structure is stable.

In order to induce the reverse transition we found that the minimum strength of the perturbation of $0.06a_{bcc}$ must be employed. The frequency of the mode after the perturbation is 0.8THz, little higher than that of the bcc lattice at the same temperature because of the effect of the perturbation. This mode is soon dispersed into other phonon modes and the energy has been transferred. We found that the perturbation gives rise to low-frequency phonon density. Figure 3.12 (b)

clearly shows that the density of low-frequency phonons, around 0.5THz, is noticeably raised at the phase transition identified by the upward arrow. By using equation (3.22) and figure 3.12 (b), the vibrational entropy difference between the hcp and the bcc is $0.71k_B$. This is in a good agreement with value estimated in section 3.2.5. Besides, the bcc phase is then stabilised. A series of typical structures is shown in figure 3.13. There are atomic configurations taken from tiny regions of typical simulations and projected onto $(110)_{bcc}$ plane. Starting from the bcc structure in figure 3.13 (a), we get the martensitic microstructure by rapidly cooling the bcc structure from 1,400K to 1,000K. The local structure in the microstructure appears to be dominated by the hcp structure as in figure 3.13 (b). It is clear in the figure that $(110)_{bcc} \parallel (0001)_{hcp}$ and $(1\bar{1}0)_{bcc} \parallel (1\bar{1}00)_{hcp}$. These are in fact the NW rules, equation (1.3) and (1.4).

After the perturbation, the inverse transition is induced and the microstructure evolves into the structure shown in figure 3.13 (c) which is in fact the bcc structure which has the same orientation as in (a). Hence the reverse transition mechanism also obeys the NW mechanism. Notice that there is some thermal fluctuation remaining in the atomic positions. The pressure curve of figure 3.14 shows that the simulation supercell transforms back to a cubic system and exhibits a first-order transition.

The induced hcp-bcc transition is first-order and obeys the NW path of transformation. The entropy difference is $0.71k_B$.

The results from our calculations indicate that following the NW path the reverse transition would require a few phonon modes in the hcp phase. It would be possible that in real materials the reverse transition is triggered by one phonon mode but with a different transformation mechanism from the forward transition. We believe that this may be a rather general result in a wide class of martensitic transitions, and may explain for example the different mechanisms observed for

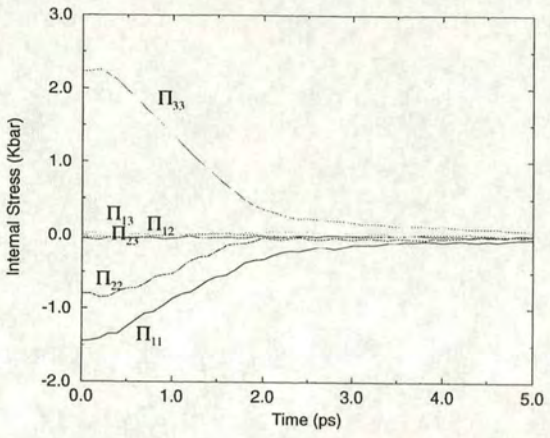

Figure 3.14: The time evolution of the internal stress tensor during the induced hcp-bcc transition at 1,400K. The stress is gradually reduced to zero after the perturbation, reflecting the transformation from rhombus to cubic supercell and exhibiting the first order transition. The overall structure is dominated by the bcc as in figure 3.13(c).

the forward and back transitions in iron where the fcc - bcc transition occurs via the Bain deformation while the reverse bcc - fcc transition follows the Burgers path [41]. Another example is NiMnGa alloys for which the forward transition occurs via $P \rightarrow M_1 \rightarrow M_2$ while the reverse transition follows $M_2 \rightarrow P$ [85], where P is the parent structure and M_1 and M_2 are the different martensitic structures.

3.4 Conclusions

In this chapter we have used the normal mode calculations to study phonon properties in the stable bcc phase at high temperature. We show that the normal mode method is in agreement with the neutron scattering data. To verify the model potential and the normal mode calculations, we construct the phonon dispersion curve and compare with the lattice dynamics calculations and the data

from the neutron scattering experiment. The results are in a good agreement for the bcc lattice. We extensively study the phonon density in the bcc and hcp phases and during the bcc-hcp and hcp-bcc phase transitions. We detected the phase changes by monitoring the internal stress tensor of the system. The overall lattice structure is determined by the radial distribution function. The local structures are illustrated. The links between phonon properties and the phase transitions are established and give the following conclusions.

In the bcc phase, the T_{1N} mode showed strong anharmonicity. This mode can be modelled by a damped oscillator with, for instance $\Gamma = 0.6$THz at 1,600K. By comparing the lattice dynamics method where the anharmonic effects are not included with the MD, we found that the anharmonic vibration is needed in order to stabilise the bcc phase. The anharmonic effects also cause the temperature dependence of the T_{1N} mode with a positive slope of 0.3THz/1,000K. When temperature is decreased below T_0, the phonon density around 0.5THz is lowered considerably during the transition. The vibrational entropy is decreased by $0.73k_B$. This triggers the first order phase transition from the bcc to hcp structure.

In the hcp phase, while the T_{1N} mode is evolving through the bcc-hcp transition, it is no longer a normal mode. It is composed of two frequencies at 1,000K and these frequencies are relatively higher than that of the mode in the bcc lattice. The T_{1N} mode involved in the forming of the microstructure exhibits a displacive movement in its time evolution indicating a structural transformation. In the conventional MD simulations, when the temperature is increased beyond T_0, the low-frequency states in the phonon density are insufficient to stabilise the bcc phase. This leads us to perturbatively excite the T_{1N} mode in the martensite phase. We found that while the phonon density is increased, the vibrational entropy gain is $0.71k_B$. The reverse transition is then induced and the bcc structure is stabilised.

Chapter 4

Elastic Theory of the Martensitic Phase

> "If you sit in the audience of a theatre when people are applauding, you can hear the individual handclaps of the people around you but if you listen to the applause from a long way off you hear only a rather uniform noise. This is really an average noise from the whole audience and the individual characteristics have been lost."
>
> J.S.Dugdale,
> Entropy and its Physical Meaning.

The bcc-hcp martensitic transition in zirconium involves little movement of atoms. The bcc parent lattice requires little distortion. This allows us, in a wider view, to consider the transition as an elastic deformation where transformation strain is well-defined. The individual atomic movement can be discarded. In section 4.1, we propose an elastic model which originates from the Nishiyama-Wessermann path [1]. Our elastic theory describes the relaxed simulation supercell which contains defects and several hcp variants in terms of a strained bcc crystal. The strain released from the bcc-hcp transformation can be formulated

in the form of matrix representations. These matrices can be derived by considering that each hcp variant is a distorted bcc crystal. At the phase transition, the elastic energy is gained because of the strain field of the distorted bcc crystal. As we shall see later, this increase in elastic energy can be compensated for by reducing the magnitude of the strain field. This can be done in two different ways; firstly, by introducing stacking faults into the hcp crystals, the strain can be partially suppressed. However, stacking faults themselves cause other strain fields. Thus there is a balance for the number of stacking faults present in the hcp crystals as we will discuss in section 4.1.4. Secondly, by forming a martensitic microstructure from several hcp variants the strain can be made almost to disappear. We will discuss the microstructure formation in section 4.2.4. Note that in these two sections the stacking fault energy and the twin boundary energy are neglected but they will be brought into the theory when we try to calculate the typical size of the hcp crystal in the martensitic microstructure in section 4.2.5. The results from our elastic theory will be compared with the MD simulations in this and the next two chapters.

4.1 A Single hcp Variant

In this section we study the transformation of a single bcc crystal into a single hcp crystal. The effect of stacking faults will be included in this model. We assume that the bcc, hcp and fcc structures are in perfect lattices with the lattice parameters of $a_{bcc} = 3.5886\mathring{A}$, $a_{hcp} = 3.2488\mathring{A}$ and $c_{hcp} = 5.1819\mathring{A}$ at 0K. We will encounter 3 different coordinate systems, i.e. x, x' and x''. These coordinate systems, which are useful for the simulation purposes, can be interchanged by rotational operators.

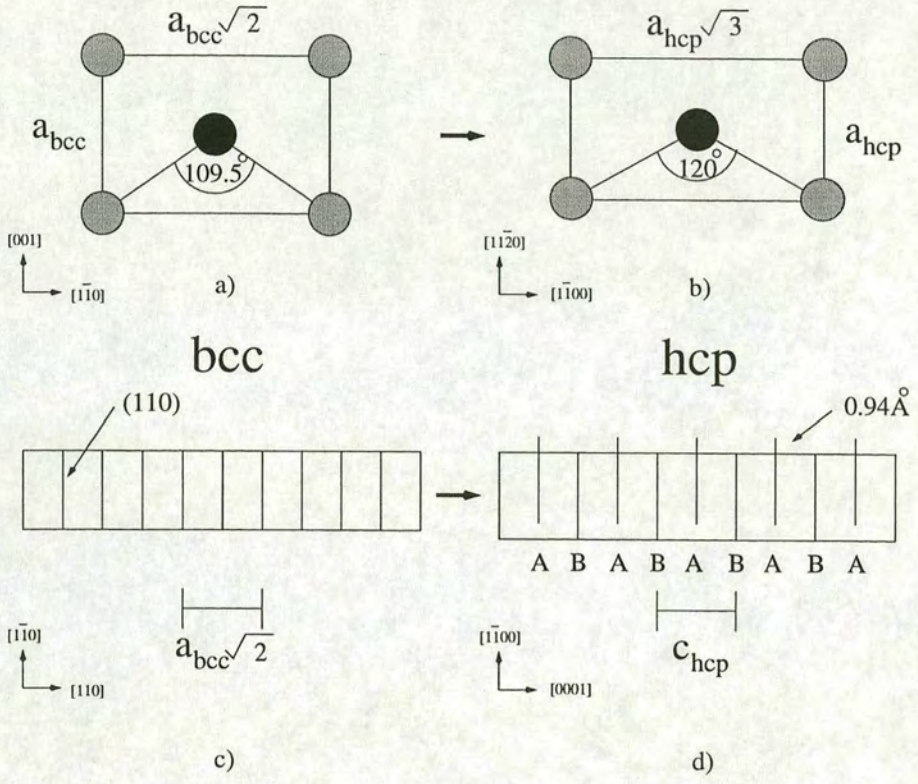

Figure 4.1: Nishiyama-Wessermann rules for the bcc-hcp transformation.

4.1.1 Nishiyama-Wessermann Rules

When the bcc lattice transforms into the hcp lattice as illustrated in figure 4.1 (a) and (b), it requires an extension in $[1\bar{1}0]_{bcc}$ by

$$\alpha^* = \frac{a_{hcp}\sqrt{3} - a_{bcc}\sqrt{2}}{a_{bcc}\sqrt{2}} \times 100 = 10.88\%, \tag{4.1}$$

and a contraction in $[001]_{bcc}$ by

$$\gamma = \frac{a_{hcp} - a_{bcc}}{a_{bcc}} \times 100 = -9.47\%. \tag{4.2}$$

These happen in order to obtain the hexagonal planes (see also figure 1.3 in section 1.2.2). The 109.5° bond angle in the bcc lattice transforms into 120°

bond angle. In other words, the plane $(110)_{bcc}$ will become $(0001)_{hcp}$. To adjust the spacing between close-packed planes, another extension in corresponding to the direction $[110]_{bcc}$ as in figure 4.1 (c) and (d) is required by

$$\beta^* = \frac{c_{hcp} - a_{bcc}\sqrt{2}}{a_{bcc}\sqrt{2}} \times 100 = 2.11\%. \tag{4.3}$$

In the final transformation, the orientation relations are

$$(110)_{bcc} \parallel (0001)_{hcp},$$
$$[1\bar{1}0]_{bcc} \rightarrow [1\bar{1}00]_{hcp}.$$

This path of transformation was proposed by Nishiyama and Wessermann [1] (NW).

The strain matrices produced by the bcc-hcp transformation can be constructed as follows. Firstly, define one of the double primed coordinate systems which is set along $\hat{\mathbf{x}}_1'' = [1\bar{1}0]_{bcc}$, $\hat{\mathbf{x}}_2'' = [110]_{bcc}$ and $\hat{\mathbf{x}}_3'' = [001]_{bcc}$. According to the NW path, this coordinate system provides the basis set for the α^*, β^* and γ strain components which lead to the transformation from a bcc crystal to a hcp variant. Because we neglect the individual atomic movement, the hcp variant can be regarded as a strained bcc crystal. Note that the individual atomic movement will be included in the theory when we consider stacking faults in section 4.1.3.

a	$\hat{\mathbf{x}}_1''$	$\hat{\mathbf{x}}_2''$	$\hat{\mathbf{x}}_3''$
1	$[1\bar{1}0]_{bcc}$	$[110]_{bcc}$	$[001]_{bcc}$
2	$[110]_{bcc}$	$[1\bar{1}0]_{bcc}$	$[001]_{bcc}$
3	$[10\bar{1}]_{bcc}$	$[010]_{bcc}$	$[101]_{bcc}$
4	$[101]_{bcc}$	$[010]_{bcc}$	$[10\bar{1}]_{bcc}$
5	$[100]_{bcc}$	$[01\bar{1}]_{bcc}$	$[011]_{bcc}$
6	$[100]_{bcc}$	$[011]_{bcc}$	$[01\bar{1}]_{bcc}$

Table 4.1: Possible coordinate systems that provide the basis sets for the bcc-hcp transformation. From now on, we will regard these coordinate systems as the double primed coordinate systems.

Secondly, by symmetry there are six different sets of $\hat{\mathbf{x}}_1''$, $\hat{\mathbf{x}}_2''$ and $\hat{\mathbf{x}}_3''$ which provide basis sets for α^*, β^* and γ. These coordinate systems are shown in table 4.1. Therefore the bcc-hcp transformation can be described by six different strain matrices corresponding to the six distinguishable variants of the hcp.

From equation (4.1), (4.2) and (4.3), the transition strain matrices, $\underline{\varepsilon}_a''$, of all six hcp variants in the double primed coordinate system can be derived as in table 4.2. Each matrix describes the transformation of the bcc crystal into a distinguishable orientation of the hcp. Hence one can derive six possible hcp martensite variants from a single bcc lattice. The same approach of constructing the strain matrices was used by Haasen [8] to study the distortion in the fcc-bcc martensitic transition via the Bain path.

$$\underline{\varepsilon}_1'' = \begin{pmatrix} \alpha^* & 0 & 0 \\ 0 & \beta^* & 0 \\ 0 & 0 & \gamma \end{pmatrix} \quad \underline{\varepsilon}_2'' = \begin{pmatrix} \beta^* & 0 & 0 \\ 0 & \alpha^* & 0 \\ 0 & 0 & \gamma \end{pmatrix}$$

$$\underline{\varepsilon}_3'' = \begin{pmatrix} \alpha^* & 0 & 0 \\ 0 & \gamma & 0 \\ 0 & 0 & \beta^* \end{pmatrix} \quad \underline{\varepsilon}_4'' = \begin{pmatrix} \beta^* & 0 & 0 \\ 0 & \gamma & 0 \\ 0 & 0 & \alpha^* \end{pmatrix}$$

$$\underline{\varepsilon}_5'' = \begin{pmatrix} \gamma & 0 & 0 \\ 0 & \alpha^* & 0 \\ 0 & 0 & \beta^* \end{pmatrix} \quad \underline{\varepsilon}_6'' = \begin{pmatrix} \gamma & 0 & 0 \\ 0 & \beta^* & 0 \\ 0 & 0 & \alpha^* \end{pmatrix}$$

Table 4.2: Six possible strain matrices which describe six hcp variants in terms of a strained bcc crystal. See also the corresponding coordinate system of each matrix in table 4.1.

A hcp crystal can be described as a strained bcc crystal, regardless of the individual atomic movements.

Note that in order to obtain a perfect hcp structure, an additional atomic movement of 0.94Å is required to shuffle every second $(110)_{bcc}$ plane into the *ABABAB* stacking sequence, see figure 4.1 (d). This movement is the result of freezing in of the T_{1N} phonon in the bcc lattice. Each variant has two possible directions of the phonon wave vector which are, however, translationally invariant and therefore give the same direction of c_{hcp} lattice parameter and hence indistinguishable variants.

4.1.2 Computational Setups

In this section, we will demonstrate how the strain matrices constructed in the last section can be compared with the simulation results. We initialise our simulation by using a regular bcc lattice and then carrying out the MD simulations at a temperature lower than the transition temperature, i.e. 600K. From section 2.3.3, we know that the simulation supercell can be described by a metric tensor $\underline{B}_o$. After the phase transition is completed - no bcc persisting - the atomic configurations are relaxed to their equilibrium positions at 0K using the constant stress algorithm (section 2.3.4). Now the simulation supercell has changed to $\underline{B}$. In the special case where $\underline{B}_o$ has only diagonal components, $\underline{B}$ can be related to $\underline{B}_o$:

$$\underline{B} = \underline{B}_o(\underline{I} + \underline{\varepsilon}). \tag{4.4}$$

This is the static case of equation (2.28). The matrix $\underline{\varepsilon}$ - in percent - can be regarded as a 'strain matrix' and can be compared with the strain matrices in our elastic theory.

However, in the last section we dealt with six coordinate systems which describe the transformation to six hcp variants. Our primary aim in this section is to describe the bcc-hcp transformation using only one specific orientation, i.e. $\hat{\mathbf{x}}'_1 = [100]_{bcc}$, $\hat{\mathbf{x}}'_2 = [010]_{bcc}$ and $\hat{\mathbf{x}}'_3 = [001]_{bcc}$. We will regard this coordinate system as the single primed coordinate system.

One advantage of introducing the strain matrices is that they transform as a tensor under an arbitrary rotation [86, 87]. For example, if $\underline{\varphi}_a$ is an arbitrary rotation matrix and $\hat{\mathbf{x}}_i''$ is transformed by

$$\hat{\mathbf{x}}_i' = \underline{\varphi}_a \hat{\mathbf{x}}_i'', \tag{4.5}$$

then the strain matrices will be transformed as a tensor by

$$\underline{\varepsilon}_a' = \underline{\varphi}_a \underline{\varepsilon}_a'' \underline{\varphi}_a^{-1}, \tag{4.6}$$

where a is 1, 2,..., 6 as in table 4.1 and 4.2. Each different system a needs a different rotation operator $\underline{\varphi}_a$. The explicit forms of the rotation matrices $\underline{\varphi}_a$ are shown in appendix B. These formulations are very useful for the converting the six strain matrices in the double primed coordinate systems into the six strain matrices in the single primed coordinate system. These strain matrices are

$$\underline{\varepsilon}_1' = \begin{pmatrix} \alpha & \beta & 0 \\ \beta & \alpha & 0 \\ 0 & 0 & \gamma \end{pmatrix} \quad \underline{\varepsilon}_2' = \begin{pmatrix} \alpha & -\beta & 0 \\ -\beta & \alpha & 0 \\ 0 & 0 & \gamma \end{pmatrix}$$

$$\underline{\varepsilon}_3' = \begin{pmatrix} \alpha & 0 & \beta \\ 0 & \gamma & 0 \\ \beta & 0 & \alpha \end{pmatrix} \quad \underline{\varepsilon}_4' = \begin{pmatrix} \alpha & 0 & -\beta \\ 0 & \gamma & 0 \\ -\beta & 0 & \alpha \end{pmatrix}$$

$$\underline{\varepsilon}_5' = \begin{pmatrix} \gamma & 0 & 0 \\ 0 & \alpha & \beta \\ 0 & \beta & \alpha \end{pmatrix} \quad \underline{\varepsilon}_6' = \begin{pmatrix} \gamma & 0 & 0 \\ 0 & \alpha & -\beta \\ 0 & -\beta & \alpha \end{pmatrix},$$

where $\alpha = (\alpha^* + \beta^*)/2 = 6.50\%$ and $\beta = (\alpha^* - \beta^*)/2 = 4.39\%$.

There is a special orientation in our simulation where the martensitic microstructure is forming. We notice that one of $< 111 >_{bcc} \approx [1\bar{2}10]_{hcp}$. The $[111]_{bcc}$ direction consists of a line of nearest neighbors in both bcc and hcp structures. Moreover there are three hcp variants of which close-packed planes are contained

in the $[1\bar{2}10]_{hcp}$ direction. Consequently, combinations of these three variants can be viewed in a planar slice, perpendicular to this direction. Thus it is convenient to set one of the axes of the initial cell along $[111]_{bcc}$. This leads us to choose an orientation system as $\hat{\mathbf{x}}_1 = \frac{1}{\sqrt{2}}[1\bar{1}0]$, $\hat{\mathbf{x}}_2 = \frac{1}{\sqrt{6}}[11\bar{2}]$ and $\hat{\mathbf{x}}_3 = \frac{1}{\sqrt{3}}[111]$. We will regard this coordinate system as the unprimed coordinate system. Again the transformation strain in this coordinate system can be obtained via a series of rotation matrices in a similar fashion as in equation (4.5) and (4.6) (see (B.12), (B.13) and (B.20) in appendix B). The results are shown in table 4.3.

$$\underline{\varepsilon}_1 = \begin{pmatrix} 2.11 & 0.00 & 0.00 \\ 0.00 & -2.68 & 9.60 \\ 0.00 & 9.60 & 4.10 \end{pmatrix} \quad \underline{\varepsilon}_2 = \begin{pmatrix} 10.89 & 0.00 & 0.00 \\ 0.00 & -5.61 & 5.46 \\ 0.00 & 5.46 & -1.75 \end{pmatrix}$$

$$\underline{\varepsilon}_3 = \begin{pmatrix} -1.49 & 2.08 & 8.31 \\ 2.08 & 0.91 & -4.80 \\ 8.31 & -4.80 & 4.10 \end{pmatrix} \quad \underline{\varepsilon}_4 = \begin{pmatrix} -1.49 & 7.14 & 4.73 \\ 7.14 & 6.77 & -2.73 \\ 4.73 & -2.73 & -1.75 \end{pmatrix}$$

$$\underline{\varepsilon}_5 = \begin{pmatrix} -1.49 & -2.08 & -8.31 \\ -2.08 & 0.91 & -4.80 \\ -8.31 & -4.80 & 4.10 \end{pmatrix} \quad \underline{\varepsilon}_6 = \begin{pmatrix} -1.49 & -7.14 & -4.73 \\ -7.14 & 6.77 & -2.73 \\ -4.73 & -2.73 & -1.75 \end{pmatrix}$$

Table 4.3: Strain matrices from the elastic theory describing the transformation from a bcc crystal to one of six hcp variants in the unprimed coordinate system.

We calculated the strain matrices directly from the MD simulation supercell with 3,456 atoms set up as discussed earlier. The crystal structure is determined by the concept of 'local structure' as described in section 5.1. The orientation of the hcp structure is defined by the direction cosine of c_{hcp} lattice parameter. The strain $\underline{\varepsilon}_a$ can be calculated using equation (4.4). In addition, the calculation of the strain components needs a reference which we choose to be a perfect bcc structure with $a_{bcc} = 3.5886\mathring{A}$. The results of the six hcp variants from the MD simulations are shown in table 4.4.

The simulation results agree very well with our elastic theory with deviation

$$\underline{\varepsilon}_1 = \begin{pmatrix} 2.12 & 0.00 & 0.00 \\ 0.00 & -2.43 & 9.24 \\ 0.00 & 9.24 & 3.76 \end{pmatrix} \quad \underline{\varepsilon}_2 = \begin{pmatrix} 10.88 & 0.00 & 0.00 \\ 0.00 & -5.51 & 5.23 \\ 0.00 & 5.23 & -1.86 \end{pmatrix}$$

$$\underline{\varepsilon}_3 = \begin{pmatrix} -1.24 & 1.94 & 7.51 \\ 1.94 & 0.98 & -4.61 \\ 7.51 & -4.61 & 3.63 \end{pmatrix} \quad \underline{\varepsilon}_4 = \begin{pmatrix} -1.33 & 7.06 & 4.18 \\ 7.06 & 6.70 & -2.64 \\ 4.18 & -2.64 & -1.90 \end{pmatrix}$$

$$\underline{\varepsilon}_5 = \begin{pmatrix} -1.23 & -1.93 & -7.46 \\ -1.93 & 0.98 & -4.60 \\ -7.46 & -4.60 & 3.62 \end{pmatrix} \quad \underline{\varepsilon}_6 = \begin{pmatrix} -1.34 & -7.07 & -4.22 \\ -7.07 & 6.71 & -2.64 \\ -4.22 & -2.64 & -1.89 \end{pmatrix}$$

Table 4.4: The results of strain matrices calculated from the six simulation supercells which transform into the six distinguishable hcp variants. The simulations were done in the constant stress mode with 3,456 atoms at 600K followed by quenching the atomic configuration to 0K.

the transition strain, the simulation results show a good agreement with our elastic theory with deviation of ± 0.26. This is a good confirmation that the bcc-hcp transformation in our simulations obeys the NW rules. The discrepancy between the theory and the simulations is that the MD simulations include the fully mechanical behaviour of the bcc phase and while the phase transition occurs, the vibrational amplitude of each atom could be as high as 0.5Å. The hcp structure obtained via the phase transition may have included some defects or some irregular structures.

4.1.3 Stacking Faults

"There's a bubble caught in the crystal and you have to shake it out."

R.P.Feynman.

Stacking faults are faults in stacking order of close-packed planes. Forming a stacking fault costs little energy. According to our potential the energy costs of stacking faults [57] are $I_1 = 41mJm^{-2}$, $I_2 = 80mJm^{-2}$ and $E = 118mJm^{-2}$,

where I_1 has only 1 layer with wrongly stacked neighbours, I_2 has 2 such layers together, and E has 3 layers of stacking faults. In the perfect hcp structure the stacking order is *ABABABAB*. However, it is worth emphasising that the bcc-hcp transformation in zirconium is an association between the strain of the unit cell and a freezing in of the N-point phonon in the bcc lattice in order to shuffle every second $(110)_{bcc}$ layer. If this shuffle does not occur co-operatively throughout the variant, i.e. the frozen phonon wave vector alters its direction at some point in the lattice, stacking faults can be formed as $\underline{B}$ in the $ABABA\underline{B}CBC$ stacking sequence. This is illustrated diagramatically in figure 4.2. The local structure of the fault will be the face-centered cubic (fcc) structure. The faults are the cause of some rotation via extra shear if they occur between even layers as shown in figure 4.2 (a). If they occur between odd layers as in figure 4.2 (b), the total rotation is zero. The existence of many faults is also a source of plastic deformation since they facilitate the creation of 'twin boundary step' (see section 4.2.3 and 5.2.3) and cause large displacements of atoms; for example, in zirconium atoms have to move by 0.94Å per stacking fault, which is about one third of the nearest neighbour distance. We show in section 6.3 that stacking faults play important roles in the deformation of the martensitic microstructure and the irreversibility of the bcc-hcp transition.

Stacking faults between even close-packed planes cause some shear but stacking faults between odd close-packed planes do not.

We now wish to modify our strain model, equation (4.1), (4.2) and (4.3) to describe shear strain contributed from stacking faults. We know that $(110)_{bcc}$ planes will transform to the hexagonal planes and stacking order will be in $[110]_{bcc}$ direction. In figure 4.2, if we cut through the *ABABABAB* stacking order at some point in the crystal and move a piece up in $[1\bar{1}0]_{bcc}$ direction by 0.94Å, we can

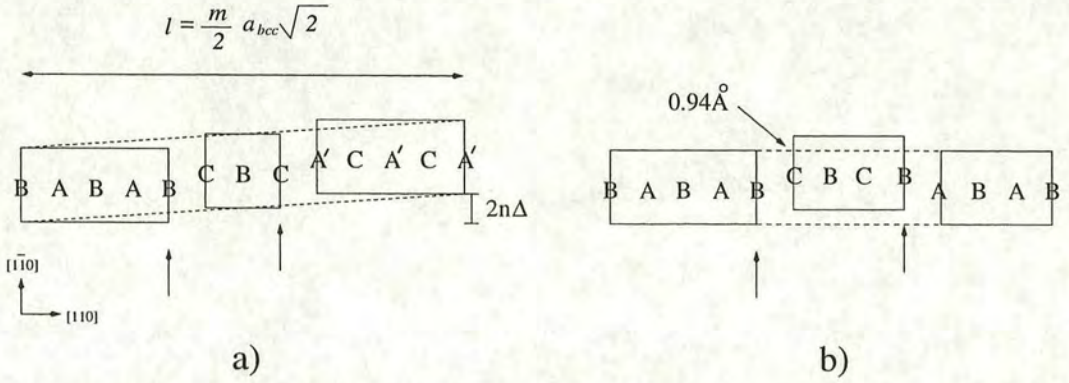

Figure 4.2: Illustrates shear strain produced by stacking faults; a) stacking faults between even close-packed layers; b) stacking faults between odd close-packed layers.

get the stacking order of $ABABA\underline{B}CBC$. The underlined letter, as well as the vertical arrows in figure 4.2, locates the local fcc structure. If the crystal is of length l, $(110)[110]_{bcc}$ shear strain of the amount $2n\Delta$ due to n stacking faults is,

$$2n\Delta = \frac{0.94}{l} \times 100\%. \tag{4.7}$$

According to figure 4.2 (a), $l = ma_{bcc}\sqrt{2}/2$ where m = total number of close-packed planes or, equivalently, total number of the $(110)_{bcc}$ planes contained in the bcc structure. This allows us to make a modification to our elastic theory by including 2nΔ into the strain matrices in the double primed coordinate system and we get, for example

$$\underline{\varepsilon}''_{1+nf} = \begin{pmatrix} \alpha^* & n\Delta & 0 \\ n\Delta & \beta^* & 0 \\ 0 & 0 & \gamma \end{pmatrix}. \tag{4.8}$$

This is for variant number 1 only. It is worthy of note that if many faults occur in the crystal, they will cause large shear and large atomic displacement.

With the help of rotational operations (equation (B.11) in appendix B), we obtain the strain matrices in the single primed system. An example of these matrices is that for the variant number 1 with n stacking faults and which is

$$\underline{\varepsilon}'_{1+nf} = \begin{pmatrix} \alpha - n\Delta & \beta & 0 \\ \beta & \alpha + n\Delta & 0 \\ 0 & 0 & \gamma \end{pmatrix}. \tag{4.9}$$

The strain matrices of other hcp variants can be derived in a similar way using equation (4.7) and table 4.2.

The results in the unprimed system are again obtained via a series of rotations. The strain matrix of variant number 1 with 2 stacking faults is shown in table 4.5 (a) compared with the result from the MD simulation in (b). We can see now that from a simple model of stacking faults in the double primed coordinate system which causes shear in a certain orientation, it turns out to be complicated shear in the unprime coordinate system. However, it is not as complicated as it looks. By numerical evaluation, we found that each component of the strain matrix in the unprimed coordinate system is linearly related to the number of stacking faults contained in the hcp crystal; see also section 4.2.2. The effect of stacking faults is illustrated in figure 4.3. The figure demonstrates shear only in the xy plane, but keep in mind that stacking faults also cause shear in the yz and the zx planes.

4.1.4 Density of Stacking Faults

In our simulations, we found that stacking faults exist even in a structure that contains only one hcp variant. As discussed earlier, this is because stacking faults are energetically cheap and thus they can easily appear and they are metastable and not easily removed. Moreover some strain field can be reduced at the expense of the existence of stacking faults.

$$\underline{\varepsilon}_{1+nf}^{theory} = \begin{pmatrix} 2.11 & 1.78 & 2.52 \\ 1.78 & -2.68 & 9.60 \\ 2.52 & 9.60 & 4.10 \end{pmatrix} \quad \underline{\varepsilon}_{1+nf}^{MD} = \begin{pmatrix} 2.68 & 2.20 & 3.06 \\ 2.20 & -2.55 & 9.12 \\ 3.06 & 9.12 & 3.58 \end{pmatrix}$$

(a) (b)

Table 4.5: Strain of the variant number 1 which includes 2 stacking faults. a) Predicted by the elastic theory; b) resulting from the constant stress MD simulation with 3,456 atoms at 600K followed by relaxing the atomic configuration to 0K. These results are in the unprimed coordinate system.

Here we will show how stacking faults can reduce the strain field. According to equation (4.9), it is readily seen that the strain field in the matrix is a minimum where

$$\alpha + n\Delta = 0, \tag{4.10}$$

and

$$\alpha - n\Delta = 0. \tag{4.11}$$

Note that the number of stacking faults cannot be negative. The condition in equation (4.10) is a minimum only when $n = 0$. From equation (4.7), the condition in equation (4.11) is minimum only when

$$\frac{n}{m} = \frac{\alpha a_{bcc}\sqrt{2}}{0.94 \times 100} \approx 0.35, \tag{4.12}$$

where n/m denotes the ratio of number of stacking faults to the total close-packed planes in the hcp crystal. This ratio can be measured directly from our MD simulations once we determine the 'local structure' of all atoms in the supercell as hcp, fcc or bcc, then we can count the number of stacking faults and the number of close-packed planes.

The number of stacking faults per total number of close-packed planes in a hcp crystal at 0K can be estimated by averaging over the two conditions in equation

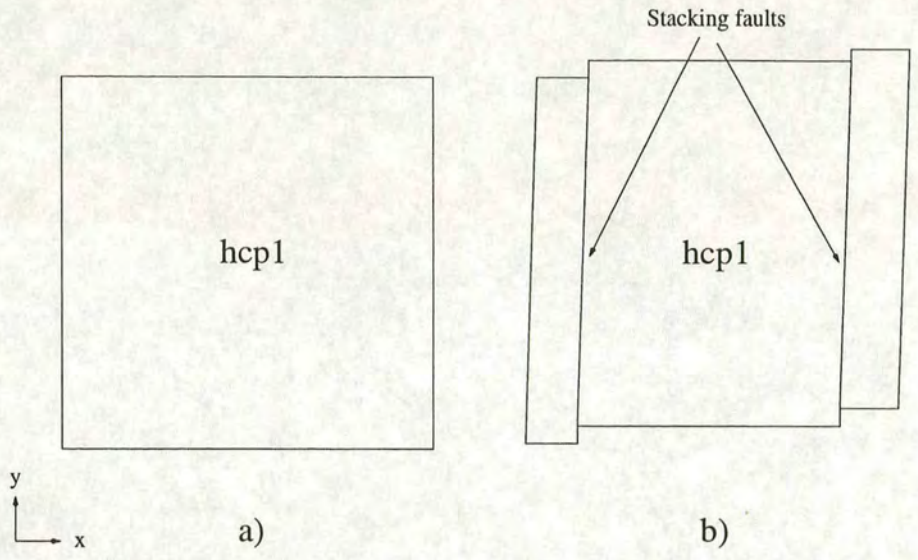

Figure 4.3: Illustrates the effect of stacking faults; a) perfect hcp crystal of variant number 1; b) the same crystal but contains 2 stacking faults.

(4.10) and (4.11), giving

$$\left.\frac{n}{m}\right|_{T=0K} \approx 0.17(5). \tag{4.13}$$

In the other words, a stacking fault is required in the hcp crystal in approximately every 6 close-packed planes in order to minimise the strain field produced by the bcc-hcp transformation.

The ratio of the planes of stacking faults to the total close-packed planes must be equal to 0.17 at 0K in order to minimise the strain field.

Now we wish to compare the equation (4.13) to the MD simulations. We set up 20 samples with different geometries and carried out the constant volume MD simulations at $\approx$ 0K, 600K, 800K, 950K and 1,200K. After the martensitic transition had finished, the atomic configurations were rapidly quenched to their equilibrium positions at 0K under the constant stress scheme. The 'local structures' were determined at 0K (see section 5.1) and the number of stacking

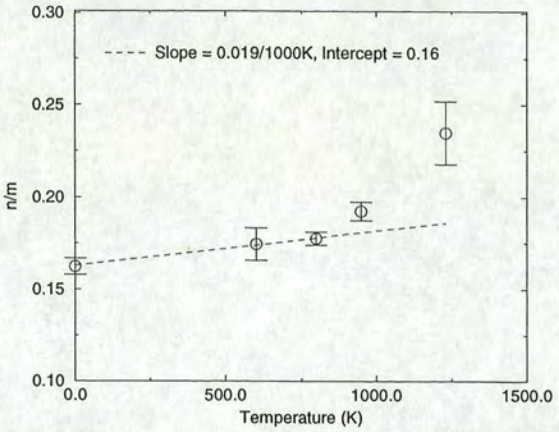

Figure 4.4: Plot of the density of stacking faults planes per total close-packed planes (circles) taken from the constant volume MD simulation followed by quenching the atomic configurations to 0K under the constant stress mode against simulation temperatures. Each point is averaged over 8 samples in different geometries (102×105×25 Å^3, 152×88×25 Å^3, 193×193×25 Å^3, 264×264×24 Å^3 and 304×176×25 Å^3). The dashed line shows a possible linear relation.

faults was measured. Then we calculated the ratio n/m. The results are plotted against the simulation temperature in figure 4.4. We found that $n/m = 0.16$ at 0K which is in a good agreement with equation (4.13). The curve also exhibits a correlation between n/m and the simulation temperature T; the dashed line in the figure shows a possible linear relation. However, the true relation is unclear.

4.2 Twinning

A twinned microstructure is defined as a formation of crystals of differently oriented variants which are separated by mirror-plane boundaries and any two variants that share a boundary are mirror images of each other. Such a boundary is called a twin boundary. The twin can be described by four twinning element, i.e. twinning plane K_1, twinning direction η_1, conjugate twinning plane K_2 and conjugate twinning direction η_2 [88]. Serra and Bacon [38] found that $(10\bar{1}1)_{hcp}$ twin

is one of the possible twin modes in zirconium and it has the lowest boundary energy. This is consistent with our results. We found that all martensitic microstructures are accommodated by the $(10\bar{1}1)_{hcp}$ twins. For the $(10\bar{1}1)_{hcp}$ twins, $K_1 = (10\bar{1}1)_{hcp}$ and $\eta_1 = [10\bar{1}\bar{2}]_{hcp}$. The conjugate elements are irrelevant in our study. The $(10\bar{1}1)_{hcp}$ twin boundary energy in our calculation is $165mJm^{-2}$ compared with $225mJm^{-2}$ calculated by Serra and Bacon [38] using Igarashi's potential for zirconium [90], $155mJm^{-2}$ calculated by Morris, *et al.* [43] using an EAM potential and $81.5mJm^{-2}$ by first-principles calculations; the twin boundary energy is consistent among different potentials and approaches. The twinning angle is 61.5°. Thus the $(10\bar{1}1)_{hcp}$ twin is an important object and will be modelled and studied by using our elastic theory. The results from the twin model will be compared with the results from the MD simulations.

4.2.1 Perfect Twins

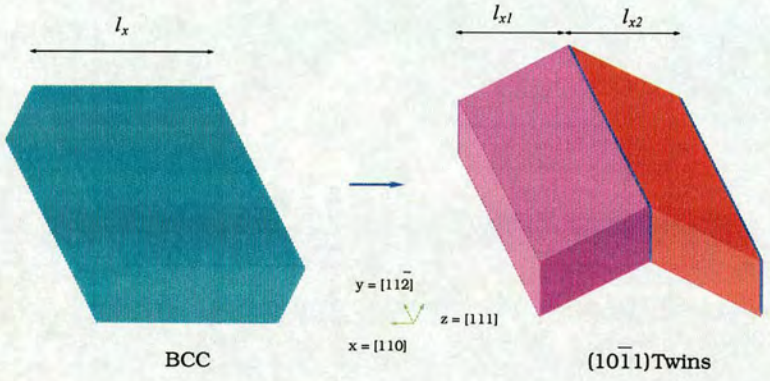

Figure 4.5: Twinned microstructure. The shape of each hcp stripe is defined by the strain matrices in table 4.3. The colour scheme is defined in table 5.1.

The aim of this section is to describe $(10\bar{1}1)_{hcp}$ twin microstructures in terms of the strain matrix of a distorted bcc crystal. For simplicity, we consider only two-striped twins. Let us assume that

- a twinned structure is a transformation of a rectangular box of a single bcc

crystal, so that $\underline{B}_o$ is diagonal,

- no change in the hcp or fcc local structure has occurred during the twinning,
- if the twin boundary lies parallel to the yz plane, the strain of the whole sample can be calculated from the average over the distance in the x direction.

From figure 4.5, the $(10\bar{1}1)_{hcp}$ twin boundary is oriented in the yz plane, the red and purple stripes are crystals of different hcp variants, l_x, is the length of the parent box in x direction and the sizes of the two twin crystals are proportional to l_x, i.e. $l_{x1} = al_x$ and $l_{x2} = bl_x$. We can calculate the average strain components ε_{ij} by

$$\varepsilon_{ij} = \varepsilon_{aij} \times \frac{l_{x1}}{l_x} + \varepsilon_{bij} \times \frac{l_{x2}}{l_x}, \tag{4.14}$$

where $\underline{\varepsilon}_a$ and $\underline{\varepsilon}_b$ are the strain matrices of 2 mirror-imaged hcp variants and l_{x1}/l_x and l_{x2}/l_x are the parameters a and b respectively, then

$$\underline{\varepsilon} = a\underline{\varepsilon}_a + b\underline{\varepsilon}_b, \tag{4.15}$$

and $a + b = 1$. The collective strain of a perfect twin can be derived using this equation from the strain matrices given in table 4.3. The twin of, for example, variants numbers 3 and 5 will have the strain matrix as in shown in table 4.6 (a) compared with the results from the MD in (b). The deviation from the elastic theory reflects the fact the structure of the hcp might have changed a little during the twin formation.

One can predict that at the bcc-hcp phase transition if we allow the system to expand, the strain component will increase from zero at the beginning of the transition to a finite value at an equilibrium in the martensitic phase. In the constant volume ensemble where the box matrix is kept fixed, the internal stress tensor components will increase, again from zero to finite values at the transition.

$$\begin{pmatrix} -1.49 & 0.00 & 0.00 \\ 0.00 & 0.90 & -4.80 \\ 0.00 & -4.80 & 4.10 \end{pmatrix} \quad \begin{pmatrix} -2.31 & 0.00 & 0.00 \\ 0.00 & 1.42 & -3.62 \\ 0.00 & -3.62 & 3.50 \end{pmatrix}$$

(a) (b)

Table 4.6: Strain of two-stripe twins composed of variants numbers 3 and 5; a) predicted by the elastic theory; b) calculated from the constant volume MD simulation followed by quenching the atomic configuration to 0K under the constant stress scheme. These results are in the unprimed coordinate system.

The theory also shows that the xy, yx, xz and zx shear components can be diminished by forming twin boundaries. In the other words, following the bcc-hcp transition the twinned microstructure can be accommodated in the sample without significant change in shape.

Twinned microstructure can also be described as a strained bcc crystal and it significantly reduces the shape change in the bcc-hcp transition.

If we shear the microstructure, the internal stress will increase. The stress keeps increasing as long as the applied shear is increased and the microstructure can persist. At a certain amount of stress, called the yield stress, the microstructure no longer tolerates the stress and undergoes some deformation modes, i.e. slips or twinnings. However, there is no a *priori* guarantee that deformation modes will be generated in the microstructure.

In our typical simulations, we encounter the deformation twinning; as described chapter 6. Thus in this section we choose to consider that the microstructure undergoes twinning deformation. It occurs by interchanging structure between the hcp variants. The variant that significantly reduces the stress will become dominant; this is one major prediction provided by the elastic theory. Even though the theory cannot produce a correct quantity for a complex mi-

crostructure, it provides qualitative explanation for the domination of a specific hcp variant in a shear system.

4.2.2 Twins and Stacking Faults

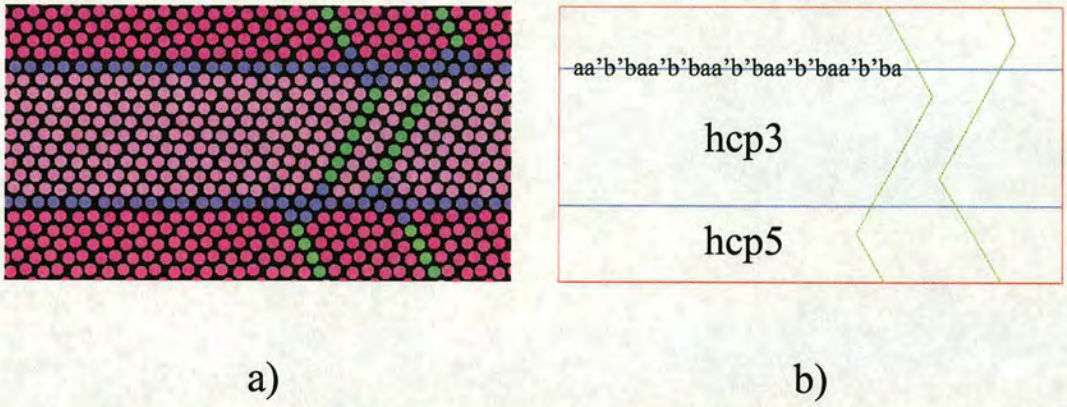

Figure 4.6: Shows the twinned structure with 2 stacking faults (green lines); a) the picture from a typical MD simulation with 9,600 atoms. The dimensions of the supercell are $51 \times 88 \times 50\mathring{A}^3$; b) a schematic diagram of (a) indicates the irregular local structures in the $(10\bar{1}1)$ twin boundary.

We have already shown that the $(10\bar{1}1)_{hcp}$ twin boundary and stacking faults have the same order of energy; see section 4.1.3 and 4.2. There is a possibility that they co-exist in the microstructure. In this section we will calculate the distortion matrix which describes a 2-striped twin microstructure with 2 stacking faults. In a twinned sample of variants numbers 3 and 5 (table 4.3) of length $l = 76.13$ Å, each variant contains 2 stacking faults and $n\Delta = 1.23$, the strain matrices are calculated by equation (4.7) and rotated via (B.20) as

$$\underline{\varepsilon}_{3+2f} = \begin{pmatrix} -0.87 & 2.43 & 8.81 \\ 2.43 & 0.30 & -3.93 \\ 8.81 & -3.93 & 4.10 \end{pmatrix}, \tag{4.16}$$

and

$$\underline{\varepsilon}_{5+2f} = \begin{pmatrix} -0.87 & -2.43 & -8.81 \\ -2.43 & 0.30 & -3.93 \\ -8.81 & -3.93 & 4.10 \end{pmatrix}. \tag{4.17}$$

The strain matrix that describes the $(10\bar{1}1)_{hcp}$ twinned structure that contains two stacking faults is shown in table 4.7 (a) compared with the MD results in (b). The strain matrices, which are directly calculated from the simulations, are in a good agreement with our theory, except there is a large shrink in the x direction and some extra shear in the yz component. Again, this indicates that the hcp structure has changed during the twin formation. The structure of twins from a typical MD simulation is illustrated in figure 4.6 (a). It shows that the local structures at the interfaces are no longer regular hcp structures but some irregular structures. By closer examination, we found that the $(10\bar{1}1)$ twin boundary is an array of two irregular structure, one with 13 local coordinations (labelled by a), the other with 11 local coordination (labelled by b), as shown in figure 4.6 (b). The explicit local structures of the twin boundary are shown in figure 5.12. According to figure 4.6 (a), it illustrates the nature of stacking sequence seen in the MD as $ABABA\underline{B}CBCB$ where $\underline{B}$ has local fcc environment (green atoms); the hcp (purple and red atoms) and fcc local structures also have some extended distortion. Thus the assumption of perfect structures is no longer held. This surely gives some deviation of the simulation results from the theory as we have seen in section 4.1.3 and 4.2.1.

Next we wish to understand the effect of the number of stacking faults on the strain components in the unprimed coordinates. By using equation (4.7), (4.9) and the rotation operations in appendix B, we numerically calculate the strain matrices which describe the hcp crystal plus some stacking faults in terms of a distorted bcc crystal in the unprimed coordinate system. We found, for example, that the yz shear component of hcp variant number 3 is linearly related to the

$$\begin{pmatrix} -0.87 & 0.00 & 0.00 \\ 0.00 & 0.30 & -3.93 \\ 0.00 & -3.93 & 4.10 \end{pmatrix} \qquad \begin{pmatrix} -1.96 & 0.00 & 0.00 \\ 0.00 & 0.99 & -3.00 \\ 0.00 & -3.00 & 3.51 \end{pmatrix}$$

(a) (b)

Table 4.7: Strain of a 2-striped twin composed of variants numbers 3 and 5 and including 2 stacking faults. a) Predicted by the elastic theory; b) resulting from the constant volume MD simulation followed by quenching the atomic configurations to 0K under the constant stress conditions. These results are in the unprimed coordinate system.

number of stacking faults contained in the hcp crystal. Note that it is convenient to work with the number of stacking faults, n per the size of the hcp crystal, l rather than the number of stacking faults itself because n/l can be compared with the MD results from different geometries. The results (solid line) of the yz shear component plotted against n/l are shown in figure 4.7.

The amount of shear that describes the hcp crystal plus some stacking faults in terms of a strained bcc crystal depends linearly on the number of stacking faults.

We have done MD simulations to confirm the results from the elastic theory. By simulating the martensitic transition at 600K and quenching the atomic positions to 0K under the constant stress conditions, the 'local structures' are determined. Then we can evaluate the ratio n/l and calculate $\underline{\varepsilon}$ from $\underline{B}$ using equation (4.4). The results of the yz shear component of hcp variant number 3 from 20 samples with different geometries (circles) plotted against the ratio n/l are shown in figure 4.7. Although the amount of strain predicted by the elastic theory is not exactly equal to the strain obtained by the MD calculations, it demonstrates the linear dependence of the yz shear component on the ratio

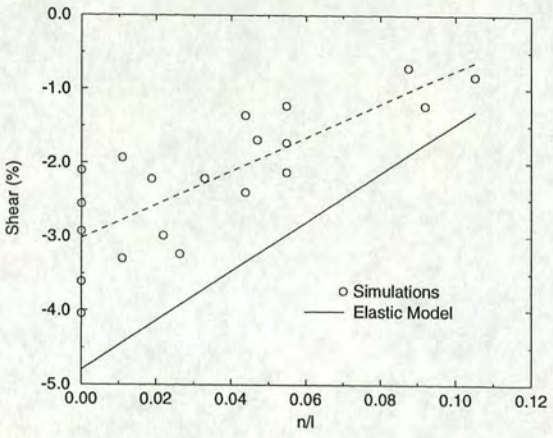

Figure 4.7: Plot of the shear in $[10\bar{1}\bar{2}](1\bar{2}10)$ against n/l taken from the constant volume MD simulations followed by quenching the atomic configurations to 0K under the constant stress conditions of different geometries samples ($30\times105\times25$ Å^3, $30\times105\times37$ Å^3, $30\times105\times50$ Å^3, $30\times123\times37$ Å^3, $41\times105\times25$ Å^3 and $51\times88\times50$ Å^3) (circles) compared with the elastic model (solid line). The dashed line is an eye guide.

n/l. This is useful for studying the twinning deformation in the martensitic microstructure as we shall see in section 6.3 that a particular variant can be forced to extinction by giving a suitable amount and suitable component of external strain.

4.2.3 Effect of Stacking Faults on the Twinning Angle

As we have seen in figure 4.2, stacking faults cause some rotation in the hcp crystal if stacking faults occur in every even close-packed plane. Now we wish to see further if they also affect the formation of the twin boundary. Referring to figure 4.8 (a), one stacking fault gives rise to atomic movement of $\frac{a_{hcp}\sqrt{3}}{2}$ Å in $[1\bar{1}00]_{hcp}$ at the $(10\bar{1}1)_{hcp}$ twin boundary. This movement cause a 'twin boundary step' of height $\frac{a_{hcp}\sqrt{3}}{2}\sin 61.5$ and also causes the rotation of the twin tilt angle to less than 61.5°, as in figure 4.8 (b).

Consider the plane perpendicular to $[1\bar{2}10]_{hcp}$ (the plane of the paper in figure 4.8), the shear is defined by

$$shear = \frac{n \times \frac{a_{hcp}\sqrt{3}}{2} \sin 61.5}{length\ of\ boundary}, \tag{4.18}$$

where n is the number of stacking faults. The length of twin boundary can be calculated in terms of the number of close-packed planes, m, as

$$l_y = \frac{m}{2}\sqrt{\left(\frac{\sqrt{3}a_{hcp}}{2}\right)^2 + c_{hcp}^2} \tag{4.19}$$

Note that this shear occurs when stacking faults exist only in even close-packed planes.

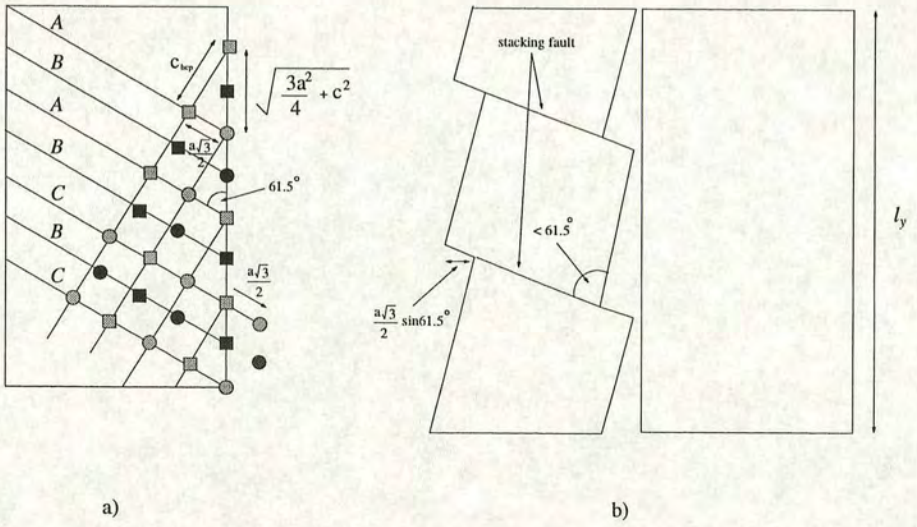

Figure 4.8: Crystal rotation caused by stacking faults; a) origin of stacking faults. Different symbols label atoms in different depth; b) rotational effect (not to scale).

The angle between the close-packed plane and the twin boundary is 61.5° but the angle imposed by the bcc structure is 60°. By inserting a suitable number of stacking faults into the twin crystal, we can reduce the 61.5° tilt angle to 60°. Thus the martensitic microstructure can accommodate the bcc-hcp transition

without much atomic diffusion. It has been found by the experiments that this twinning mode - in accord with the internal shears - is required to accommodate the bcc-hcp transition in Li, Ti and Zr [88].

Now we wish to rotate the twin crystal through 3.0° to obtain 60° twinning tilt angle. From equation (4.18) and (4.19), we get

$$\tan 3.0 = \frac{n\frac{a\sqrt{3}}{2}\sin 61.5}{\frac{m}{2}\sqrt{\frac{3a^2}{4}+c^2}}, \tag{4.20}$$

and

$$\left.\frac{n}{m}\right|_{T=0K} \approx 0.06(2). \tag{4.21}$$

In other words, a stacking fault must exist in every 16 close-packed planes in order to reduce the twin angle.

Stacking faults cause the rotation of twin tilt angle from 61.5° to 60.0° imposed by the bcc structure.

From the MD simulations of twinned structure, we found the average number of stacking faults contained in the twin crystal over 30 samples in different geometries to be equal to one stacking fault per 9.7 close-packed planes [25]. By motion of these stacking faults it would be possible for the crystal to deform plastically and the boundary to evolve to the stable $(10\bar{1}1)$ tilt without much diffusion of atoms from the parent bcc phase positions.

4.2.4 Microstructure Formation

We have seen in section 4.2.1 that the twinned microstructure can be described as an elastically deformed bcc, and now we will extend the theory further to explain the formation of the martensitic microstructure in terms of the elastic energy. Again the transformation can be described by a strain matrix as follows.

Firstly from a single bcc crystal, it can transform into a microstructure which composes of 1-2 hcp variants (see figure 4.9). The possible hcp variants are labelled by number 1, 2, 3, 4, 5 and 6 which correspond to the strain matrices in table 4.3.

Secondly, the strain matrix $\underline{\varepsilon}$ that describes the transformation can be derived from the average of strain components of all hcp variants appearing in the microstructure as in equation (4.15). This is a crude model because interface energy is neglected and the interfaces are oriented parallel to the yz plane only. According to this orientation, only the interface between variants numbers 3 and 5 is a $(10\bar{1}1)$ twin boundary - the interfaces of other combinations are not.

Thirdly, the strain energy can be calculated by using [89]

$$E_{strain} = \frac{1}{2}\sum_{ijkl} C^{T}_{ijkl}\varepsilon_{ij}\varepsilon_{kl}. \tag{4.22}$$

The strain energy in this equation has a unit of energy density per volume, i.e. J/m^3 or equivalent to GPa.

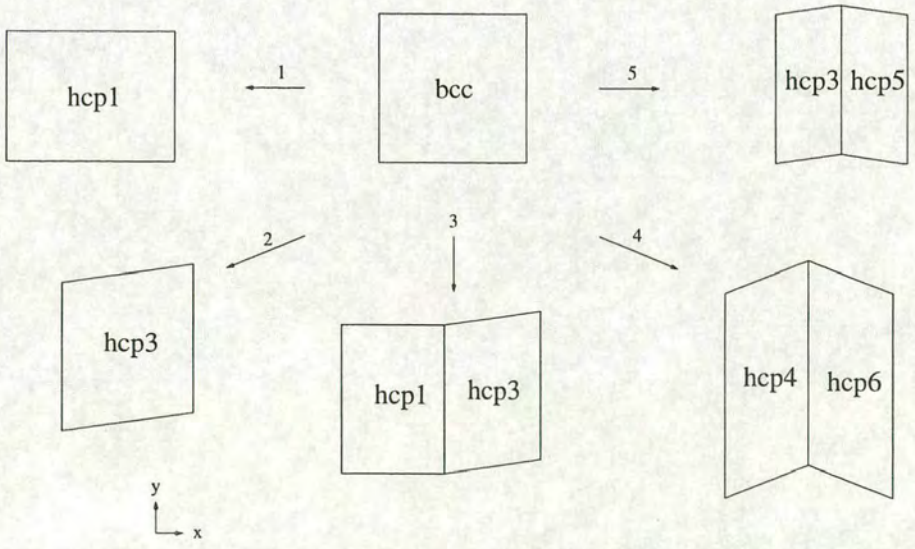

Figure 4.9: Illustrates the transformations from a single bcc crystal to the martensitic microstructures.

Sample	variant a	variant b	E_{strain} (GPa)
1	1	-	2.62×10^{-1}
2	3	-	2.33×10^{-1}
3	1	3	1.06×10^{-1}
4	4	6	8.86×10^{-2}
5	3	5	4.98×10^{-2}

Table 4.8: The strain energy of selected microstructures.

We estimate $C_{ijkl} \approx 50$ GPa. This is reasonable because C_{ijkl} in the bcc and hcp are also of the same order [7, 57]. The strain energy of selected microstructures are shown in table 4.8. It shows that the selected martensitic microstructures (samples numbers 3,4 and 5) have lower strain energies than a single structure (sample number 1 and 2). The corresponding microstructures are sketched in figure 4.9. This leads to a prediction that the microstructure tend to be formed during the martensitic transition. A combination of three or more variants may have even lower strain energy and become dominant in the microstructure.

The martensitic microstructure is more energetically favoured than a martensite crystal.

Although the results of this section suggest that the formation of microstructure is energetically favoured, it does not account for boundary energy and stacking fault energy. Furthermore, the theory does not give the detail about a typical size or the orientation of the hcp crystal. The typical size of the hcp crystal in the martensitic microstructure can be considered when we include the twin boundary energy as we shall see in the next section.

4.2.5 Energy Balance

Consider a typical microstructure. We know from the last section that the strain energy released from the phase transition is of order of 10^{-1} GPa. From energy balance, the total energy E_{total} of the typical microstructure is the sum of released strain energy E_{strain}, twin boundary energy E_{twin} and stacking fault energy E_{sf} as

$$E_{total} = -l^3 E_{strain} + l^2 E_{twin} + n l^2 E_{sf}, \tag{4.23}$$

where l is the typical size of the hcp crystal and n is typical number of stacking faults in a hcp crystal. Differentiate equation (4.23) with respect to l to find a minimum point at

$$l = \frac{2(E_{twin} + nE_{sf})}{3E_{strain}}. \tag{4.24}$$

In our case, $E_{twin} = 165 mJm^{-2}$ and $E_{sf} = 44 mJm^{-2}$. We choose $n = 2$. Thus $l \approx 17$ Å. However, the model in this section is only a crude model. In order to obtain an accurate result, we need to include correct geometry and correct strain energy as in the MD simulations. From an average over 50 MD simulations we found that the typical size of the hcp crystal in the martensitic microstructure is ≈ 32 Å.

4.3 Conclusions

The bcc-hcp transformation in zirconium can be regarded as an elastic distortion of the bcc crystal. We start from Nishiyama-Wessermann rules to explain a single crystal transformation. An elastic model has been proposed and the strain matrices for describing each hcp variant are constructed. It provides qualitative explanations for the features of the martensitic microstructure. The elastic model is modified to describe stacking faults. We found that the stacking faults exist even in a single crystal. This is because the strain field released from the bcc-hcp

transformation can be compensated by the existence of stacking faults. However, stacking faults themselves cause another strain field. Thus there is a balance, i.e. the density of stacking faults per close-packed plane must be 0.17 evaluated at 0K. This mechanism happens in a single crystallite and it is in good agreement with the results from the MD simulations. We extend the elastic model to describe the $(10\bar{1}1)_{hcp}$ twinning formation. The perfect twin angle is 61.5°. The effect of stacking faults in the twins is included. We found that the formation of $(10\bar{1}1)_{hcp}$ twins can significantly reduce the strain energy. The stacking faults also have an effect of rotating the hcp crystal through the twinning formation. This is to obtain an averaged 60° twin angle as it is forced by the bcc parent lattice, and the density of stacking faults per number of close-packed planes in this case is equal to 0.06. The elastic model is applied further for studying the formation of the martensitic microstructure. We found that the combinations of hcp variants have lower strain energy than a single martensite crystal and hence microstructure formation is energetically favoured. The typical size of the hcp crystal derived from the theory is 17 Å compared with 32Å obtained from the typical MD simulations.

Chapter 5

Martensitic Microstructural Evolution

Rivers flow into the sea,
Yet even the sea is not so full of me...
If I'm not blind, why can't I see,
That a circle can't fit where a square should be...

from *Hole Hearted* by Extreme.

In this chapter, we use molecular dynamics to simulate the time evolution of martensite microstructure. We are interested particularly on the growth behaviour and the natural evolution of the martensitic microstructure. The MD method is a powerful tool for this purpose because the typical speed of martensite growth is close to the speed of sound in metals [1] and it is difficult to probe by experiments. We have done the simulation by rapidly quenching the bcc supercell to the temperature below the transition temperature. The concept of 'local atomic structures' is introduced. The principle of this concept is to classify and label each atom in the simulation supercell according only to its local environment. The crystal structure is a region of atoms which have the same 'local structure'.

The picture of the martensitic structure can be constructed as a cross-section through the simulation supercell. The tools for determining the 'local structure' are developed in section 5.1. The transition temperature according to the potential is determined in section 5.2.1. The nucleation and growth kinetics of the martensitic phase are studied in section 5.2.2. We show that for simulations above a certain size, a twinned microstructure develops which has been suppressed by finite size effects in previous studies. This twinned microstructure is examined in section 5.2.3. After the system reaches a new equilibrium in the martensitic phase, there is a slight microstructure evolution which will be discussed in section 5.2.4. The conclusions are in section 5.3.

5.1 Microstructure Illustrations

The present work is concerned with the microstructural formation after the bcc-hcp martensitic transition. Thus it is necessary to verify correct crystal structures, such as bcc, hcp or fcc, which involve the formation of the martensitic microstructure. Consequently, the nucleation, growth kinetics and the evolution of microstructure will be examined by using an appropriate visualisation.

colour	structure	$\underline{\varepsilon}_a$
green	local fcc coordinations	-
red	local hcp1 coordinations	$\underline{\varepsilon}_5$
purple	local hcp2 coordinations	$\underline{\varepsilon}_3$
orange	local hcp3 coordinations	$\underline{\varepsilon}_1$
blue	'unknown' and 'plastic'	-

Table 5.1: The colour scheme used in microstructure illustrations. Some of these colours also correspond to the hcp variants defined in table 4.3.

Correctly identifying local crystal structure is the most important key in illustrating the microstructure. This is because the microstructure is a mosaic of several regions of different local structures. They can be identified by taking

coordinates of each atom and its nearest neighbours from the MD simulations and performing the quenching process or the thermal fluctuation removal procedures, then comparing with perfect structures, such as bcc, hcp or fcc, defined in section 5.1.2 and 5.1.3. The setting of perfect crystals is called a 'template'. The local structures can be matched to a template of perfect bcc, hcp or fcc by allowing a small rotation and a small deviation in atomic positions. If they cannot match the above structures, they will be labelled as 'unknown' structure. By this method, the exact orientations of these 'local structures' can be individually identified. Practically, we already know the orientation of the bcc and because of the bcc-hcp orientation relation, equation (1.3) and (1.4), we also know the possible orientations of 6 hcp variants and this knowledge considerably reduces the computational effort.

We picture the microstructure by introducing the concept of the 'local atomic structure'.

We have found that the microstructure forms a columnar structure; the microstructure repeats itself in a certain direction, normally in $[111]_{bcc}$ or its equivalent. Thus the pictures of the 3-D microstructure can be made from a cross-section of this columnar structure. Atomic positions are plotted in 2-D pictures and labelled by different colours according to different local crystal structures or different crystal orientations. Most pictures of the microstructure in the present work follow the colour scheme in table 5.1.

One disadvantage of this illustration is that the information of height from the plane is absent. It makes this visualisation method inappropriate for studying surface structures. Nevertheless the method is useful in our work where only the pattern of microstructures is studied. Examples of the microstructure illustration by this method have been shown in [25, 48] and throughout this work.

5.1.1 Neighbour Distribution Functions

Neighbour distribution functions can be represented by the distribution of neighbouring atoms with respect to the distance, the so-called radial distribution function (rdf), or the distribution of angles between neighbouring atoms, the so-called angular distribution function (adf). In case of the rdf, the distribution shows the probability of finding an atom at some distance, r, from another atom. In a regular lattice, the neighbour distribution does not vary in time and it has a certain characteristic of the crystal structure. Therefore, it is useful for quickly identifying the overall crystal structures in our work.

From the MD runs, the rdf is generated by calculating the distances r_{ij} for every pair of atoms in the system and plotting the number of atoms, which have neighbours in the range r_{ij} and $r_{ij} + \delta r$, against r, where δr is small. Thus the rdf, $\mathcal{D}(r)$, can be written as [54]

$$\mathcal{D}(r) = \lim_{\delta r \to 0} \sum_{ij} H(r_{ij} - r) H(r - r_{ij} + \delta r), \tag{5.1}$$

where $H(x)$ is the Heavyside function: $H(x) = 0$ for $x < 0$ and $H(x) = 1$ for $x > 0$. For a regular lattice, the rdf peaks appear at certain distances reflecting a characteristic of the crystal structure. The smallest distance, r_1, is the nearest neighbour distance. The peak located around this distance with the width of Δr_1 is called the first neighbouring shell. Subsequent peaks are called second and third neighbouring shells and so on. At 0K, $\Delta r_k \to 0$ but at high temperature, the thermal motion leads to bigger Δr_k. This thermal effect can combine two close rdf peaks into one broader peak which causes difficulties in the structure determination.

Wang and Ingalls [22] studied the bcc-hcp martensitic transition in iron induced by pressure ($\approx$ 13.0GPa). They used x-ray-absorption fine-structure (XAFS) technique to monitor the atomic structure and the phase transition.

The Fourier transform of the XAFS spectra closely relates to the radial distribution function of the absorbing atoms. We believe that the rdf is a good tool for determining the overall atomic structure and can be compared with experiments.

The adf can be generated very much in the same way. The angles θ_i between atomic bonds to the nearest neighbours are calculated. The plot between the number of angles which lie in the range θ_i and $\theta_i + \delta\theta$, against θ is established. The adf, $\mathcal{A}$, can be written as

$$\mathcal{A}(\theta) = \lim_{\delta\theta \to 0} \sum_i H(\theta_i - \theta) H(\theta - \theta_i + \delta\theta). \tag{5.2}$$

Similar to the rdf, the peaks in the adf have a characteristic shape for a corresponding structure. At 0K, the width of the adf peaks $\Delta\theta_k \to 0$ but at high temperature, the thermal fluctuation in atomic positions leads to broadening adf peaks and $\Delta\theta_k$ are bigger. Again this thermal effect can combine two close adf peaks into one broader peak which also causes difficulties in the structure determination.

Throughout this work, we always use both rdf and adf to determine the overall structure obtained from the MD simulations. To aid analysis, the effect of thermal motion can be removed from the atomic positions in a number of ways and they will be discussed in section 5.1.4 and 5.1.5.

5.1.2 Body-centered Cubic (bcc) Structure

At $T > 1{,}333$K, zirconium has the bcc structure. The primitive cell is rhombohedral with the cell angles of $\alpha = \beta = \gamma = 109.47°$. Nearest neighbour distance is $\sqrt{3}a_{bcc}/2$. The packing fraction is 0.68 [91]. The symmetry group is $Im3m$ (O_h^9). A cubic unit cell contains 2 atoms which are located, in units of a_{bcc}, at

$$p_1 = (0, 0, 0), \tag{5.3}$$

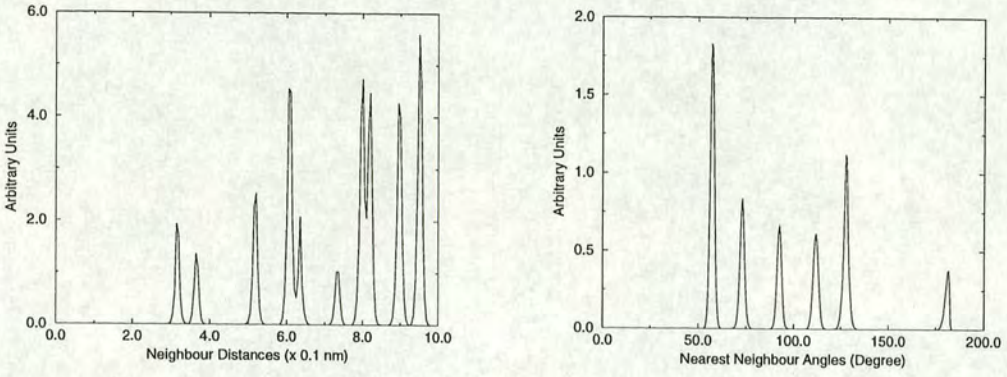

a) b)

Figure 5.1: Illustrates typical neighbouring distributions of a perfect bcc sample with 8,192 atoms; a) rdf; b) adf. The sample is a snapshot taken from the MD simulation after running at 600K for 10fs and the distribution peaks are slightly broadened by thermal fluctuation.

$$p_2 = (\frac{1}{2}, \frac{1}{2}, \frac{1}{2}). \tag{5.4}$$

According to the present potential at 0K, $a_{bcc} = 3.5886\mathring{A}$, $E_{coh}^{bcc} = 6.22eV$ and $V_{bcc} = 23.11\mathring{A}^3/atom$. The rdf and the adf of a sample that contains 8,192 bcc atoms are plotted in figure 5.1 (a) and (b) respectively. The rdf has principal peaks at $\sqrt{3}a_{bcc}/2$, a_{bcc} and $\sqrt{2}a_{bcc}$. These peaks mark neighbouring shells of the bcc structure. The rdf indicates that for a bcc atom there are 8 neighbours in the first shell and 6 and 12 neighbours in the second and third shells respectively. In the bcc case, the adf is the angular distribution of atomic bonds between the bcc atom and its first and second neighbouring shells. Some well-known angles, such as 60°, 90° and 109.47° are detected.

5.1.3 Close-packed (cp) Structures

At $T < 1{,}333$K, zirconium undergoes a first-order structural phase transition and has the hexagonal close-packed (hcp) structure. The theoretical packing fraction is 0.74 [91]. The symmetry group is $Pm6m$. A orthorhombic cell of the hcp comprises 4 atoms located at

$$p_1 = (0, 0, 0), \tag{5.5}$$

$$p_2 = (\frac{1}{2}, \frac{1}{2}, 0), \tag{5.6}$$

$$p_3 = (\frac{1}{3}, 0, \frac{1}{2}), \tag{5.7}$$

$$p_4 = (\frac{5}{6}, \frac{1}{2}, \frac{1}{2}). \tag{5.8}$$

The length of the sides of the unit cell are $\sqrt{3}a_{hcp}$, a_{hcp} and c_{hcp} in x, y and z directions respectively. According to the present potential at 0K, $a_{hcp} = 3.2488\mathring{A}$, $c/a = 1.595$, $E_{coh}^{hcp} = 6.25eV$ and $V_{hcp} = 23.68\mathring{A}^3/atom$. Note that the actual density of the hcp structure in our calculation is less than that of the bcc structure. This is in contrast with the theoretical packing fraction. The reason is that the packing fraction of hard spheres assumes equal nearest neighbour distances in both structures whereas the equilibrium nearest neighbour distances in the hcp structure are longer than the equilibrium nearest neighbour distances in the bcc structure.

The rdf and the adf of a sample that contains 6,912 hcp atoms are plotted in figure 5.2 (a) and (b) respectively. The rdf has principal peaks at a_{hcp}, $\sqrt{2}a_{hcp}$, $c_{hcp}$and $\sqrt{3}a_{hcp}$. The rdf indicates that for a hcp atom there are 12 neighbours in the first shell and 6, 2 and 12 neighbours in the second, third and fourth shells respectively. In the hcp case, the adf is the angular distribution of atomic bonds between the hcp atom and its first neighbouring shell only. Some well-known angles, such as 60° and 120° are detected. In addition, the hcp structure has a

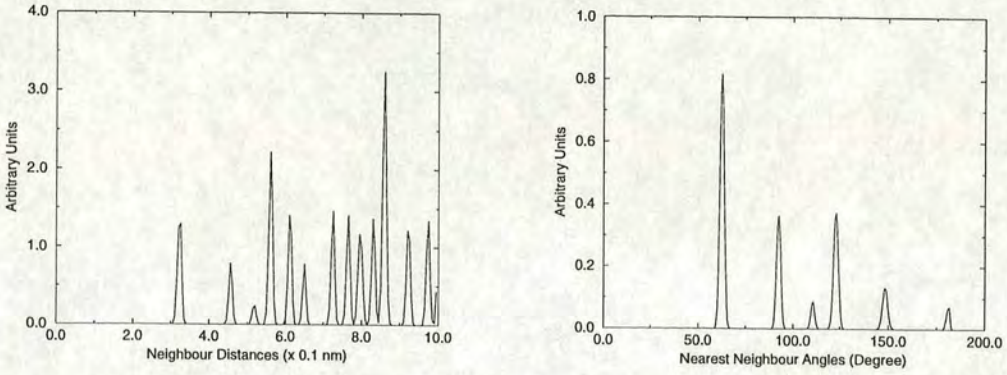

a) b)

Figure 5.2: Illustrates typical neighbouring distributions of a perfect hcp sample with 6,912 atoms; a) rdf; b) adf. The sample is a snapshot taken from the MD simulation after running at 600K for 10fs and the distribution peaks are slightly broadened by thermal fluctuation.

distinct peak in the adf about 140.5° angle. This angle comes from the atomic bonds to 2 nearest neighbours, which is $\sqrt{c_{hcp}^2 + a_{hcp}^2}$ apart. The 140.5° angle is absent in both bcc and fcc structures. Moreover, the adf peak around 140.5° gives a clear character of the hcp structure even at high temperature where $\Delta\theta_k$ is large. It is useful for quickly classifying the hcp and the cubic structures. Other peaks such as 60°, 90° and 120° are similar to the adf peak in the bcc and the fcc structures. Another hcp characteristic peak around 110° is less useful because it will be absorbed into the peak at 120° at high temperature where the adf peaks are broadened.

Stacking faults are a metastable state in most hcp metals including zirconium [92]. They have the local fcc environment but not a true fcc crystal. Stacking faults occurs as a fault in stacking sequence, i.e. $ABA\underline{B}CBCB$. The letter $\underline{B}$ denotes the line of atoms that have the fcc local coordination. In order to determine the fcc local structure we must learn more about the rdf and adf of the fcc

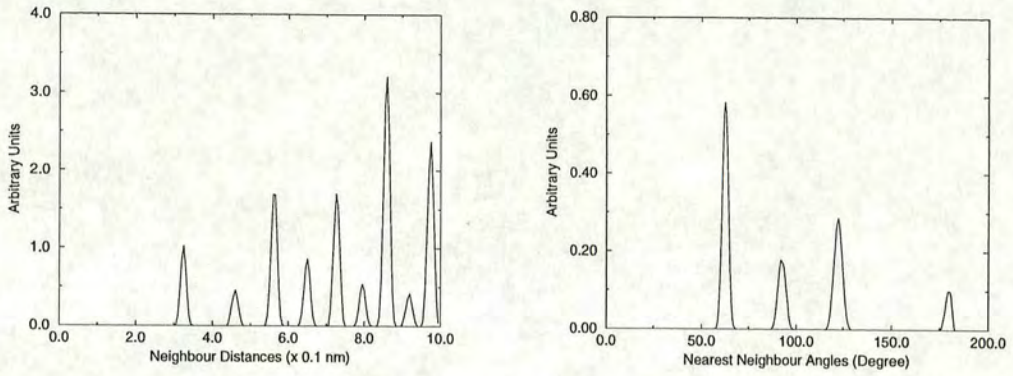

a) b)

Figure 5.3: Illustrates typical neighbouring distributions of a perfect fcc sample with 6,912 atoms; a) rdf; b) adf. The sample is a snapshot taken from the MD simulation after running at 600K for 10fs and the distribution peaks are slightly broadened by thermal fluctuation.

structure. A cubic unit cell of the fcc comprises 4 atoms located, in units of a_{fcc}, at

$$p_1 = (0, 0, 0), \tag{5.9}$$

$$p_2 = (\frac{1}{2}, \frac{1}{2}, 0), \tag{5.10}$$

$$p_3 = (0, \frac{1}{2}, \frac{1}{2}), \tag{5.11}$$

$$p_4 = (\frac{1}{2}, 0, \frac{1}{2}). \tag{5.12}$$

According to the present potential at 0K, $a_{fcc}/\sqrt{2} = 3.2488\mathring{A} \equiv a_{hcp}$, $E_{coh}^{fcc} = 6.23eV$ and $V_{fcc} = 24.25\mathring{A}^3/atom$. The rdf and the adf of a sample that contains 6,912 fcc atoms are plotted in figure 5.3 (a) and (b) respectively. The rdf has principal peaks at a_{hcp}, a_{fcc} and $\sqrt{3}a_{hcp}$. The rdf indicates that for a fcc atom there are 12 neighbours in the first shell and 6 and 12 neighbours in the second and third shells respectively. In the fcc case, the adf is the angular distribution

of atomic bonds among the fcc atom and its first neighbouring shell only. Some well-known angles, such as 60° and 120° are detected. Unlike the hcp, the peak around 140.5° is absent in the fcc structure.

The adf peak around 140.5° is unique in the hcp structure even at high temperature.

5.1.4 Quenching Atomic Configuration to Absolute Zero

In this work, we have done all the MD simulations at finite temperature, typically at $T \simeq 0.5T_0$ where the bcc-hcp phase transition occurs. The temperature is regulated by the Nosé-Hoover algorithm [60, 61, 62], see section 2.3.2 and 2.3.4. The Nosé-Hoover thermostat is required because it acts to remove the latent heat of the transition and without it, i.e in microcanonical ensemble, the transition would not occur because the latent heat will keep the temperature above the phase transition. To monitor the progression of the transition and the evolution of the microstructure, the concept of a 'local crystal structure' is introduced as we mentioned earlier in section 5.1. The martensitic microstructure is composed of several differently oriented regions of these local atomic structures, separated by domains boundaries. However at finite temperature the atomic positions fully include thermal fluctuation and hence it is impracticable to determine the local structures correctly.

One way to remove thermal motion is to quench the atomic configuration to 0K [54]. The hcp structure obtained from the typical MD simulation at 600K is shown as dashed lines in figure 5.4 (a) and (b). By quenching, the atomic configuration will fall into a local minimum of energy. Thermal fluctuations will vanish and the lattice will be close to the perfect structure. In practice the local energy minimum is located using a conjugate gradient method [93].

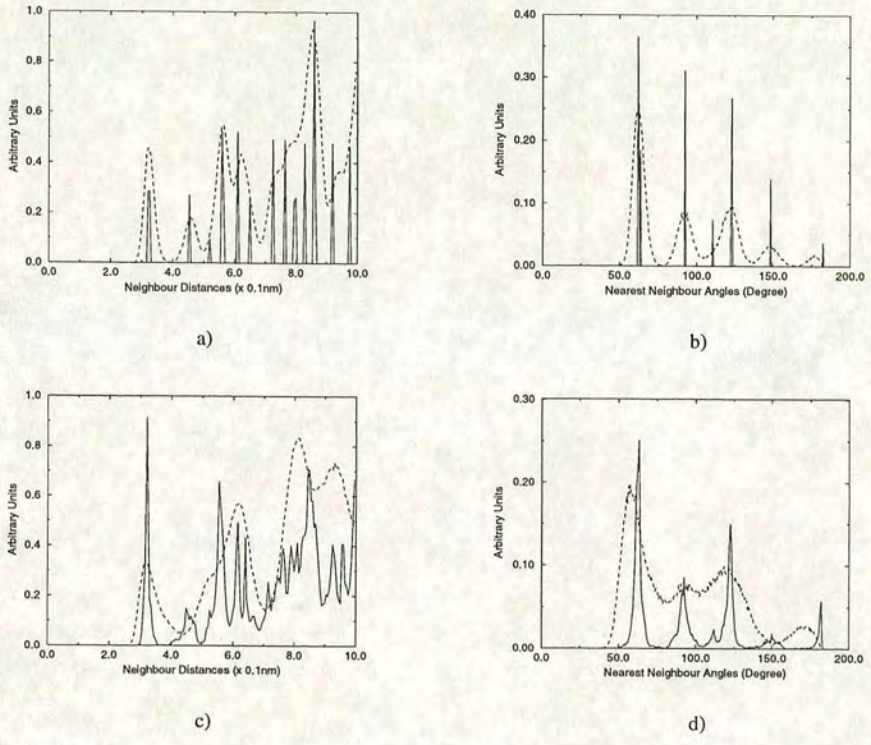

Figure 5.4: a) A typical rdf of 6,912 hcp atoms; b) a typical adf of the hcp. The dashed lines are the hcp structure taken from the MD at 600K after equilibration for 5ps. The solid lines are structure obtained by the quenching method. The dashed lines in (c) and (d) are the bcc structure taken from MD at 1,400K after equilibration for 5ps. The system contain 8,192 atoms. The solid lines are the structure obtained by quenching the bcc structure to 0K. It is obvious that the quenched structure has similar coordination to hcp in (a) and (b).

Together with the constant pressure scheme, the final configuration will represent an unstrained microstructure at 0K. The box mass, W, must be carefully chosen as it is important for the simulation box to gradually and steadily relax to its equilibrium shape. Ackland [54] found that $W = \sum_i m_i/10$ allows sufficiently steady progress for the particle relaxation. For the present potential, the hcp structures are stable at 0K. As shown in figure 5.4 (a) and (b), the hcp structure obtained by the quench method (solid line) is almost perfect; see figure 5.2 for comparison.

For our potential the hcp structure is stable at 0K, the stacking faults are a metastable state and the bcc is unstable.

However, as we have seen in section 3.2.3, the bcc structure is unstable at 0K. Thus if we use the quench method with the bcc + hcp phase, the bcc atoms will be eliminated from the microstructure. This is illustrated in figure 5.4 (c) and (d). The finite temperature bcc structure (dashed line) is taken from the MD and quenched to 0K. The structure achieved by quenching (solid line) has hcp local coordinations and hcp bond angles. The neighbouring distributions also show that the structure is not perfect but contains some distortion. Therefore in order to determine the bcc, we must resort to another method which will be described in the next section.

5.1.5 Thermal Fluctuation Removing Procedures

The problems of structure determination arise as far as the bcc is concerned because the bcc structure is not stable at 0K for the present potential. If one tries to quench an atomic configuration from a finite temperature simulation in which bcc and hcp co-exist to 0K, the microstructure will end up with hcp variants and their boundaries. To study such a co-existence, the structure determination must be done without quenching and hence thermal fluctuation in particle positions is fully included. Normally at a finite temperature particles move around their equilibrium lattice sites in random directions. Consequently, when we take instantaneous atomic positions, it might be impossible to identify the exact lattice sites. Nevertheless the effect of thermal fluctuation is to broaden the rdf and adf (dashed lines in figure 5.5 (a) and (b)). It does not alter the lattice structures unless a phase transition has occurred.

To remove the thermal fluctuation we invent an artificial spring network in order to sharpen the first rdf peak. The procedure is as follows. Firstly, take

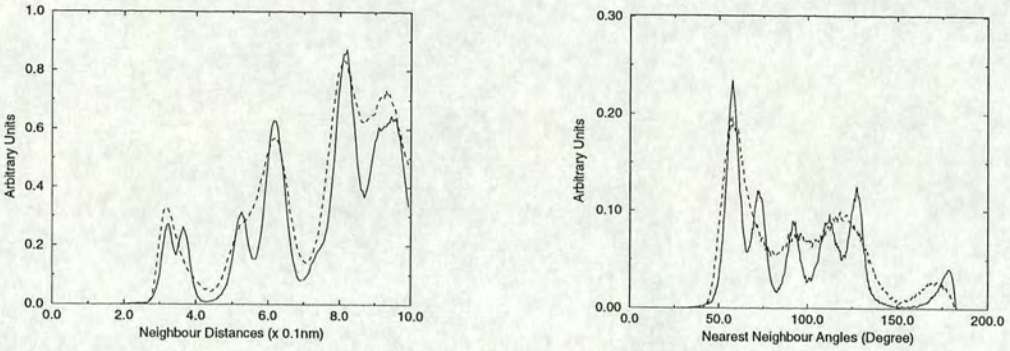

a) b)

Figure 5.5: a) A typical rdf of 8,192 bcc atoms at 1,400K (dashed line); b) a typical adf of the bcc at 1,400K (dashed line). Solid lines in (a) and (b) are the bcc structure after applying the thermal fluctuation removing procedure. See figure 5.1 for comparison.

only a single snapshot of the atomic positions from the MD simulation. Secondly, attach each atom and its nearest neighbours by springs with natural length equal to the average nearest neighbour distance. We choose 12 nearest neighbours in the hcp phase and 14 nearest neighbours in the bcc + hcp phase. Thirdly, move each atom until the force exerted on the atom vanishes, i.e.

$$\sum_{j}^{nn} F_{ij} = -\sum_{j}^{nn} k\Delta r_{ij} \to 0, \tag{5.13}$$

where Δr_{ij} is the difference between the instantaneous nearest neighbour distance and the natural length of the spring, j is summed over all nn nearest neighbours of atom i. Fourthly iterate the third step until the system reaches a local minimum in total energy state, i.e. minimise

$$\sum_{ij} E_{ij} = \sum_{ij} \frac{1}{2} k\Delta r_{ij}^2. \tag{5.14}$$

We found that the spring constant k affects the numerical solutions and the efficiency of the method. A preliminary test is needed for finding a suitable value of k; in this work, we use k in the range of 0.001 - 0.01.

The results of removal of thermal fluctuation of atoms in the bcc structure are shown as solid lines in figures 5.5 (a) and (b). The dashed lines in the figure show a typical bcc structure from the MD run at 1,400K. By comparing these results with figure 5.1, it is clearly seen that the overall structure is bcc. Note that the spring network improves the sharpness of not only the first rdf peak but of the entire rdf function and it also improves the sharpness of the adf peaks. These thermal fluctuation removing procedures will be adopted in section 5.2.2 when we study the martensitic nucleation process where the bcc and the hcp structures are co-existent.

5.2 Natural Evolution

Martensitic microstructure has been extensively studied in many materials over the past few decades [1]. These studies result in more understanding of mechanical properties of those materials. It is because the final microstructure, and as a consequence the mechanical properties are direct products of the different growth kinetics and nucleation. The growth kinetics and nucleation of martensitic transitions are most fundamental in the physics of first-order phase transitions [24, 33]. During the transition, the system will stay out of an equilibrium state, i.e. $< E >$ is not conserved. To obtain accurate results, one must perform a large scale simulation. This led Lindgård and Mouritsen [24] and Castán and Lindgård [33] to resort to a simple strain model. They studied the kinetics of martensitic domain growth and generalised to other classes of phase transitions. However, the study is rather limited because the correct number of variants and long range strain are absent from their physical pictures.

Here we employ the molecular dynamics approach in which atoms are treated

individually, and so the appropriate symmetries of the transition are automatically included. Furthermore, the full anharmonicity can be included via the interatomic potential, as is the relative stability of the various crystalline phases, their point, line and planar defects, and the anisotropic elasticity.

A large number of simulations have been performed, with varying crystallographic orientation and aspect ratio of the bcc lattice to the simulation supercell and investigating both constant volume and constant pressure boundary conditions, and different quenching methods. We have demonstrated in [25] that the observed qualitative microstructural features are independent of the details of the simulation (except for finite size effects). A number of common features emerge which we will discuss generally, and then illustrate these major features in the context of a few typical simulations.

5.2.1 Transition Temperature

The transition temperature, T_0, can be evaluated in a number of ways. The most convenient method is to plot the equilibrium values of the cohesive energy, E_{coh}, against temperature. We set the simulation in the constant stress scheme. The curve of the cohesive energy against temperature (figure 5.6) is evaluated for a number of samples with different geometries and different number of atoms, i.e. $29\times29\times29\mathring{A}^3$ (1,024 atoms), $102\times105\times25\mathring{A}^3$ (11,520 atoms) and $193\times193\times25\mathring{A}^3$ (40,128 atoms). The first is oriented in $x = [100]$, $y = [010]$ and $z = [001]$. The other two are oriented in $x = [1\bar{1}0]$, $y = [11\bar{2}]$ and $z = [111]$. We start the simulation with equilibrium bcc structure at high temperature and ensure that T $> T_0$. The temperature is gradually reduced by 1K and the system is allowed to be in an equilibrium for 50, 200, 300, 400 and 500 timesteps in which the cohesive energy is averaged. The typical curve with 300 timesteps for equilibration is shown in figure 5.6 (a). The cohesive energy of the bcc structure is approximately linearly dependent on temperature with positive slope. It also shows that around

1,350K the slope has dramatically changed indicating a structural activity. At T < 1,320K the cohesive energy has changed its character to non-linear behaviour. We determined the local structures at T < 1,320K and found that most atoms have hcp local coordinations. The rdf and the adf are similar to the dashed lines in figure 5.4 (a) and (b) respectively. In fact, the final microstructure is not a perfect hcp but rather some combination of hcp variants with some stacking faults as we shall see later in section 5.2.3 and 5.2.4.

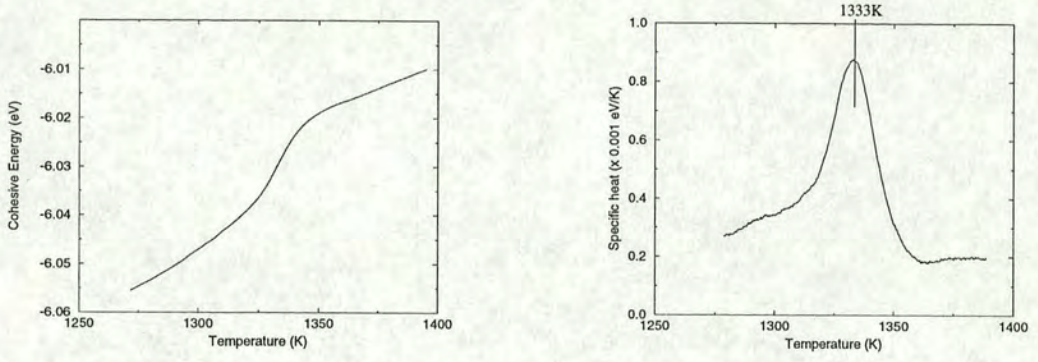

a) b)

Figure 5.6: a) The typical plot between the cohesive energy and temperature with 0.3ps equilibration period taken from the constant stress MD simulation with 40,128 atoms; b) the differentiation of (a) with respect to the temperature, i.e. specific heat. The mark indicates the optimum point which is defined as the transition temperature.

In order to determine the transition temperature, we differentiate the curve in figure 5.6 (a) with respect to temperature. This is the specific heat of the system. The result is shown in figure 5.6 (b). It exhibits a maximum at 1,333K. We define this as the transition temperature of the bcc-hcp transition. This behaviour is consistent with the other runs with different period of equilibration or with different number of atoms, except that shorter periods give lower T_0 as shown in table 5.2. The reason is that in the short period of equilibration the

equilibration period (*ps*)	T_0 (K)
0.05	1204 (11520), 1102 (40128)
0.20	1302 (40128)
0.30	1333 (40128)
0.40	1369 (1024), 1370 (11520), 1337(40128)
0.50	1333 (40128)

Table 5.2: Transition temperature calculations from the constant stress MD simulations with different geometries. The number of atoms is in parentheses.

ensemble average of E_{coh} can be only a poor representation of E_{coh}. Consequently, the curve of E_{coh} against temperature is incorrect.

The transition temperature of the bcc-hcp transition in zirconium in our calculations is 1,333K.

Osetsky and Serra [41] also used the MD calculations to determine the transition temperature for the bcc-fcc martensitic transition in iron. In their work only the changes in structure alone are considered in determining what is the transition temperature. However, the structure determination is sometimes ambiguous and hence gives an incorrect result. This led us to consider also the specific heat of the system together with the structural changes.

It is worth emphasising that the present potential is fitted to the physical properties of the hcp structure alone. There is no prior guarantee for the bcc-hcp transition or *vice versa*. However, we have shown in chapter 3 that the potential reproduces the phonon properties of zirconium in the bcc phase and exhibits the bcc-hcp phase transition upon lowering temperature. In addition, the transition temperature obtained from the present potential is reasonable compared with T_0 = 1,136K in real zirconium.

5.2.2 Nucleation Theory and Growth Kinetics

At the phase transition, the bcc structure gradually transforms into the hcp. The spatial positions where the transformations begin, the so-called nuclei, are randomly distributed in the bcc phase because their existence depends on local fluctuations. They may also shrink and vanish. Nucleation theory shows there is a critical size above which a nucleus will grow and below which it will only fluctuate [94]. However, after the nuclei emerge, they start growing in time as the phase transition continues. For simplicity, let us assume that the martensitic nucleus is of a cylindrical shape with thickness dz. In a real sample, this cylindrical symmetry can arise because there will be a temperature gradient and a boundary between the bcc lattice and the martensite. The nucleation seen here happens ahead of the boundary and the cylinders are perpendicular to it. If the boundary grows with velocity v, the number of martensitic atoms is proportional to the volume of the growing cylinder which is $\pi(vt)^2 dz$. The nucleus can be viewed as a circle in 2-D as shown in figure 5.7 (a). Additionally, if the nucleation sites appear constantly in time as ϵt, then the number of martensitic atoms will increase in time as

$$N_{marten}(t) = \frac{\epsilon \pi v^2 t^3 dz}{V_{hcp}}, \tag{5.15}$$

where V_{hcp} is the volume of a single hcp atom and ϵ is the nucleation rate. Hence the growth of number of martensitic atoms is proportional to the cube of time. This is illustrated in the curve in figure 5.8 (a). Eventually, several martensitic regions will reach each other and form martensitic boundaries as in figure 5.7 (b). The growth rate will then be impeded and the number of martensitic atoms no longer increases as a function of t^3 but rather more slowly as in figure 5.8 (b). When the transition is completed as in figure 5.7 (c), the growth rate becomes zero as shown in figure 5.8 (c). The typical size of crystal was determined in section 4.2.5.

In the early stage of nucleation where the martensitic nuclei grow independently, the growth behaviour can be described by equation (5.15).

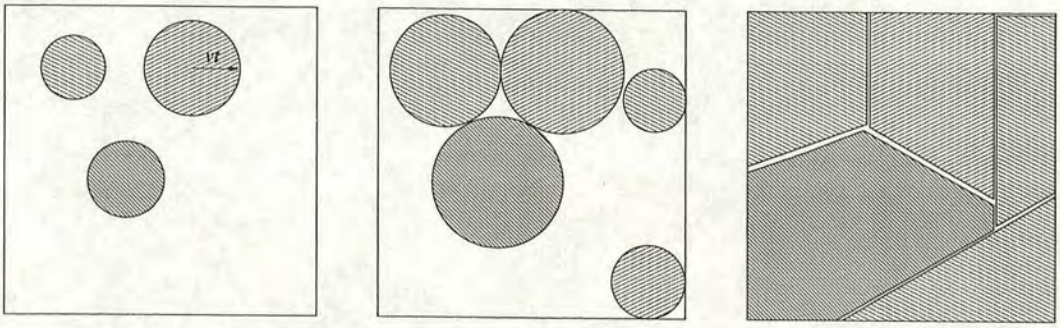

Figure 5.7: Shows schematic diagrams of nucleation and growth process; a) nucleation sites emerge and they are free to grow. The growth rate is proportional to t^3; b) domain boundaries are forming. The growth rate is impeded; c) at the final stage, the microstructure completes and the growth rate becomes constant.

Most of all, the curve in figure 5.8 describes growth behaviour similar to

$$N(t) = N_0(1 - \exp(-kt^n)), \tag{5.16}$$

especially where $t \approx 0$ and $t \to \infty$. This equation is empirical and generally valid for many types of phase transition, for instance precipitation transition, massive transition or cellular transition [94]. Notice that k and the power n are the main parameters in this equation. The exact values of these parameters can be derived by fitting to experimental data. Furthermore we expect that at t near the origin of the transition, equation (5.16) can be approximated by (5.15).

To verify the nucleation theory, we start a number of simulations from equilibrium bcc structure with 74,880 atoms ($264 \times 264 \times 25\mathring{A}^3$) oriented as $x = [1\bar{1}0]$, $y = [11\bar{2}]$ and $z = [111]$. The z direction is flattened because finite size effects force the martensitic phase to grow in the xy plane. The temperature is rapidly

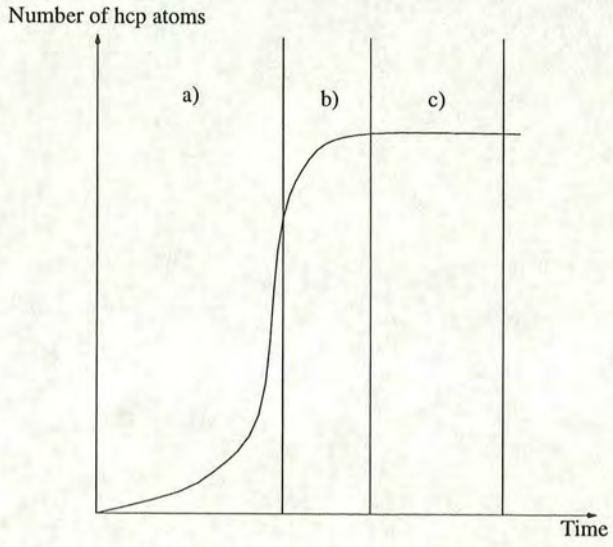

Figure 5.8: Illustrates the plot of the number of martensite atoms against time. (a), (b) and (c) are different growing stages corresponding to (a), (b) and (c) in figure 5.7.

reduced to 200K or 800K in the constant volume mode. The microstructure is determined at every period of 0.2ps. To study the time evolution of the phase transition, local atomic structures are identified using the method developed in section 5.1 and the number of atoms of each structure is counted and plotted against time. The growth behaviour of the hcp atoms at 200K (triangle) and 800K (circle) in the early stage is shown in figure 5.9 (a). It is readily seen that the number of hcp atoms increases faster at low simulation temperature. Generally the growth curve at this stage has a similar behaviour to the curve in figure 5.8. The simulation continues for 35ps, until the martensitic phase is in an equilibrium.

The entire evolution of the phase transition at 200K is shown in figure 5.9 (b). At a few ps from the beginning, the number of bcc atoms is dropping sharply. Most atoms of which local structure is the bcc structure become distorted, only few transform into the hcp. During the interval of 1-2ps the hcp phase grows sharply. Then variant boundaries are forming where different regions meet and

these boundaries decelerate the growth rate. The number of stacking faults starts increasing. Around 20 ps, the system approaches equilibrium. The number of the hcp atoms and the fcc atoms become constant. The bcc structure has virtually vanished. However, the plastic atoms keep increasing slightly and linearly in time while boundary structures are slightly decreasing. It is interpreted that the boundaries between hcp variants are removed and plastic movement is left as a by-product of the combining boundary. Further study will be done in section 5.2.4.

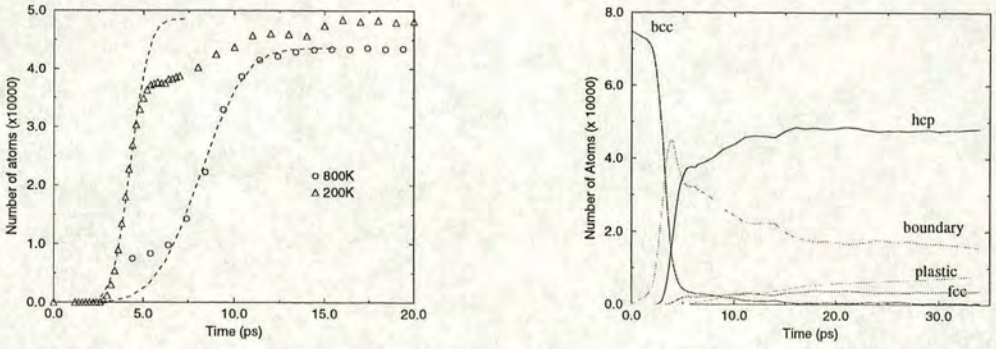

a) b)

Figure 5.9: Shows the time evolution of the phase transition from the bcc to the hcp structure; a) the plot of the number of the hcp atoms against time. The number of hcp atoms is identified from typical constant volume MD simulations at 200K (triangle) and 800K (circle). The system contains 74,880 atoms. Dashed lines are equation (5.16); b) the plot of the number of atoms of various 'local structures', which are involved in the bcc-hcp transition, against time at 200K.

The series of growing microstructure is illustrated in figure 5.10. The simulation setup is equivalent to fast cooling the real zirconium. At the beginning, the distorted bcc has propagated in some regions. During these few ps the hcp nuclei start forming. These nucleation sites are non-saturated, i.e. the sites can appear in random places in the sample. This is in contrast with the model derived by Lindgård and Mouritsen [24] which gave spontaneous nucleation. The distribu-

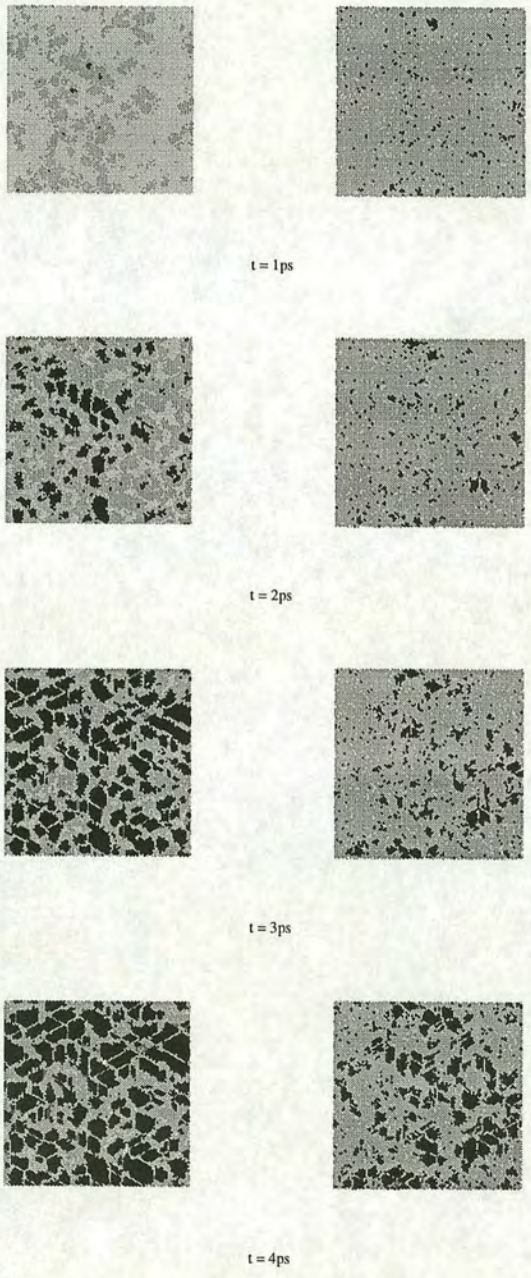

Figure 5.10: Four snapshots, taken at 1ps intervals from a typical constant volume MD simulation with 74,880 atoms at 200K (left) and 800K (right). The black regions indicate the hcp structure, regardless of orientation. The dark grey, mid-grey and light grey are domain boundaries, the bcc and the fcc respectively. 'Plastic' atoms are labelled by white.

tion of the nucleation is non-uniform. The growth of the hcp atoms at the early stage is fast and temperature dependent as shown in figure 5.9 (a).

The nucleation sites in our calculations are non-saturated.

There is an interesting point at the early period, $t \approx 3$ps, where the hcp regions are free to grow. Equation (5.16) can be estimated as

$$N(t) \approx N_0 k t^n. \tag{5.17}$$

From equation (5.15), it is trivial to choose $n = 3$ for equation (5.16). The parameter k can be evaluated by fitting the curve in figure 5.9 to the model in equation (5.17). We found that k is equal to $2.2 \times 10^{-2} ps^{-3}$ and $1.6 \times 10^{-3} ps^{-3}$ at 200K and 800K respectively. With the help of equation (5.15) and (5.17), we find that

$$\epsilon = \frac{N_0 k V_{hcp}}{\pi v^2 dz}. \tag{5.18}$$

This relation is valid only when the nucleation sites are growing independently. For simplicity we set $v \approx$ speed of sound in metals which is about 10 Å/ps. We estimate that $V_{hcp} \approx 24$ $Å^3$ and $dz \approx 25$ $Å$. The rate of nucleation can be calculated as 7.2×10^{-5} sites/Å^2/ps at 200K and 5.7×10^{-6} site/Å^2/ps at 800K. These results are rather oversimplified because we assume that growth velocity is constant, but figure 5.10 demonstrates that growth velocity is not uniform. Furthermore, the nucleation site is not a perfect circle but rather a rhombus. Nevertheless, it suggests that at 200K the martensitic phase nucleates faster and the crystal domains are finer whereas at 800K it nucleates more slowly and forms a coarsened microstructure. As a consequence the twinning structure becomes bigger and longer when the transition occurs at 800K.

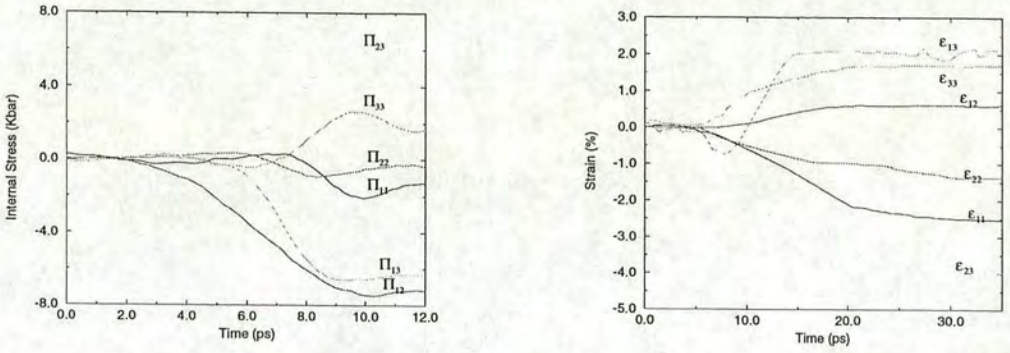

a) b)

Figure 5.11: a) A typical time evolution of the internal stress tensor components (equation (2.24)) taken from a constant volume MD at 800K. b) A typical time evolution of the strain components calculated from the box matrix by equation (2.28). The box matrix is taken from a constant pressure MD at 800K.

The more rapid the cooling, the finer the microstructure.

Another way to monitor the evolution of the phase transition is to compute the time evolution of the internal stress tensor in the constant volume MD or the strain matrix in the constant pressure MD. This is because, as discussed in chapter 4, the formation of the microstructure can compensate for the shape change during the transition and strain energy will be minimised. Nevertheless, the number of variants and their typical size have some limits, i.e. there are only 6 variants and the typical size is about 32 Å; see section 4.2.5. Therefore the shape change by the phase transition is not totally compensated. This results in small residual stresses in constant volume simulations. A typical result of the phase transition in constant volume simulations is shown in figure 5.11 (a). The curves show the typical time evolution of the components of the internal stress tensor, defined by equation (2.24). The simulation was done at 800K, initialised

by an equilibrium bcc structure. They demonstrate that the system has been in equilibrium for a few ps before undergoing the phase transition. A period of about 9ps is required for the system to reach a new equilibrium state in the martensitic phase. This agrees with the time evolution of the number of hcp atoms at 800K (figure 5.9 (a)) which also shows that the system has evolved for 9ps before the number of hcp atoms reaches its maximum and becomes constant in time. This exhibits the first-order nature of the transition.

Figure 5.10 demonstrates the short range order nature of the bcc-hcp transition whereas figure 5.11 demonstrates the long range order behaviour. It clearly shows that the long range effect is significant a few ps after the local changes.

A typical constant stress simulation with the same setup is shown in figure 5.11 (b). It shows the time evolution of the strain components computed by equation (2.28). The strain matrix has similar behaviour to the internal stress tensor during the phase transition.

5.2.3 Twin Boundary and Twin Boundary Steps

After 10 ps, the sample is completely transformed. The final microstructure appears to have long stripes of rhombus shape and has no periodic pattern. The interfaces are categorised into two groups. The first group has coincident site (see also section 6.4), low energy $(10\bar{1}1)$ twin boundaries. The 'local structure' of atoms in the twin boundary is demonstrated in figure 5.12 (a) and (b). The boundary is in fact an array of these two irregular structures which has 13 nearest neighbours of type (a) and 11 nearest neighbours of type (b). The arrangement of the boundary structure is $...aa'b'baa'b'ba..$ where primed symbols indicate different layers. The c_{hcp} axis is largely distorted. An example of the $(10\bar{1}1)$ twin

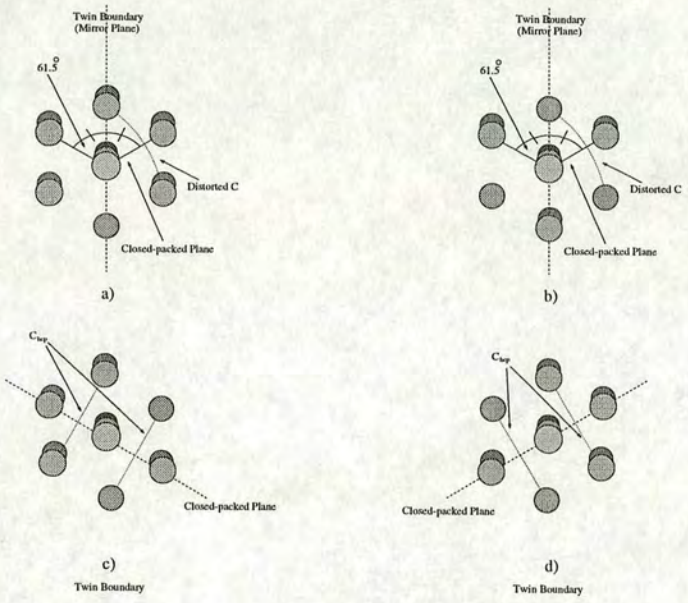

Figure 5.12: Illustrates; a) local structure of $(10\bar{1}1)$ twin boundary. It has 13 nearest neighbours and the c_{hcp} axis is distorted; b) another local structure of the boundary which has 11 nearest neighbours; (c) one possible orientation of the local hcp structure existed in the simulation; (d) another possible orientation of the local hcp structure. These two local hcp structures form twin boundary on the twinning plane (dotted line).

boundary and its inner structure were shown in figure 4.6. The angle between the close-packed planes and the twin boundary is 61.5°. This is one of a few possible twin structures that are known to exist in zirconium [38]. The twin boundary is the interface of two appropriate variants, illustrated in figure 5.12 (c) and (d).

However, in the coordinate system of the simulation supercell there are only a few possible orientations of the $(10\bar{1}1)$ twin boundaries which are imposed by the parent bcc crystal. These orientations of the boundaries are

1. parallel to the dotted line in figure 5.12,

2. at 61.5° angle to the dotted line in figure 5.12,

3. at 123.0° angle to the dotted line in figure 5.12.

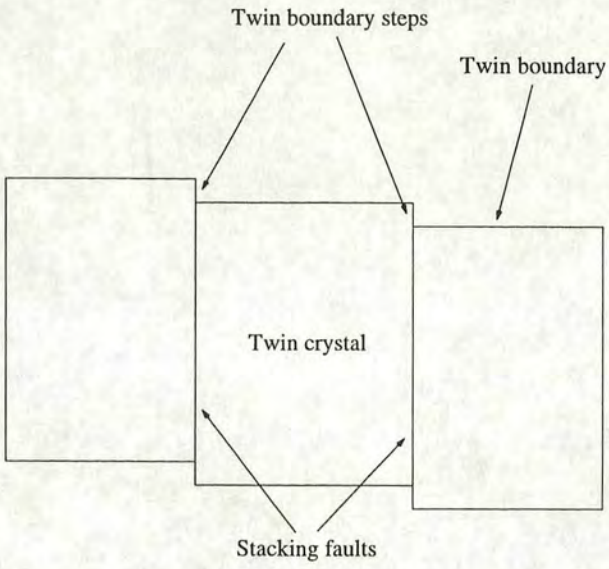

Figure 5.13: Illustrates two 'twin boundary steps'.

Apart from the orientations above, the interface between different hcp variants will be a broad boundary which falls into the second category. In this category, the atomic local structure is irregular and cannot be classified as hcp, fcc or bcc.

Now we wish to demonstrate the effect of stacking faults on the twin boundary. In a hcp crystal, a partial stacking fault can be created by a dislocation moving across the basal plane with Burgers vector not equal to a lattice translation vector. This stacking fault is bounded by a 'partial dislocation' [95], see figure 5.13 (b). In contrast, stacking faults occurred in our simulations are embedded by the twin boundaries. These stacking faults also create twin boundary steps of height $\frac{a_{hcp}\sqrt{3}}{2}\sin 61.5$ on the twin boundary as shown in figure 5.13 (a). These steps will be regarded as the 'twin boundary steps' from now on. The boundary structure of these 'twin boundary steps' are quite similar to the twinning dislocations studied by Serra, *et al.* [88] but there are no stacking faults present in the latter. The twinning deformation yields by twinning dislocations as follows. Firstly, by applying a suitable shear the twinning dislocations are induced to move along

the twin boundary in the direction of η_1; defined in section 4.2. Secondly the twin crystal will grow at the expense of the other. This mechanism is important to recognise because we will see in section 6.3.1 that the twining deformation causing by the 'twin boundary steps' also has a similar mechanism.

We believe that the existence of stacking faults is partly because the system tries to reduce atomic movement from the bcc to the hcp and stacking faults can relieve some strain energy as shown in section 4.1.4 and 4.2.3. The existence of stacking faults also help to indicate the orientations of hcp variants.

The presence of stacking faults is reported in experiments of twinning by deformation by Song and Gray [30]. Using empirical many-body potential for most of the hcp metals, Vitek and Igarashi [92] found that I_2 stacking faults are a common metastable state of those hcp metals. We believe that stacking faults may exist in real martensite.

The typical microstructure in our calculations is the $(10\bar{1}1)$ twinned microstructure with some stacking faults in each twin crystal. These stacking faults create some 'twin boundary steps'.

5.2.4 Microstructure Evolution

As we have mentioned earlier, the observed microstructures are independent of the details of the simulations [25]. Therefore it is convenient to study the detail at the atomic level of the microstructural evolution by considering a smaller simulation scale. In this section, we will illustrate the entire process by following a single typical simulation.

The orientation of the bcc lattice with respect to the simulation cell is $x = [1\bar{1}0]_{bcc}$, $y = [11\bar{2}]_{bcc}$ and $z = [111]_{bcc}$. The dimensions of the cell are set to x = 102Å, y = 105Å and z = 25Å. To simulate the initial bcc phase and the

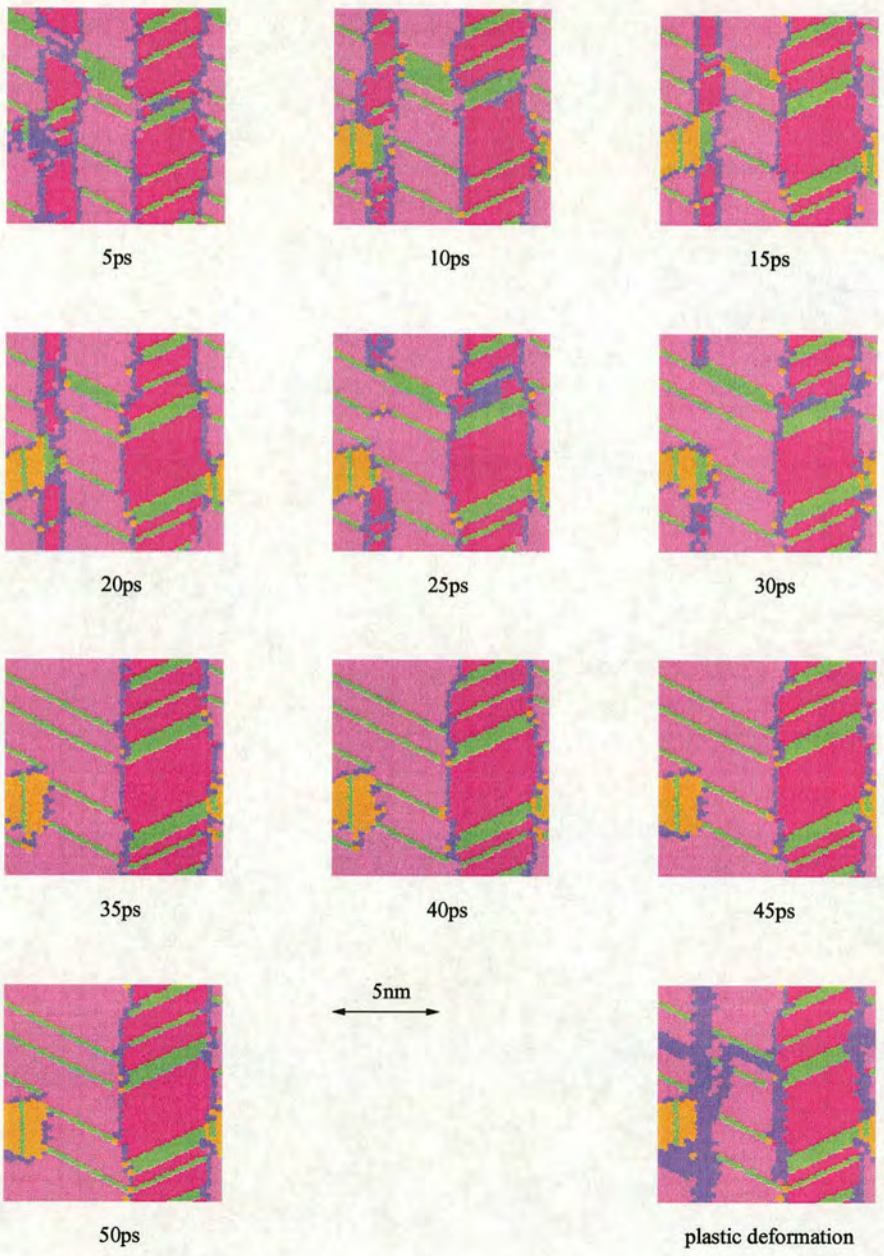

Figure 5.14: Ten snapshots, taken at 5ps intervals, of configurations quenched from the constant volume MD simulations with 11,520 atoms. The purple, orange and red regions are hcp-coordinated variants, the green regions are fcc (generally these are stacking faults) while the blue are unclassifiable atoms (typically in the atomically sharp twin boundary). The final picture is from the same configuration as the tenth (50ps), with atoms having different neighbours from their original bcc-coordination shell coloured blue.

final hcp phase in the same simulation, we use periodic boundary conditions. After equilibration, the temperature is reduced to 600K and the evolution of the microstructure followed.

In our chosen simulation, $< 1\bar{2}10 >_{hcp}$ lies along the z-axis of our simulation cell. The microstructure repeats itself in this direction due to the finite size effect. This means that we can represent the microstructure by considering a single xy-plane slice, as in figure 5.14. The other such planes are similar.

Within the first 5ps (figure 5.14) the phase transition almost completes. Four strips of laminated 60^o twins are developed. These twins correspond to two of the possible hcp variants, illustrated individually in figure 5.12 (b) and (c). The twin boundary is close to the $(10\bar{1}1)_{hcp}$ plane. Referring to experimental and other computational results, $(10\bar{1}1)_{hcp}$ twins grow only in highly stressed sample at high temperature [38, 43]. Furthermore, it has been shown experimentally that $(10\bar{1}1)_{hcp}$ twin associated with the internal shears can accommodate the bcc-hcp transition in lithium, titanium and zirconium [88]. Here, the 60^0 angle is forced by the relationship to the parent bcc phase. At this stage, some metastable structures including a number of stacking faults (which manifest themselves as diagonal lines of fcc-coordinated atoms) are produced, and a small region of rather random close packing is nucleated.

By 10ps, the random close-packed region has ordered into a small lump of the third hcp variant. During the period to 30ps, the thinner of the strips of one hcp variant is gradually replaced by the other variant. This coarsening of the microstructure is analogous to Ostwald ripening, in which two twin boundaries are removed. The atoms in this region have now moved away from their previous sites in plastic deformation, and they have a different set of nearest neighbours. The boundary movements are complicated and inevitably leave plastic movement as a by-product. We will discuss the twinning mechanism in more detail in section 6.3.1.

Removing a twin boundary occurs naturally by a ripening process and some 'plastic atoms' result during the process.

After 40ps, only three regions of three distinct variants are left. Two variants clearly dominate, forming the familiar martensitic laminate microstructure. The third variant is forced to merge with the dominant variant in an inappropriate direction and to create a broad domain boundary. This broad boundary is not moving within our simulation time scale.

The final two figures show a small amount of further evolution as the twin boundaries straighten and sharpen. The final picture is at 50ps, the same as the previous, except that those atoms which have nearest neighbours other than the original 14 from the bcc structure are marked in blue. This gives some indication of the amount of plastic deformation which has occurred, and hence of sources of microscopic irreversibility in the transition. Of course, the thickness of the laminate is now determined by the finite size of the simulation cell.

Although the chosen simulation shows most of the behaviour observed in the other 50 simulations on similar cells - varying crystallographic orientation of the bcc lattice and varying aspect ratio, it is important to recognise that the nucleation is to some extent random. In some simulations, $< 1\bar{2}10 >_{hcp}$ did not lie along the z-axis. In others only two stripes of two variants were nucleated, and hence no coarsening was observed. The third variant did not appear in many of the simulations. Again, this variety of behaviour gives us confidence that the nucleation phase is not dominated by finite size or boundary condition effects.

5.3 Conclusions

In this chapter we study the bcc-hcp transition in zirconium by using atomistic simulations and the MD method. The overall atomic structures are determined by using the radial distribution function and the angular distribution function.

An individual local structure is identified by taking a snapshot of the atomic configuration from the MD runs, reducing thermal motion by either the quenching method or the procedures to remove thermal fluctuation, then taking an individual atom and its nearest neighbours and comparing them with a template of perfect structures, such as bcc, hcp or fcc. After examining all atoms in the system, the cross-section of the microstructure can be pictured. This allows us to study the evolution and the microstructure of the bcc-hcp transition at the atomistic level.

Firstly, we calculated T_0 by plotting the E_{coh} against temperature. We found that T_0 in this model potential is 1,333K. Secondly, we study the time evolution of the transition. A nucleation model is proposed. Typical behaviour of growth kinetics is discussed as follows: the number of martensitic atoms grow as t^3 in the early stage. The growth rate is impeded when boundaries are formed. It becomes constant when the phase transition completes. This is in good agreement with the typical MD simulations at 200K and 800K. The growth kinetics in the first 10ps is similar to that of the nucleation model. We also found that more rapid quench simulation produces a coarse microstructure.

The microstructure obtained from the MD is dominated by stripes of the $(10\bar{1}1)_{hcp}$ twins. Some mismatched boundaries between the hcp variants are detected. The structure of $(10\bar{1}1)_{hcp}$ twin boundary is examined. We found that the twin boundary is an array of irregular structures in a $(10\bar{1}1)$ plane. Stacking faults in the twin crystal cause steps of height $\frac{a_{hcp}\sqrt{3}}{2}\sin 61.5$ on the twin boundary. We have called these steps the 'twin boundary steps'. They play an important role in twinning deformation as we shall see in section 6.3.

At the final stage of the phase transition where the growth rate of martensitic atoms become finite and constant, there is a slight evolution in the final microstructure. Because of scale independence of the method [25], we study the typical evolution of the microstructure in the context of a smaller simulation. We found that stripes of the $(10\bar{1}1)_{hcp}$ twins become coarsened and leave plastic

damage to the microstructure. The plastic atoms occur because the coordination numbers between boundary structures and the hcp are different, and then some atoms must be shuffled in order to obtain a regular hcp structure while the boundary is swept through.

Chapter 6

Twinning Deformation

"If you are under strain,
knock your head on the door.
If some remains, knock it again
'til there'll be no more."

I wrote, 2nd August 1999.

Identification of deformation mechanisms leads to understanding in ductility and plasticity of materials. There is an excellent review on the ductility and plasticity of hcp metals and their alloys by Yoo and Lee [96] and a particular review on titanium and its alloys by Naka, *et al.* [97]. In this chapter, we are interested particularly in the ductility and plasticity of zirconium. Zirconium is a ductile metal [35]. However, there are only two main slip modes, i.e. primary slip in $\frac{1}{3} < 1\bar{2}10 > \{1\bar{1}00\}_{hcp}$ [26, 36, 35] and secondary slip in $\frac{1}{3} < \bar{1}\bar{1}23 > \{10\bar{1}1\}_{hcp}$ [35]. Hence, these slip modes are insufficient to satisfy *von Mises' criterion* [95] - it requires five independent slip systems for every grain to deform plastically to accommodate the macroscopic shape changes imposed by neighbouring grains. As a consequence, twinning deformation plays an associated role in the plasticity in zirconium [4, 37].

We will concentrate on twinning deformation in zirconium microstructure. There are two ways to obtain twinning. The first one is twinning via the bcc-hcp phase transition which we have discussed in section 5.2.3 and 5.2.4. The second one is twinning via shape deformation which will be investigated throughout this chapter. We are interested particularly in the $(10\bar{1}1)_{hcp}$ twinned microstructure as it naturally occurs via the phase transition in our simulations. We focus on two similar structures of the twins. The first structure is called a 'perfect twin'. It is a structure composed of two mirror image hcp variants forming a boundary on the mirror plane, $(10\bar{1}1)_{hcp}$ in this case. This boundary is straight and is called symmetric tilt twin boundary. The sample is prepared artificially as hcp twins. The second is a twinned structure which has been produced from the bcc phase via the phase transition. It is not a pure single crystal, but contains several hcp variants, $(10\bar{1}1)$ twin boundaries and some stacking faults. The simulation methods will be explained in section 6.1. We study elastic deformation in section 6.2. The twinning deformation and its mechanism are investigated in section 6.3. The conclusions are laid out in section 6.4.

6.1 Deformation Simulations

There are two fundamental methods to perform deformation simulations. The first method is to apply direct stress to the simulation by exerting a constant force on every atom on a certain surface in a specific direction. An opposite force must also be exerted on the opposite surface so that the system experiences no net force. The stress is equal to the amount of the force divided by the simulation area of that surface. At equilibrium, the microstructure is examined and the strain induced by the applied stress is measured. This method is convenient and straightforward. However, if the microstructure can undergo a series of structural changes at a particular amount of stress, the system will take a long time, often longer than the practical time scale in our simulation ($\approx$ 50ps), to reach an

equilibrium - this is the yield point of the material - and it is impracticable for the present purpose.

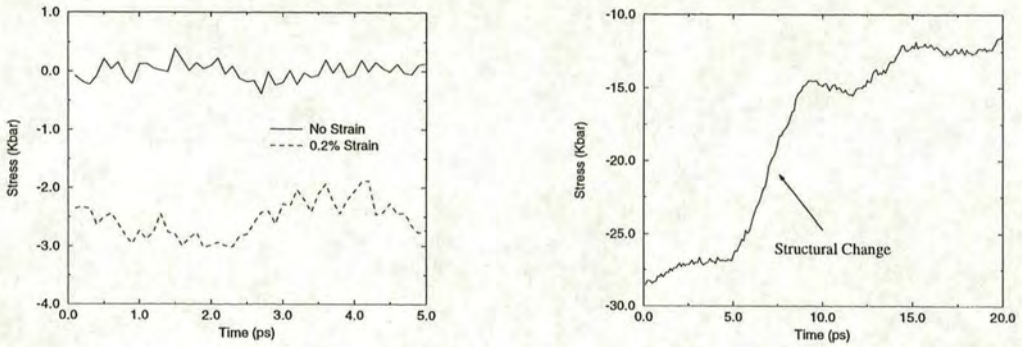

a) b)

Figure 6.1: The typical evolution of stress from the constant strain method. The simulation contains 11,520 atoms. a) Solid line is the stress at no strain. Dashed line is the stress corresponding to 0.2% strain; b) large strain causes a large amount of stress which induces a structural change.

The other method is strain simulation. In this method, deformation is performed by slightly deforming the simulation box, typically 0.2%-0.4%, then running the simulation until it reaches an equilibrium. Microstructure is then examined. If the strain is in some simple orientation, the induced stress can be measured from an ensemble average of the components of the internal stress-tensor. An example of strain simulation is shown in figure 6.1 (a). Normally, the simulation with no strain has zero stress (solid line). Stress is increased to $\approx$ 2.5 kbar when the sample is 0.2% deformed (dashed line). The increasing strain is applied repeatedly until the sample cannot withstand the increased stress and undergoes a structural change. An example of structural change is shown in figure 6.1 (b).

By the strain method, the stress-strain relation can be established and together with the illustration method (see section 5.1), a series of pictures of mi-

crostructural evolution can be constructed. It makes it possible to examine the stress-strain relation along with corresponding changes in the microstructure and the deformation mechanism can be studied at the atomic level.

Stress method	- apply stress to each atom - measure strain on the Parrinello-Rahman block - use constant stress MD
Strain method	- apply strain to each atom - measure stress on the block - use constant volume MD

6.2 Elastic Deformation

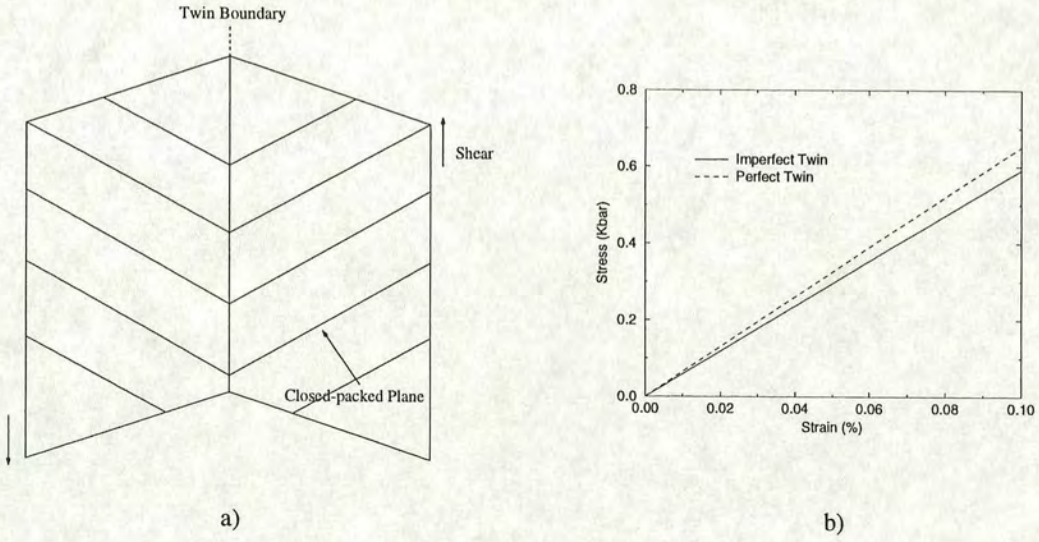

Figure 6.2: Illustrates the simulation setup; a) a $(10\bar{1}1)$ twinned microstructure is being sheared on $[10\bar{1}\bar{2}](10\bar{1}1)$; b) stress-strain relation in the elastic limit of perfect twins (10,240 atoms) (dashed line) and martensitic microstructure (11,520 atoms) (solid line) at 600K using the strain method.

In this section, we are interested in elastic deformation where the microstructure can recover the previous shape after the small applied stress is removed. The

simulations have been carried out at 600K. Both perfect twins and martensitic microstructure are studied. The perfect twinned microstructure has the dimensions of $99 \times 94 \times 26\mathring{A}^3$ (10,240 atoms). The simulation supercell is carefully taken to be orthogonal and $z = [1\bar{2}10]_{hcp}$. The martensitic microstructure has the dimensions of $102 \times 105 \times 25\mathring{A}^3$ (11,520 atoms) and was created by a phase transformation from a regular bcc structure which is oriented in $x = [1\bar{1}0]_{bcc}$, $y = [11\bar{2}]_{bcc}$ and $z = [111]_{bcc}$. After the bcc-hcp transition the martensitic microstructure orients in $z \approx [1\bar{2}10]_{hcp}$. In fact the perfect twins are set up with the same orientation as in the microstructure. Note that the martensitic microstructure is the twinned microstructure which contains a number of stacking faults. The different twin setups are presented in table 6.1.

Perfect twins	- artificially prepared - free from defects and dislocations - straight boundary - orthogonal supercell and $z = [1\bar{2}10]_{hcp}$ - $99 \times 94 \times 26\mathring{A}^3$ (10,240 atoms)
Martensitic twins	- produced from the bcc-hcp transition - contains some stacking faults - contain 'twin boundary steps' - zigzag boundary but straight on the average - $[111]_{bcc} \approx [1\bar{2}10]_{hcp}$ - $102 \times 105 \times 25\mathring{A}^3$ (11,520 atoms)

Table 6.1: The difference between perfect twin and martensitic twin supercells.

A small strain of 0.02% is applied to the samples in the $[10\overline{12}]$ direction on the $(10\bar{1}1)$ plane as demonstrated in figure 6.2 (a). After the system reaches equilibrium, the stress is measured from the internal stress-tensor. Then the strain is relieved from the sample and the atomic configuration is relaxed and examined, as discussed in section 5.1, to verify that there is no plastic deformation occurring. By continuing evaluation of responding stress at every increasing strain, we can plot the relation in the elastic region between stress and strain

of the perfect twin and the martensite microstructure. The results are shown in figure 6.2 (b). The shear modulus, G, can be calculated from the graph. We found that $G = 66$ GPa for the perfect twin and $G = 58$ GPa for the martensite microstructure. It shows that both microstructures have similar flexibility.

6.3 Twinning Deformation

Twinning deformation is common in twinned microstructures. It occurs while the microstructure is stressed by a certain amount. Atoms in small regions displace almost instantaneously and cooperatively so that those variants which reduce the stress become dominant in the microstructure. Again in this section, we will examine the twinning deformation both in perfect twins and in martensitic microstructure.

6.3.1 Martensitic Microstructure

Starting from equilibrium bcc at 1,400K, we rapidly quench the simulations to various temperatures, i.e. 600K, 800K, 1,000K and also 1,200K where the bcc-hcp transition takes place. The dimensions of the samples are $102 \times 105 \times 25 \mathring{A}^3$ (11,520 atoms). After the samples reach an equilibrium state in the martensitic phase, the final microstructures have z aligned along $[1\bar{2}10]$. A number of simulations have been studied and we found typical microstructure is composed of 2 stripes (at 600K and 800K) or 4 stripes (at 1,000K and 1,200K) of $(10\bar{1}1)$ twin structures parallel to yz plane. A typical sample of 4 stripes is shown in figure 6.4 (a). Notice that the number of stripes varies with the simulation temperature. This is consistent with the nucleation theory in section 5.2.2.

At equilibrium, we perform strain simulation at 0.2% per 20ps in $[10\overline{12}](10\bar{1}1)$. Each 20ps period, we measure the corresponding stress. The atomic configuration is taken from the MD and quenched to 0K to determine the structure and make

pictures of the microstructure from snapshots of the atomic configuration. We have done six simulations with the same geometry but different in the numbers of twin crystals and the numbers of stacking faults. The twinning deformation operates in response to the strain deformation. We found that the twinning mechanism in the martensitic microstructure is the same in every sample. Thus, we will explain the twinning mechanism in the context of a single simulation which covers all important features.

This simulation setup is equivalent to the strength test in real materials. Knowing how the strength can be related to the pattern of the microstructure is a useful key for designing materials. For this purpose the MD simulations can provide a rough clue for this relation before the strength test will be done with the real materials.

To understand the deformation mechanism, one must define certain reference points for atomic displacement. In fact, little displacement is required for creating stacking faults but large and complex displacement is required for turning one hcp variant into another. Since the bcc structure was well defined prior to the martensitic microstructure, it is convenient to use atomic coordinates in the bcc structure as a reference. It can be readily seen that when the bcc-hcp transition occurs, 12 out of 14 nearest neighbours of the bcc atom become the nearest neighbours of the hcp. The other two bcc nearest neighbours have moved a little further and fall into the second neighbouring shell in the hcp structure as shown in figure 6.3 (a). It shows the distribution of 14 bcc local coordinations in the hcp phase. Note that in an ideal transition to the perfect hcp structure the relative displacement of all 14 bcc nearest neighbours will never exceed 1Å; see section 4.1.1. By this mechanism the 12 nearest neighbours in the hcp phase will always come from the 14 nearest neighbours in the bcc.

However, if there is any more movement other than 1Å, it indicates that now some bcc nearest neighbours are no longer the nearest neighbours of the same atom in the hcp phase. This movement can be detected indirectly by the

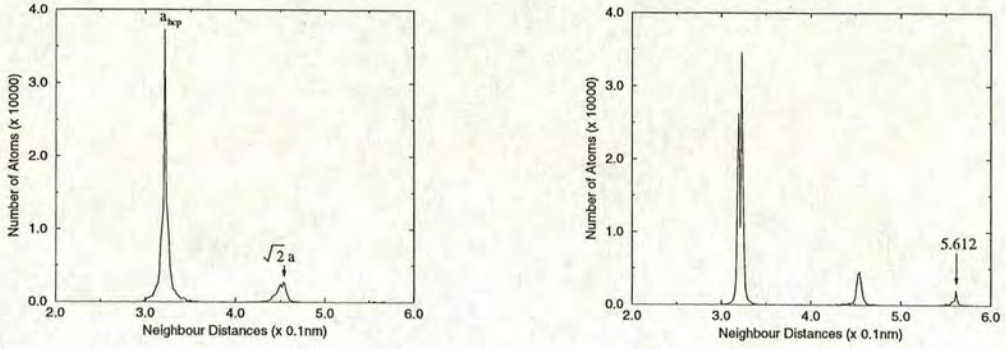

Figure 6.3: Graphs of the final separation between atoms originally in the first two shells of the bcc neighbours. They demonstrate plastic movement with respect to initial local coordinations in the bcc phase; a) from 14 bcc local coordinations, 12 become hcp nearest neighbours and the other 2 fall into the second hcp neighbouring shell. No 'plastic atom' occurs. The curve is taken from the constant volume MD simulation a few ps after the bcc-hcp transition at 600K. The sample contains 11,520 atoms; b) some atoms have moved away from their original nearest neighbours and fall into the fourth neighbouring shell in the hcp structure. The curve is taken from the same sample after yield stress is applied and plastic damage occurs.

distribution of 14 bcc local coordinations in the hcp phase as shown in figure 6.3 (b). We define this particular change of local coordination as 'plastic deformation' and the atom is classified as a 'plastic atom'. This atom might re-establish the hcp or fcc local environment. Sometimes the atom can only be classified as 'unknown' as its local environment corresponds to neither bcc, fcc nor hcp. In our illustration method (section 5.1) we colour each atom according to its current local structure; see table 5.1. Sometimes it is useful to colour 'plastic' atoms distinctively, i.e. by blue.

Most deformation processes, such as slip, require atomic displacements of $\approx a_{hcp}$ in some specific plane to regain perfect hcp structure; see figure 6.5. Dislocations are an example of a source of 'plastic' atoms. However, we will see

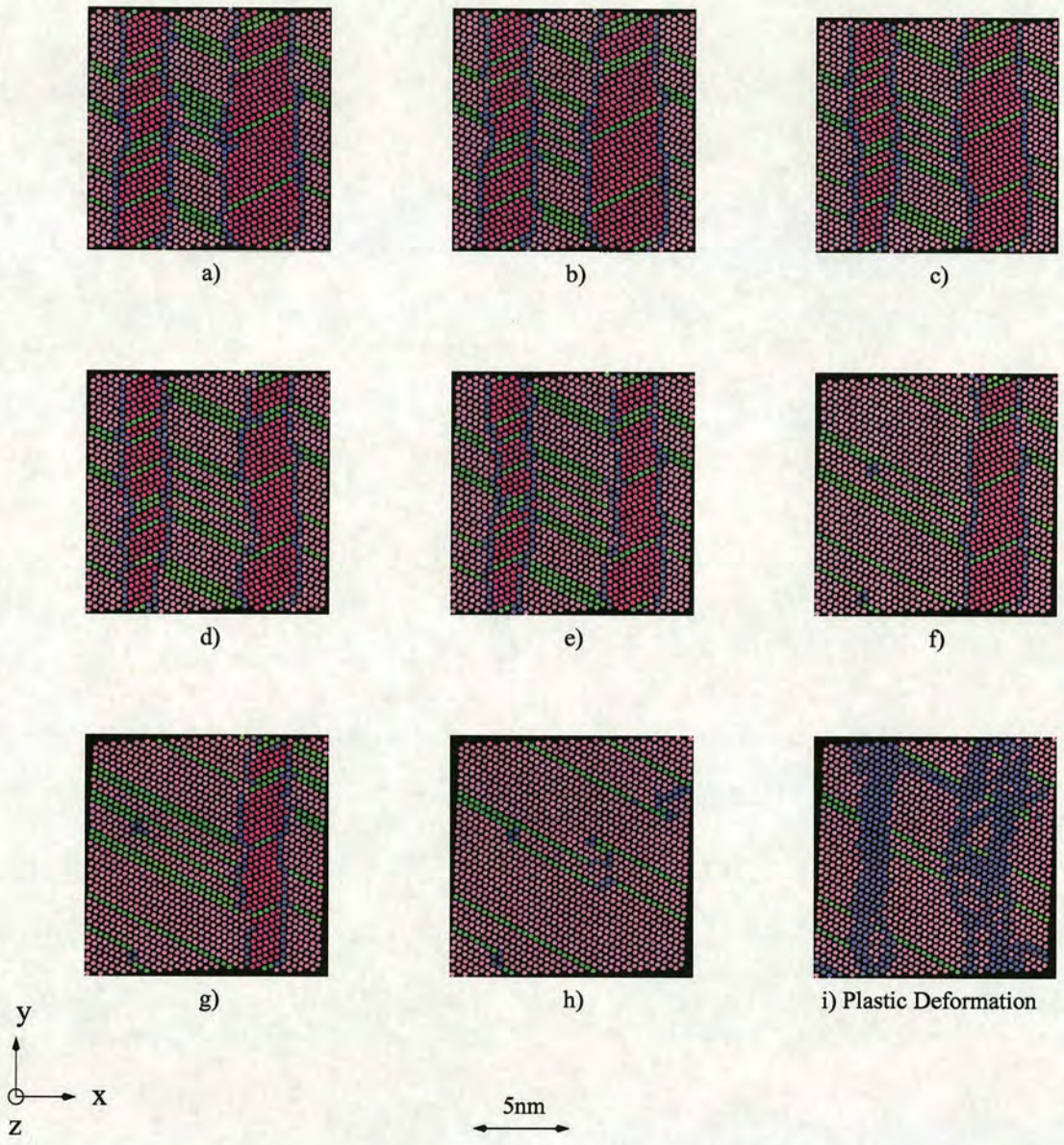

Figure 6.4: Relaxed microstructure taken from the MD simulations after applying a series of increasing strain at 600K. The system contains 11,520 atoms. Each snapshot is quenched and relaxed under constant stress conditions to 0K. The last picture shows the same picture as at (h) but the plastic atoms are labelled by blue. The colour scheme is defined by table 5.1.

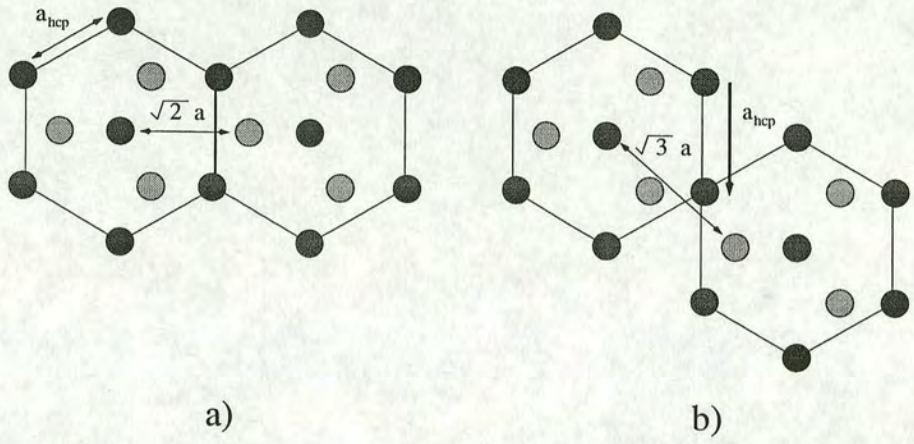

Figure 6.5: Shows a) perfect hcp structure; b) slip by $\frac{1}{3} < 1\bar{2}10 >$.

later that in the twinning process plastic atoms can be generated by a different mechanism.

A sample of twinned microstructure that contains 4 stripes and 4 boundaries subjected to increasing strain is shown in figure 6.4. The colour labelling is the same as in figure 5.13. The strain applied is up to 4.0% and the stress-strain relation is found. A typical curve is shown in figure 6.6. It has a stick-slip property. This property can be explained as follows: when strain is increased, stress is also increased proportionally. This is called stick phase. This is basically elastic deformation of the microstructure.

Twins move by a stick-slip mechanism.

At a certain amount of stress, the microstructure can no longer endure and undergoes a structural change. If the microstructure does not change severely, the stress-strain relation might be only slightly altered. However, if the change is severe, the curve in the stress-strain relation will exhibit a large discontinuous jump. This is called the slip phase. Stick-slip patterns repeatedly happen in

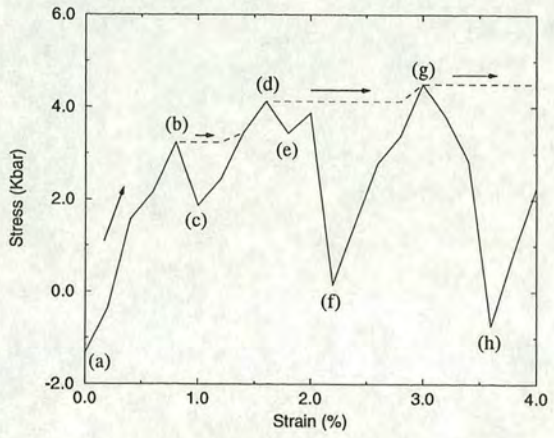

Figure 6.6: The stress-strain relation of martensitic microstructure at 600K during applying a sequence of increasing strain at the rate of 0.2% per 20ps. (a)-(h) label the same stages as in figure 6.4.

the stress-strain curve. We stop monitoring the twinning deformation when the twinned structure has disappeared.

Let us look at the microstructure in more detail. At no strain, figure 6.4 (a) and 6.6 (a), the microstructure is already under a little stress of -1.32 kbar. This is because the formation of microstructure and the existence of stacking faults are insufficient to compensate for the shape change during the phase transition.

When strain is increased, stress is also increased, as shown in figure 6.6 (a)-(b). The non-linear relation between stress and strain reflects a slight structural change. In fact a region of fcc crystal is removed from the microstructure; see figure 6.4 (b) and compare with (a). This removal of fcc corresponds to partial basal dislocations moving from one twin boundary to the other.

During strain to 1.0%, figure 6.4 (b) and (c), twin boundaries show a lot of activity in $[10\bar{1}1]$ direction. A part of twin boundary between two 'twin boundary steps' has a stepwise movement in the direction normal to the twinning plane while the 'twin boundary steps' move across the twin boundary. The detail of the 'twin boundary steps' was explained in section 4.2.3 and section 5.2.3.

The stepwise movement advances in $[10\bar{1}1]$ direction by $\frac{\sqrt{3}}{2}a_{hcp}\sin 61.5°$. From figure 6.4, we notice that the whole twin surface does not move simultaneously but looks more like it has been ripening as we have also seen earlier in section 5.2.5. The stepwise movement in the twinning process was also detected experimentally in titanium and zirconium using transmission electron microscopy by Song and Gray [30]. The sidewise propagation of twin steps in their experiments occurs under a local shear stress.

It can be readily seen that the twin boundary movement causes the stripes of red variant to be smaller and of purple variant to be larger. This is because the purple variant significantly reduces stress in $[10\bar{1}\bar{2}](10\bar{1}1)$. The mechanism can be explained as follows: with respect to a cubic box, the purple variant of the perfect hcp structure can be regarded as a box which is strained by $\approx 2.08\%$ in $[10\bar{1}\bar{2}](10\bar{1}1)$. Therefore if a cubic box is strained by 2.08% and suddenly all the structure in the box switches to the purple variant, the system will turn out to be under no stress. This is a major prediction provided by the elastic theory in chapter 4. However, in the simulation such a sudden structural change has never happened but rather a slowly growing process occurs.

The twinning mechanism progresses by the stick-slip process while the twin boundaries are moving. This is illustrated by figure 6.6 (b) and (c). Stress reaches a local maximum at 3.24 kbar and then drops to 1.87 kbar. Again at (d) and (e), stress is increasing to another maximum at 4.12 kbar then drops a little to 3.44 kbar. See the sequence of pictures in figure 6.4 (b)-(e).

The boundary movements continue until a stripe of red variant vanishes and the purple variant becomes dominant at 3.87 kbar. The two stripes of purple variant combine into one bigger stripe, leaving a step in layers of stacking faults. After this severe structural change, the stress drops extremely to 0.15 kbar at $\approx$ 2.2% strain; see figure 6.4 (f) and 6.6 (f).

The vanishing stripe of the red variant contains 12 layers of stacking faults

whereas the remaining stripe of the same variant has only 6 layers of stacking faults. This means that the variant that contains more stacking faults disappeared first. This is also true when we invert the direction of the shear - the purple variant that contains more stacking faults disappeared first. Thus the more 'twin boundary steps' on the twin boundary, i.e. the more stacking faults in the twin crystals, the more mobile the twin interfaces. This indicates that the 'twin boundary steps' can assist the twinning deformation. Thus twinning deformation might hardly happen in perfect twin structures where there are no step present.

During strain to 3.6%, figure 6.4 (f)-(h), some layers of stacking faults are created in purple variant. The boundaries also have a lot of movement activities. Again the purple variant becomes even bigger and the red variant becomes even smaller. At 3.6% strain, stress reaches a maximum at 4.50 kbar. The remaining stripe of red variant vanishes, only the purple variant has survived in the microstructure and then the stress drops to -0.73 kbar.

Deformation occurs by growth of one twin at the expense of another. Some 'plastic atoms' are created during the deformation process.

We found that during the twinning process, the eaten stripes have left a lot of 'plastic' atoms of which current local structures are still hcp or fcc. Figure 6.6 (h) and (i) show the microstructure at the same stage but in (i), the plastic atoms are blue. The presence of plastic atoms can be described as follows. Initially, the $(10\bar{1}1)$ planes parallel to the twin boundary have ...$aa'b'baa'b'ba$.. structural sequence where a and b have 13 and 11 nearest neighbours respectively, see section 5.2.3 for more detail. The primed symbols indicate the same local structure as the unprimed ones but different in height from the plane of the paper in figure 5.12. In order to move the twin boundary, the local boundary structure must discard

or accept one nearest neighbour from a nearby structure and hence a shuffling process occurs, leaving the microstructure with plastic deformation. The exact mechanism is unclear but the movement of the atoms must be $\approx a_{hcp}$ in order to retrieve the hcp structure.

As we have seen in section 3.3.3, the reverse transition also obeys the NW mechanism in which atomic movement never exceeds 1Å. Hence the movement greater than 1Å due to slips or shufflings that occur prior to the reverse transition can not be recovered and the shape memory effect is absent.

Unlike zirconium microstructure, ferroelastic materials have quite a different twinning mechanism [103, 104]; the interchange between variant structures occurs in such a way that local coordinations are the same. In some materials, this leads to the shape memory effect where the martensite can undergo a small deformation which is reversed on the inverse martensitic transition. This occurs because in deformation twinning macroscopic shape can be changed by slightly changing the microscopic local environment of atoms. As only little atomic movement is involved, the reverse transition atoms can 'remember' which were their neighbours and transform back exactly to their previous sites and the macroscopic shape is regained.

At the end of the simulations, we get a single piece of the purple variant which contains some stacking faults, for example the density of stacking faults in figure 6.4 (h) is 0.11. As discussed earlier, we can think of the purple variant as a strained cubic box. Because we start from the bcc lattice and the simulation supercells are contained in cubic simulation boxes, it is simple to use this box as a reference. After the bcc-hcp phase transition, we can regard the regular hcp variants as strained bcc structures. For example, the purple variant gives 2.08% strained in $[10\bar{1}2](10\bar{1}1)$ with respect to the original bcc supercell. We also showed in section 4.1.2 that the amount of this strain is linearly dependent on the number of stacking faults.

The plot of the $[10\bar{1}2](10\bar{1}1)$ shear strain measured from MD supercells which

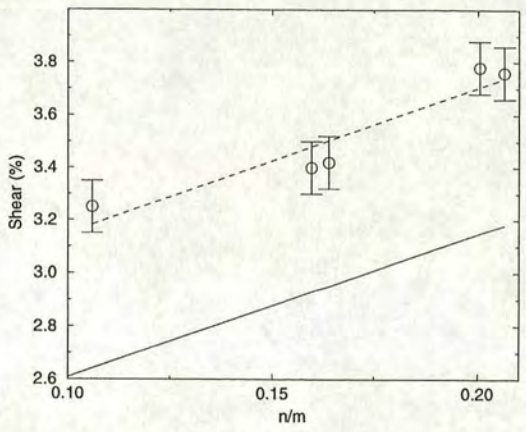

Figure 6.7: The plot of residue $[10\bar{1}2](10\bar{1}1)$ shear strain after only one variant remains in the microstructure against the number of stacking faults per total number of close-packed planes n/m. n/m is defined in section 4.1.4 and 4.2.2. Dashed line indicates possible linear dependence, compared with elastic theory in section 4.2.2 (solid line).

contain a single hcp crystal with some stacking faults against the number of stacking faults is shown by the dashed line in figure 6.7. Each point is averaged over 5 samples. This is in good agreement with the elastic theory (solid line) proposed in section 4.2.2. Even though the amount of shear predicted by the theory is incorrect, it qualitatively explains the linear dependence between shear and stacking faults.

We are also interested in the yield stress of different patterns in the microstructure. The yield stress is the ability of the microstructure to endure a certain amount of stress before undergoing a structural change. In this case, it is defined by the amount of stress that causes a stripe in a twinned microstructure to vanish. With the same geometry, we found that the yield stress of four-stripe twins (figure 6.8 (a)) is 4.47 kbar whereas two symmetric stripe twins (figure 6.8 (c)) require a yield stress of 6.9 kbar. These amounts are averages obtained from three constant strain MD simulations each.

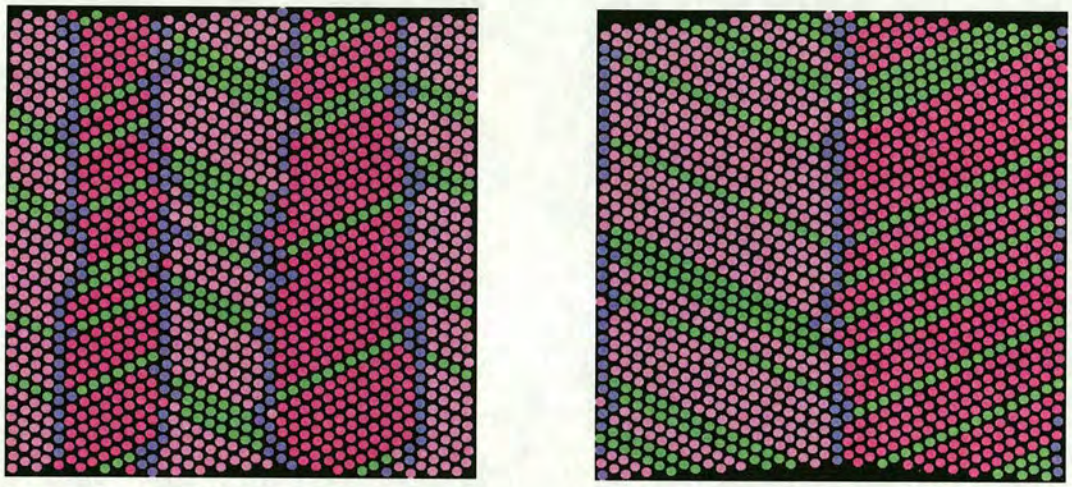

a) b)

Figure 6.8: Two typical twinned microstructures obtained from the MD simulations; a) four stripes $(10\bar{1}1)$ twins; b) two symmetric stripes. The yield stress is 4.47 kbar for (a) and 6.95 kbar for (b). The colour scheme is defined by table 5.1.

At our simulation scale, the yield stress is higher in a coarser twinned microstructure.

6.3.2 Perfect Twins

To study twinning deformation in perfect twins, we set up a perfect twin with orthogonal unit cells which z is aligned along $z = [1\bar{2}10]$. The number of unit cells is $8 \times 8 \times 8$ and the dimensions are $99 \times 94 \times 26\mathring{A}^3$ (10240 atoms). We set up a perfect twin with the twin boundary aligned along $(10\bar{1}1)$. We perform an equilibration run at 600K for 5ps. Then the sample is deformed by the strain method at 0.4% per 20ps in $[10\overline{12}](10\bar{1}1)$. Corresponding stress is measured and the microstructure is determined after each period of 20ps.

A typical stress-strain relation is shown in figure 6.9. We found that stress-

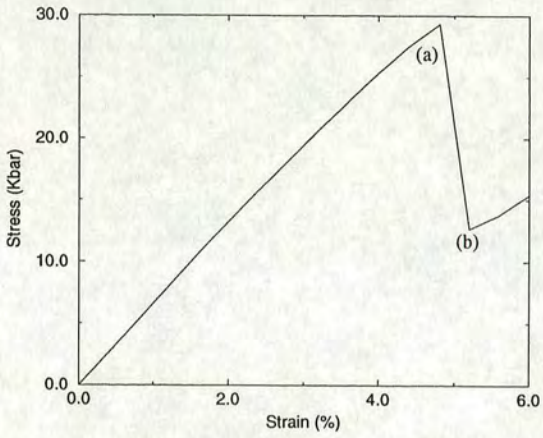

Figure 6.9: The stress-strain relation of perfect twins at 600K during applying a sequence of increasing strain at the rate of 0.4% per 20ps.

strain relation is linear from 0.0% to 4.4% strain and it requires 29.31 kbar to deform perfect twins; figure 6.9 (a). For a typical perfect twinned structure (figure 6.10 (a)), twinning deformation occurs in such a way that an extra variant is created inside a stripe of the twinned microstructure (figure 6.10 (b)). It also creates broad boundaries due to mismatch of orientation between variants; see section 5.2.3 for more detail about the boundaries. After the new variant is created, the stress drops to 12.62 kbar; figure 6.9 (b). The mechanism is different because there are no stacking faults and hence there are no 'twin boundary step' on the twin boundaries. We suggest that it would require a large amount of energy in order to move the entire boundary. Therefore the system does resort to other deformation processes. Furthermore, the perfect twins are far stronger than the martensitic microstructure.

Without twinning dislocations, twin boundaries cannot move.

In figure 6.10 (b), we see that stacking faults also exist but appear in every

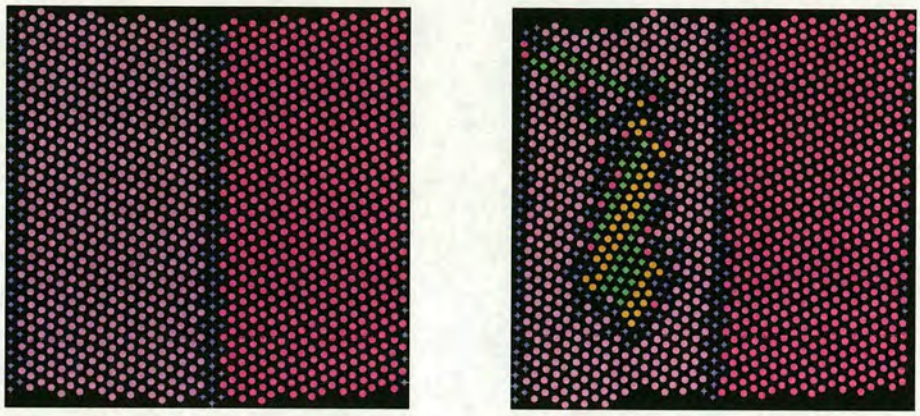

a) b)

Figure 6.10: Illustrates twinned microstructure taken from the MD simulation at 600K; a) starting configuration of perfect $(10\bar{1}1)$ twins with 10,240 atoms; b) deformation of (a) using constant strain method. The atomic configuration is quenched and relaxed under the constant stress scheme to 0K. The colour scheme is defined by table 5.1.

odd and even layer of the close-packed planes. We know that the former does not give rise to extra strain (figure 4.2). Again we believe that the existence of stacking faults is to form the 'twin boundary steps' and to assist the movement of the twin boundaries.

This is because the movement of twin boundaries is complicated as already shown in the last two sections. As studied by Serra and Bacon [98], twinning deformation in $(10\bar{1}2)$ twins operates under twinning dislocations once they have been nucleated. The twinning dislocations are steps on the matrix-twin interface. These steps can be moved at the critical resolved shear strain. Atoms in the intermediate planes have to be shuffled to restore the perfect hcp arrangement. The $(10\bar{1}2)$ twin boundary has a stepwise movement similar to our findings. This movement creating a series of dislocations to the twin boundary and generally these twinning dislocations in $(10\bar{1}2)$ twins are essentially mobile [38, 99, 100]. However, this twinning mechanism does not operate in $(10\bar{1}1)$ twins. Even though

the $(10\bar{1}1)$ twins contains some twinning dislocations, it is shown by using the MD simulations that these dislocations are sessile [38, 99, 100]. This also explains why $(10\bar{1}1)$ twins are less common in real materials than $(10\bar{1}2)$ twins [98].

6.4 Conclusions

We have used the strain method to study twinning deformation in the perfect twins and in the martensitic microstructure. We are interested in a particular case where the twin boundary is on the $(10\bar{1}1)$ and the strain is in $[10\overline{12}](10\bar{1}1)$. In the elastic regime we found that perfect twins and martensitic microstructure have a similar shear elastic constant; $G = 66$ GPa and 58 GPa respectively. During the deformation process, the martensitic microstructure deforms by broadening a hcp variant that reduces stress from the microstructure. A variant that cannot reduce the stress will shrink. Broadening can only occur by motion of the 'twin boundary steps' across the twin boundary. This leads to stick-slip property in the stress-strain relation, indicating a series of structural changes.

Plastic deformation is detected and is a result of structure interchanging between the hcp variants and the interfaces. This is one possible explanation for the absence of the shape memory effect in zirconium microstructure. During the twinning process, the boundaries move in a stepwise fashion. The length of the step is $\frac{\sqrt{3}}{2}a_{hcp}\sin 61.5°$ in the direction normal to the twin boundary. Stacking faults create the 'twin boudary steps' in the twin boundaries. We observed that stripes that contain more stacking faults - more steps on the twin boundary - are assimilated quickly and disappear first. Hence the 'twin boudary steps' and their associated stacking faults assist the movement of twin boundaries and ease the twinning deformation. It was predicted in section 4.2.2 that the amount of strain required for completing the twinning deformation is linearly dependent on the number of stacking faults contained in the variant. This is in good agreement with the results in section 6.3.1. We also found that at our simulation scale the

microstructures that contain bigger twin crystals are stronger. The yield strength is of order 5.0 kbar. Different deformation occurs in perfect twins. They deform by creating a new variant inside a twin crystal rather than a twinning deformation. This is because the perfect twin supercell contained no dislocations to assist the boundary movement. The strength of perfect twins is greater than 29 kbar.

Chapter 7

Conclusions

'By always thinking unto them. I keep the subject
constantly before me and wait till the first dawnings
open little by little into the full light.'

Sir Isaac Newton.

The bcc-hcp transition in zirconium is an example of a martensitic transition. It is a displacive transition which involves little atomic movements. In our calculations, we found that the transformation path obeys Nishiyama-Wessermann rules [1] which are

$$(110)_{bcc} \parallel (0001)_{hcp}, \tag{7.1}$$

and,

$$[1\bar{1}0]_{bcc} \parallel [1\bar{1}00]_{hcp}. \tag{7.2}$$

We have studied a large number of large scale simulations - up to 74,880 atoms - using the molecular dynamics method along with Nosé-Hoover constant temperature algorithm [60, 61, 62] and Parrinello-Rahman constant stress algorithm [64]. We chose a Finnis-Sinclair type potential derived for α zirconium [57] as a model case. The potential is in a simple form and accurately represents zirconium [25].

By using the normal mode calculations, we studied phonon properties in the stable bcc phase at high temperature. The phonon density in both bcc and hcp phases is calculated. We found that the T_{1N} mode in the bcc exhibits strong anharmonicity which can be modelled by an overdamped oscillator with $\Gamma = 0.6$THz at 1,600K. By comparing the normal mode calculations with the lattice dynamics method where the anharmonic effects are not included, the MD showed that the anharmonic vibration is needed in order to stabilise the bcc phase. We showed that the phonon density around 0.5THz is lowered considerably during the transition and the vibrational entropy is decreased by $0.73k_B$. This triggers the bcc-hcp transition. The concept of the excess vibrational entropy stabilising the high temperature phase is also applied to a wide range of martensitic transitions in alkali metals [20, 40] and some alloys [21].

We continued evaluating the time evolution of the T_{1N} modes which evolve through the bcc-hcp transition. The modes have finite frequency at the transition. During the structural changes, the frequencies of the modes split into 2-3 relatively higher frequencies ≈ 2.5 THz. This points out that if the reverse transition occurs in such a way that all atoms follow their previous trajectories to where they started the forward transition, it would require two or more phonon modes instead of one. If the reverse transition is triggered by one mode phonon, the path of the reverse transformation must be different from the forward transformation path. The martensitic transition in iron [41] and in NiMnGa alloys [85] are examples of different forward and backward transformation paths.

The bcc-hcp transformation in zirconium can be regarded as an elastic distortion of the bcc crystal. Starting from Nishiyama-Wessermann rules, we described martensitic microstructure as a strained bcc crystal. We found that microstructure is more energetically preferable than a single hcp crystal.

Similar strain models have been widely used for studying martensitic transitions. By symmetry considerations of the bcc lattice, Liakos and Saunders [89] expanded the strain energy up to the fourth-order terms in Landau theory. Sub-

sequent work by Gooding and Krumhansl [32] demonstrated that Landau theory can be applied to study the bcc-9R transformation in lithium, and minimising the strain energy in the Landau theory led to a first-order structural phase transition. They pointed out that the theory can describe the existence of stacking faults and deformation faults in the microstructure. Fradkin [101] extended the Landau theory to study the effect of external pressure and external stress to the fcc-bcc transition. As studied by Barsch and Krumhansl [102], Mazor and Bishop [103], Horovitz, Barsch and Krumhansl [104] and Jacobs [105], twinned microstructure in ferroelastic materials can be examined if appropriate gradient terms are included into the Landau expansion of the elastic free energy. The dynamics of twin boundaries can be simulated. By mapping the elastic model of the bcc-hcp transition in zirconium into a magnetic model and using Monte-Carlo simulations, Lindgård and Mouritsen [31] and Castán and Lindgård [33] confirmed that the bcc-hcp transition in zirconium is first-order. They also studied the kinetics of the martensitic microstructure. Domain boundaries, i.e. stacking faults and twin boundaries were observed.

Nevertheless, many physical properties such as anharmonicity, long range strain, exact number of variants, correct lattice orientations, anisotropic elasticity, twin boundaries, lattice defects and the appropriate symmetries of the transition were neglected from these strain models. Thus we resorted to atomistic simulations and the MD methods. By introducing the concept of 'local atomic structure', microstructures can be pictured. This allows studies of microstructure evolution at the atomistic level.

In our calculation the transition temperature is determined as 1,333K. At the early stage of the phase transition, the number of martensite atoms grows as t^3. The final microstructure obtained from the MD simulations is dominated by stripes of the $(10\bar{1}1)_{hcp}$ twins with some stacking faults contained in each hcp crystal. In the previous study in TiV alloys [34], no microstructure was observed. We believe that in the TiV study the size of the simulations was too small.

We have seen from our simulations that the strain field in the microstructure makes a preferential selection of the hcp variants [25]. Further study by Maier *et al.* [106] using elastic neutron scattering experiment also found that external strain promotes the martensitic transition in alkali metals. They suggested that this external strain must be in a specific mode, i.e. $[110]_{bcc}$ shear type as in zirconium. If the strain field is random, it will inhibit the transformation.

When no bcc persists, we found that the twinned microstructure exhibits slightly further evolution where twins become coarsened and leave some plastic damage to the microstructure. The plastic atoms are caused because the coordination numbers between boundary structures and the hcp phase are different, and then some atoms must be shuffled in order to reestablish a regular hcp structure after the boundary has swept through.

In real zirconium, the microstructure produced by the martensitic transition has a 'lath' structure [26]. A 'lath' is a plate-shaped hcp region of which one lateral dimension is much smaller than the other two and in addition the two larger dimensions are very unequal. The martensite regions are the integrated structure of these 'laths'. The twin formation hardly occurs via the phase transition [26, 30]. This is in contrast with our findings. We believe that this discrepancy occurs because in real zirconium the bcc-hcp transformation follows the Burgers path [23, 26, 27, 28, 29] whereas in our simulations the transformation obeys the NW rules. However twin formation is important in understanding the mechanical properties of a number of materials, including zirconium itself [4, 37]. It has been widely studied in both theory [38, 43] and experiment [4, 37, 39]. Furthermore, it is the fundamental cause of shape memory and ferroelastic materials. Some researchers believe that twinned microstructure also affects the phonon and electronic properties of high T_c superconductors [102, 103, 104, 105].

The simulations of twinning deformation in twinned microstructure were carried out by using the strain method. We found that the shear modulus is of order 50 GPa. During the deformation process, a stripe of twins grows at the expense

of another, leading to the stick-slip mechanism. 'Plastic' atoms were created as a result of interchanging structure between the hcp variants. This is one possible explanation for the absence of shape memory effect in zirconium microstructure. Typical yield stress of the martensitic microstructure is of order 5.0 kbar whereas typical yield stress of the perfect twins is of order 30 kbar. The deformation mechanisms of these microstructures are rather different: in martensitic twins there are a number of the 'twin boundary steps' and their associated stacking faults which assist the interface movements and ease the twinning deformation but in perfect twins where there are no such dislocations present they deform by introducing a new hcp crystal inside the twin crystal.

In pure zirconium, yield stress is of order 2.0 kbar [4, 35] which is less than in our calculations. This is because in real zirconium there are a number of deformation modes including several twinning modes, i.e. slip in $\frac{1}{3} < 1\bar{2}10 > \{1\bar{1}00\}_{hcp}$ [26, 35, 36] and $\frac{1}{3} < \bar{1}\bar{1}23 > \{10\bar{1}1\}_{hcp}$ [35] and $\{10\bar{1}1\}_{hcp}$, $\{10\bar{1}2\}_{hcp}$, $\{11\bar{2}1\}_{hcp}$ and $\{11\bar{2}2\}_{hcp}$ twinning [26, 30, 38, 39]. Moreover, some twinning modes with some dislocations are essentially mobile [38, 99, 100].

Computer simulations have proved to be a powerful tool in studying the microstructure at the atomic level. For example, the structure of dislocation twinning in $\{10\bar{1}1\}_{hcp}$ twin in titanium calculated by an empirical potential and the MD method [44] is in excellent agreement with the result from high-resolution electron microscopy. This gives us confidence in our simulation results which are yet to be clarified by experiments.

Appendix A

Smoothing Spectrum and Maximum Entropy

As we have seen in chapter 3, equations (3.5), (3.6) and (3.18) concern the evaluation of the power spectrum, $P(\omega)$. One might approximate $P(\omega)$ numerically by applying a data windowing function and the discrete Fourier transform. This approximation is fully reviewed by Press, *et al.* [68]. The discrete Fourier transform provides the discrete power spectrum, $P(\omega_k)$, at different points k in the frequency space as follows. The discrete Fourier transform, C_k, of N-point sampled data c_j with sampling interval Δ is

$$C_k = \sum_{j=0}^{N-1} c_j w_j e^{2\pi i j k/N}, \tag{A.1}$$

where k runs from 0,1,2,...,$(\frac{N}{2}-1)$ and w_j is a windowing function, for example the Barlett (triangular) windowing function of the form

$$w_j = 1 - \left| \frac{j - \frac{1}{2}N}{\frac{1}{2}N} \right|. \tag{A.2}$$

This windowing is needed mainly because it will improve the sharpness of the spectral peaks without shifting the peak positions. The discrete Fourier transform

alone will provide poor spectral quality since the signals in equation (3.4) and (3.21) are sampled in a short and finite period with limited number of sampling points.

The power spectrum can then be estimated by

$$P(\omega_k) = \frac{1}{W_{ss}}(|C_k|^2 + |C_{N-k}|^2), \tag{A.3}$$

where k runs from 0,1,2,...,$(\frac{N}{2} - 1)$, $\omega_k = \frac{2\pi k}{N\Delta}$, the cutoff frequency $\omega_c = \frac{2\pi}{\Delta}$ and

$$W_{ss} = N \sum_{j=0}^{N-1} w_j^2. \tag{A.4}$$

However, $P(\omega_k)$ is not exactly equal to $P(\omega)$ but rather an average of $P(\omega)$ over a narrow range of ω. A better approximation is to evaluate $P(\omega_l)$ where the number of points $n_l > n_k$, then sum $P(\omega_l)$ over m consecutive l to obtain one smoother spectrum $P(\omega_k)$, k being the middle point among those summed l. In this method, the standard deviation is reduced by a factor $1/\sqrt{m}$ [68]. Note that we employ a sum operator rather than an average because we need to conserve the normalisation property of $P(\omega)$; equation (3.20). This method has been applied to the curves of phonon density in figure 3.7 and 3.12.

An alternative method to estimate $P(\omega)$ is the so-called maximum entropy method (MEM) [58]. It produces the most uniform spectrum consistent with a set of data. The method starts from generating several trial fitted spectra $P_{fit}(\omega)$. The inverse transform of those $P_{fit}(\omega)$ is denoted by $Q_{fit}(t)$. A good fit [58] is obtained by maximising

$$-\sum_{\omega} P_{fit}(\omega) \ln P_{fit}(\omega) + \frac{\lambda}{2}\chi^2 \tag{A.5}$$

where

$$\chi^2 = \sum_{t} |Q_{fit}(t) - Q_{data}(t)|^2. \tag{A.6}$$

The term $P_{fit}(\omega) \ln P_{fit}(\omega)$ is known as the information-theoretical entropy and λ is a Lagrange multipier which keeps χ^2 constant. In other words, the $P_{fit}(\omega)$ that produces the maximum entropy according to equation (A.5) is a good fit to $P(\omega)$, as is suggested by the name.

In fact we are free to choose the functional form of $P_{fit}(\omega)$. Nevertheless, Press *et al.* [68] suggested that the form

$$P_{fit}(\omega) = \frac{a_0}{|1 + \sum_{k=1}^{M} a_k e^{i\omega\Delta}|^2} \tag{A.7}$$

has a special feature which can fit sharp spectral peaks. A set of coefficients a_k is obtained by fitting. This function has a free order parameter, denoted by M in equation (A.7). A different order parameter results in the different features of spectral peaks. To choose a correct order parameter and avoid difficulties, we compared MEM with the conventional discrete Fourier transform. Throughout the present work, we have used MEM for determining anharmonic phonon frequencies in equation (3.5) and comparing with the frequencies extracted from the triangular (Barlett) windowing function (A.2) and the discrete Fourier transform (A.1).

Appendix B

Rotational Operations

In chapter 4, we perform the axis rotations from x_i'' to x_i' and from x_i' to x_i. The double primed coordinate systems transform into the primed coordinate systems by

$$x_i' = \underline{\varphi}_a x_i'', \tag{B.1}$$

where a = 1,2,3,4,5 and 6, and the strain tensors transform by

$$\underline{\varepsilon}_a' = \underline{\varphi}_a \underline{\varepsilon}_a'' \underline{\varphi}_a^{-1}, \tag{B.2}$$

where

$$\underline{\varphi}_1 = \begin{pmatrix} \cos 45 & -\sin 45 & 0 \\ \sin 45 & \cos 45 & 0 \\ 0 & 0 & 1 \end{pmatrix}, \tag{B.3}$$

$$\underline{\varphi}_2 = \begin{pmatrix} \cos 45 & \sin 45 & 0 \\ -\sin 45 & \cos 45 & 0 \\ 0 & 0 & 1 \end{pmatrix}, \tag{B.4}$$

$$\underline{\varphi}_3 = \begin{pmatrix} \cos 45 & 0 & -\sin 45 \\ 0 & 1 & 0 \\ \sin 45 & 0 & \cos 45 \end{pmatrix}, \tag{B.5}$$

$$\underline{\varphi}_4 = \begin{pmatrix} \cos 45 & 0 & \sin 45 \\ 0 & 1 & 0 \\ -\sin 45 & 0 & \cos 45 \end{pmatrix}, \tag{B.6}$$

$$\underline{\varphi}_5 = \begin{pmatrix} 1 & 0 & 0 \\ 0 & \cos 45 & -\sin 45 \\ 0 & \sin 45 & \cos 45 \end{pmatrix}, \tag{B.7}$$

$$\underline{\varphi}_6 = \begin{pmatrix} 1 & 0 & 0 \\ 0 & \cos 45 & -\sin 45 \\ 0 & \sin 45 & \cos 45 \end{pmatrix}. \tag{B.8}$$

For example,

$$\underline{\varphi}_1[1\bar{1}0] = \sqrt{2}[100], \tag{B.9}$$

$$\underline{\varphi}_1[110] = \sqrt{2}[010], \tag{B.10}$$

and

$$\underline{\varphi}_1 \begin{pmatrix} \alpha' & \Delta & 0 \\ \Delta & \beta' & 0 \\ 0 & 0 & \gamma \end{pmatrix} \underline{\varphi}_1^{-1} = \begin{pmatrix} \alpha + \Delta & \beta & 0 \\ \beta & \alpha - \Delta & 0 \\ 0 & 0 & \gamma \end{pmatrix}. \tag{B.11}$$

The primed coordinate system transforms into the unprimed coordinate system by

$$x_i = \underline{\varphi}_3 \underline{\varphi}_2 \underline{\varphi}_1 x_i', \tag{B.12}$$

and the strain matrix transforms by

$$\underline{\varepsilon}_a = \underline{\varphi}_3 \underline{\varphi}_2 \underline{\varphi}_1 \underline{\varepsilon}_a' \underline{\varphi}_1^{-1} \underline{\varphi}_2^{-1} \underline{\varphi}_3^{-1}, \tag{B.13}$$

where

$$\underline{\varphi}_1 = \begin{pmatrix} 1 & 0 & 0 \\ 0 & \cos 45 & -\sin 45 \\ 0 & \sin 45 & \cos 45 \end{pmatrix}, \tag{B.14}$$

$$\underline{\varphi}_2 = \begin{pmatrix} \cos 35.264 & 0 & -\sin 35.264 \\ 0 & 1 & 0 \\ \sin 35.264 & 0 & \cos 35.264 \end{pmatrix}, \tag{B.15}$$

and

$$\underline{\varphi}_3 = \begin{pmatrix} \cos 30 & -\sin 30 & 0 \\ \sin 30 & \cos 30 & 0 \\ 0 & 0 & 1 \end{pmatrix}. \tag{B.16}$$

For example,

$$\underline{\varphi}_3\underline{\varphi}_2\underline{\varphi}_1[1\bar{1}0] = \sqrt{2}[100], \tag{B.17}$$

$$\underline{\varphi}_3\underline{\varphi}_2\underline{\varphi}_1[11\bar{2}] = \sqrt{6}[010], \tag{B.18}$$

$$\underline{\varphi}_3\underline{\varphi}_2\underline{\varphi}_1[111] = \sqrt{3}[001], \tag{B.19}$$

and

$$\underline{\varphi}_3\underline{\varphi}_2\underline{\varphi}_1 \begin{pmatrix} \alpha & \beta & 0 \\ \beta & \alpha & 0 \\ 0 & 0 & \gamma \end{pmatrix} \underline{\varphi}_3^{-1}\underline{\varphi}_2^{-1}\underline{\varphi}_1^{-1} = \begin{pmatrix} 2.11 & 0.00 & 0.00 \\ 0.00 & -2.68 & 9.60 \\ 0.00 & 9.60 & 4.10 \end{pmatrix}. \tag{B.20}$$

Appendix C

Published Papers

PHYSICAL REVIEW B VOLUME 58, NUMBER 17 1 NOVEMBER 1998-I

Simulation of martensitic microstructural evolution in zirconium

U. Pinsook and G. J. Ackland
Department of Physics and Astronomy, The University of Edinburgh, Edinburgh, EH9 3JZ, Scotland, United Kingdom
(Received 4 March 1998)

A twinned microstructure is frequently observed after a martensitic phase transition. In this paper we investigate the atomic-level processes associated with the twin formation in a model system, using a many-body potential parametrized to represent zirconium. Molecular-dynamics simulations of the martensitic phase transition from bcc to hcp in zirconium show the evolution of a laminated twinned microstructure. Plastic deformation also occurs, creating basal stacking faults. The plastic deformation is such as to cause a rotation of the twins. This alters the twinning angle to the 61.5° angle of the low-energy $(10\bar{1}1)_{hcp}$ twins. These are thus identified as a cause of microscopic irreversibility in the transition. [S0163-1829(98)01534-3]

I. INTRODUCTION

A number of metals which have the body-centered-cubic (bcc) structure at high temperature exhibit a temperature-induced phase transition to a hexagonal-close-packed (hcp) phase at low temperature. This is a first-order martensitic transition, which proceeds via the Nishayama-Wassermann mechanism.[1] This is associated with the instability of a transverse N-point phonon in the bcc lattice and occurs when the temperature is lower than 1136 K. This phonon is stabilized by large anharmonic fluctuations at a higher temperature.[2,3]

In previous work, the development of martensitic microstructure during the transition has been investigated by a simplified model, using strain components as the order parameters.[4,5] In that model, anharmonic effects were included, but the existence of hcp variants was limited to two possible orientations. In practice, the symmetry of the phase transition allows for up to six equivalent hcp variants, all of which should be included for a realistic atomistic study.

Here we employ the molecular-dynamics approach in which atoms are treated individually, and so the appropriate symmetries of the transition are automatically included. Furthermore, the full anharmonicity can be included via the interatomic potential, as is the relative stability of the various crystalline phases, their point, line, and planar defects, and the anisotropic elasticity. To examine microstructure, large numbers of atoms are required because of the possible importance of long-range strain fields in nucleation. Thus the potential must have a functional form that is sufficiently fast to compute that large-scale calculations are feasible.

Obtaining a potential that satisfies all these criteria is not straightforward. For this reason previous simulational work at the atomistic level has been rather limited. Using static relaxation the energetics and relaxed structure of twins and twinning dislocations in the hcp phase have previously been studied,[6,7] as has the collapse of vacancy loops and generation of basal and prism stacking faults.[8] Anomalies in vacancy and self-diffusion migration have also been reported,[9] and these have been shown to be associated with the non-ideal c/a ratio of zirconium.[10] The bcc phase itself has been characterized as being dynamically stabilized by phase fluctuations.[11]

In a previous molecular-dynamics (MD) study the evolution of the transition in a titanium-vanadium alloy has also been simulated at a low temperature,[12] but no twinned microstructure was observed. Likewise, the martensitic transition in iron has also been investigated using MD: this differs from zirconium in that it is between face centered cubic (fcc) and bcc rather than hcp and fcc. Again no microstructure was observed.

In our study, we use molecular dynamics to simulate the time evolution of martensite microstructure after rapid quenching from the bcc phase to 600 K. We show that for simulations above a certain size, a twinned microstructure is developed that has been suppressed by finite-size effects in previous studies. We report a number of features in the transition, including stress-induced nucleation and subsequent ripening of the microstructure. In principle, the transition mechanism is microscopically reversible, but we show that plastic deformation occurs, driven by the energy cost of forming the twin boundary; this is very sensitively dependent on the crystal geometry.

II. THE POTENTIAL

The series of molecular dynamics simulations reported here were done using the MOLDY code[13] with a 1-fs time step and up to 11 520 atoms. A many-body interatomic potential was used,[14,15] and since it will be shown that the results are closely related to other predictions of the potential, these will be reviewed briefly here.

The potential was fitted to the anisotropic elastic properties of the material, the nonideal c/a ratio (1.595), the cohesive energy of the hcp crystal structure relative to other possible structures,[16] and the energetics of vacancies and stacking faults. It has been shown to give a good description of other point-defect properties[16] and twin-boundary energies.[6] This is important since defects may be generated during the phase transition, and the scale of the energy minimizing microstructure is governed by the relative energies of twin boundaries and strain.[17,18]

The potential gives a good description of both bcc and hcp phases, with a phase transition from bcc to hcp occurring between 1330 and 1390 K (Ref. 19) depending on cooling rate and boundary conditions.

The energy is written in the form[20]

TABLE I. Parameters for potential function.

k	A_k (eV/Å^3)	R_k (Å)	a_k (eV^2/Å^3)	r_k (Å)
1	−0.61248219	5.5763004	0.50569395	5.5763004
2	0.87645549	5.4848856	−0.00890725	4.7992749
3	−0.21947820	5.2106413		
4	−0.01371379	4.3422011		
5	0.68830444	3.6565904		
6	1.45995293	3.1995166		

$$E_i=\frac{1}{2}\sum_j V(r_{ij})-\sqrt{\rho_i}, \tag{1}$$

where

$$V(r)=\sum_{k=1}^{6} A_k(R_k-r)^3H(R_k-r), \tag{2}$$

and

$$\rho_i=\sum_j \phi(r_{ij})=\sum_j \sum_{k=1}^{2} a_k(r_k-r_{ij})^3H(r_k-r_{ij}), \tag{3}$$

where $H(x)$ is the Heaviside step function, r_{ij} is the separation between atoms i and j, and the fitted parameters are given in Table I.

The potential does not model the rapid electronic heat conduction, so the temperature in the simulation is regulated with a Nose-Hoover thermostat to remove the latent heat released by the phase transition.

One other feature of the model is worthy of note: the primary dislocation slip system according to this model is basal slip, not prism slip as observed experimentally. This may be due to the low basal stacking fault energy, which allows basal dislocations to split into partials connected by a ribbon of stacking fault. Basal slip is common in hcp metals, but is believed to be a secondary slip mechanism in zirconium.[21]

III. TRANSITION MECHANISM

The conventional model for the transformation from bcc to hcp can be regarded as an orthorhombic distortion of the bcc lattice. An hcp variant requires a compression of 9.6% along one of $\langle 001\rangle_{bcc}$ direction and an extension of 10.9% in a corresponding $\langle 110\rangle_{bcc}$ direction to form a close-packed plane from a $(1\bar{1}0)_{bcc}$ plane. From various combinations of these directions, it can be seen that there are six possible hcp martensite variants, corresponding to different orientations of the c axis, into which bcc can transform.

The transformation is not purely defined by a strain of the unit cell, since a relaxation of the internal coordinates is also required, i.e., alternate $(1\bar{1}0)_{bcc}$ layers shuffle by 0.94 Å. This corresponds to a freezing in of the N-point phonon in the bcc lattice. If this shuffle does not occur cooperatively throughout the variant, stacking faults can be formed within a single variant. This is the Nishayama-Wassermann mechanism; the shuffle of successive layers distinguishes it from the Burgers mechanism that obtains the same orientation between bcc and hcp but in which the atoms move into these positions via a shear of successive layers. In a martensitic transition the Nishayama-Wassermann mechanism is preferred because it leads to less overall change of shape of the crystallite.

The maximum distance moved by individual atoms in this perfect transition path relative to their neighbors is 0.47 Å, so the mechanism is martensitic rather than diffusive. Curiously, the equivalent of the N-point phonon that would be involved in the reverse (hcp-bcc) transition is not a normal mode in the hcp lattice.[22] This may also explain the observation that the Burgers mechanism is responsible for the bcc to fcc transition in iron, while the Bain mechanism is followed in the reversed fcc to bcc.

The $\langle 111\rangle_{bcc}\rightarrow\langle 10\bar{1}0\rangle_{hcp}$ directions consist of a line of nearest neighbors in both structures, so there is very little strain in this direction during the transition. Moreover, for a given $\langle 10\bar{1}0\rangle_{hcp}$ direction, there are three hcp variants with close-packed planes containing this direction. Consequently, combinations of these three variants can be viewed in a planar slice perpendicular to this direction. For this reason, it is convenient to set an axis of the initial simulation cell along $\langle 111\rangle_{bcc}$.

IV. CALCULATIONS

We performed a number of simulations of 50-ps duration using a 1-fs time step and a fourth-order Gear predictor-corrector algorithm. The initial conditions comprise a homogeneous high-temperature bcc lattice a with the equilibrium value of the lattice parameter corresponding to the potential at 1400 K. Quenching to 800 or 600 K was done either by instantaneous rescaling of the temperature, or by use of the Nose-Hoover[23] thermostat. Boundary conditions were either constant volume or constant pressure in the Parrinello-Rahman[24] scheme. The qualitative results were independent of these parameters.

A range of unit-cell shapes and sizes were investigated. Two orientations were tried: the unit cell oriented along $(100)_{bcc}$, $(010)_{bcc}$, and $(001)_{bcc}$ or along $(1\bar{1}0)_{bcc}$, $(11\bar{2})_{bcc}$, and $(111)_{bcc}$. In both cases the transition was via the Nishiyama-Wassermann mechanism,[1] as described above.

Analysis of the simulation was performed every 5 ps as follows. The temperature was taken from the instantaneous kinetic energy via the standard relation $KE=1.5k_BT$ while the overall crystal structure was determined from the radial distribution function (Fig. 1 shows typical radial distribution functions for hcp and bcc).

The microstructure was examined by taking a snapshot from the MD simulation and then relaxing the atoms to their local minimum-energy configuration. From the relaxed structure, each atom was classified as hcp, bcc, or fcc according to its nearest-neighbor coordination shell, considering both symmetry and orientation. Assuming the Nishayama-Wassermann mechanism, there are six possible directions for the hcp c axis and these variants were identified separately. As described above, only three variants were ever observed in a single simulation. Some atoms, typically at twin boundaries, cannot be classified by this method and are labeled "unknown."

Once the atoms have been associated with a particular

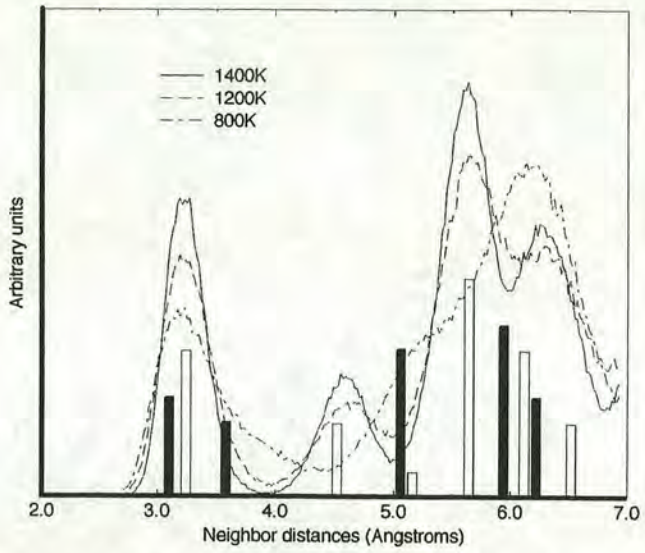

FIG. 1. The high-temperature phases are identified from their radial distribution function: the graph shows the characteristic hcp pattern at 800 and 1200 K, while at 1400 K the bcc pattern [broad first peak containing 14 (two shells) neighbors, absent second peak] is clearly different. The filled bars show the ideal peak positions for a bcc structure and the open bars those for hcp, while the bar heights are proportional to the number of atoms at that location. Quenching instantaneously to 0 K gives an hcp radial distribution function in each case.

structure, the $(111)_{bcc}$ direction which defined the plane of the microstructure was deduced. The different local coordinations were plotted in different colors, and slices through the sample perpendicular to the $(111)_{bcc}$ direction were examined visually to determine the microstructure.

A large number of simulations have been performed, with varying crystallographic orientation of the bcc lattice, and varying aspect ratio. A number of common features emerge, which we discuss generally, and then illustrate in the context of a single simulation.

V. STRESS-INDUCED PREFERENTIAL NUCLEATION AND METASTABLE PHASE FORMATION

Immediately on cooling, a region of hcp is nucleated. Because of the transition strain, this hcp region sets up a stress field around it in the plane of that strain $(111)_{bcc}$. This stress field can be accommodated by formation of the other two variants for which this particular $\langle 111\rangle_{bcc}$ lies in the close-packed plane. Thus two more variants are preferentially nucleated, and a columnar structure is established. Note that while the specifics of this nucleation depend on the transition mechanism, the preservation of lines of close-packed atoms (here $\langle 111\rangle_{bcc}$) is common to most martensitic transitions. Thus we believe that this is a general feature that will reduce the number of nucleated variants below that which is geometrically possible. Furthermore, because only a small amount of strain is required, the martensite can grow very quickly along the direction of the preserved close-packed line, defining the preferred plane for the martensite/parent interface.

As soon as the growing nuclei meet one another, a 60° rotation twin boundary is formed, the angle being that between, e.g., the $(101)_{bcc}$ and $(110)_{bcc}$ planes in the parent phase. This boundary may be either symmetric or asymmetric: If only two variants are present in a laminate microstructure, then all boundaries can be symmetric, but if finite regions of all three variants are present, some asymmetric boundaries must be formed. In the present case, the symmetric boundary has lower energy, and this provides a driving force for the elimination of one of the variants.

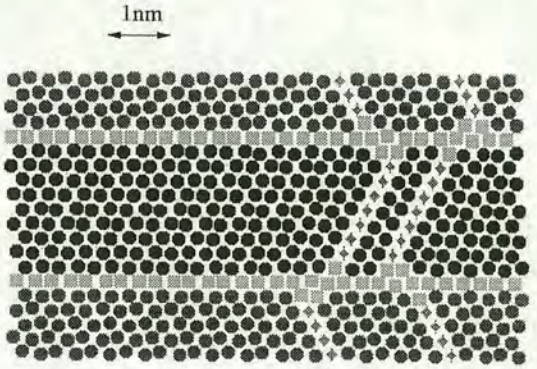

FIG. 2. A relaxed configuration indicating the structure of the twins. Darker circles represent the two hcp variants and stars are stacking faults that have local fcc coordination. Squares are boundary atoms that cannot be classified as hcp or fcc. The long straight sections have identical structure to the $(10\bar{1}1)_{hcp}$ twin boundaries calculated by Serra and Bacon (Ref. 6), while the stacking faults serve to rotate the twins towards 60°.

An interesting feature that occurs in the very early stages of microstructural evolution is the appearance of the fcc structure. This structure has a higher free energy than hcp, both according to the potential and in real zirconium. However, it is able to form a low-energy grain boundary with all three variants simultaneously. Thus it is found that for rapid cooling where the microstructure is very fine, small regions with the fcc structure appear. These regions may persist while all three variants still exist, but once the laminar microstructure is established, they are eliminated. It is worth noting, however, that in those regions that transform first to fcc and then to bcc, the "memory" of their original position in the bcc structure is lost. This may be a microscopic cause for the absence of the shape memory effect in zirconium (other sources of plastic deformation will be discussed later).

VI. STACKING FAULTS AND TWIN ROTATION

The relationship between the stacking faults and the transition is of interest, since stacking faults are metastable defects but do not anneal out in our calculations. In zirconium, we find that the tilt angle between two bcc-derived variants is 60°; this is very close to the 61.5° symmetric tilt boundary of $(10\bar{1}1)_{hcp}$ twins with low boundary energy that we calculate as 165.8 mJ m^{-2} according to this potential following the methods of Refs. 6 and 25. The twin boundary straightens toward $(10\bar{1}1)_{hcp}$.

There remains a discrepancy in angle that is made up by twinning dislocations; however, when the twins are small these may appear as partial twinning dislocations with a basal stacking fault extending through the twins (see Fig. 2). Close inspection shows that these stacking faults are not ar-

ranged at random, but rather an even number of layers apart leading to a systematic rotation of the variants toward the 61.5° angle that minimizes the boundary energy. To obtain that strain exactly would require one stacking fault every ten close-packed planes. Over a series of 30 calculations we have found an average of one stacking fault per 9.7 close-packed planes, in excellent agreement with the theoretical value. By motion of these stacking faults it would be possible for the crystal to deform plastically and the boundary to evolve to the stable $(10\bar{1}1)_{hcp}$ tilt without much diffusion of atoms from the parent bcc phase positions. However, although some mobility of the stacking faults is observed, it is too slow for this annealing process to occur on the time scale of our simulations.

VII. A TYPICAL SIMULATION

Having described the individual features of the transition microstructure, we now illustrate the entire process by following a single simulation.

The orientation of the bcc lattice with respect to the simulation cell is $x=[1\bar{1}0]_{bcc}$, $y=[11\bar{2}]_{bcc}$, and $z=[111]_{bcc}$. The dimensions of the cell are set to $x=101.50$ Å, $y=105.48$ Å, $z=24.86$ Å. To simulate the initial bcc phase and the final hcp phase in the same simulation, we use periodic boundary conditions and find that no remnant of the bcc phase persists at low temperature. After equilibration, the temperature is reduced to 600 K where the simulation is run and the evolution of the microstructure followed.

In our chosen simulation, the $\langle 111\rangle_{bcc}$ direction that transforms to $\langle 10\bar{1}0\rangle_{hcp}$ lies along the z axis of our simulation cell. This means that we can represent the microstructure by considering a single xy-plane slice, as in Fig. 3. The other such planes are similar.

Within the first 5 ps, Fig. 3(a), four strips of laminated 60° twins are formed. These twins correspond to two of the possible hcp variants. The twin boundary is close to the $(10\bar{1}1)_{hcp}$ plane. Referring to experimental and other computational results, $(10\bar{1}1)_{hcp}$ twins grow only under a highly stressed sample at high temperature.[6,7] Here, the 60° angle is forced by the relationship to the parent bcc phase. At this stage, some metastable structures including a number of stacking faults (which manifest themselves as diagonal lines of fcc-coordinated atoms) are produced, and a small region of rather random close packing is nucleated.

By 10 ps, the random close-packed region has ordered into a small lump of the third hcp variant.

During the period to 30 ps, the thinner of the strips of one hcp variant is gradually replaced by the other variant. This coarsening of the microstructure is analogous to Ostwald ripening, in which two twin boundaries are removed. The atoms in this region have now moved away from their previous sites in plastic deformation, and they have a different set of nearest neighbors.

After 40 ps, only three regions of three distinct variants are left. Two variants clearly dominate forming the familiar martensitic laminate microstructure. The final two figures show a small amount of further evolution as the boundaries straighten and sharpen.

The final picture is at 50 ps, the same as the previous, except that those atoms that have nearest neighbors other than the original 14 from the bcc structure are marked in white. This gives some indication of the amount of plastic deformation that has occurred, and hence of sources of irreversibility in the transition. Of course, the thickness of the laminate is now determined by the finite size of the simulation cell.

Although the chosen simulation shows most of the behavior observed in the other 20 simulations on similar cells, it is important to recognize that the nucleation is to some extent random. In some of the simulations the $\langle 111\rangle_{bcc} \rightarrow \langle 10\bar{1}0\rangle_{hcp}$ direction did not lie along the z axis. In others, only two strips of two variants were nucleated, and hence no coarsening was observed. The third variant did not appear in many of the simulations. This variety of behaviors gives us confidence that the nucleation phase is not dominated by finite-size or boundary-condition effects.

VIII. FINITE-SIZE EFFECTS

Previous atomistic-level molecular-dynamics work has not observed microstructure for the simple reason that the simulations are too small. The microstructure forms because the energy of forming twin boundaries is less than the strain energy of accommodating the hcp structure into the bcc cell.[26] Simple scaling laws show that for a simulation cell of length L, the energy associated with the twin boundary area grows as L^2, while the strain energy grows as L^3; consequently the microstructure becomes favored in a large system.

There are several similar finite-size considerations, and we explain here which features are affected by finite-size effects.

The appearance of regions of fcc is a finite-size effect, being due to a balance between high-energy asymmetric twin boundaries (L^2) and the energy difference between hcp and fcc (L^3). However, when the microstructure is very fine, in the early stages of growth, these fcc regions are genuinely stable. In the simulation they are eliminated not because of the scaling laws, but because the need for high-energy asymmetric twin boundaries in the microstructure is removed when the microstructure ripens to contain only two variants. In this sense, the temporary appearance of the fcc phase is expected to be a real phenomenon occurring early in the microstructural evolution, and not an artifact of the finite size of our system.

IX. CONCLUSIONS

A series of molecular-dynamics simulations that used a many-body potential have been carried out to describe the bcc-hcp transition in a model of zirconium. These calculations give insights into the atomic-level evolution of the microstructure during and shortly after the transition. By using a variety of simulation shapes and sizes, investigating both constant-volume and constant-pressure boundary conditions, and different quenching methods, we have demonstrated that the observed qualitative microstructural features are independent of the details of the simulation (except for finite-size effects).

A particular $\langle 111\rangle_{bcc}$ direction, apparently found randomly from the four possibilities, defines both the transfor-

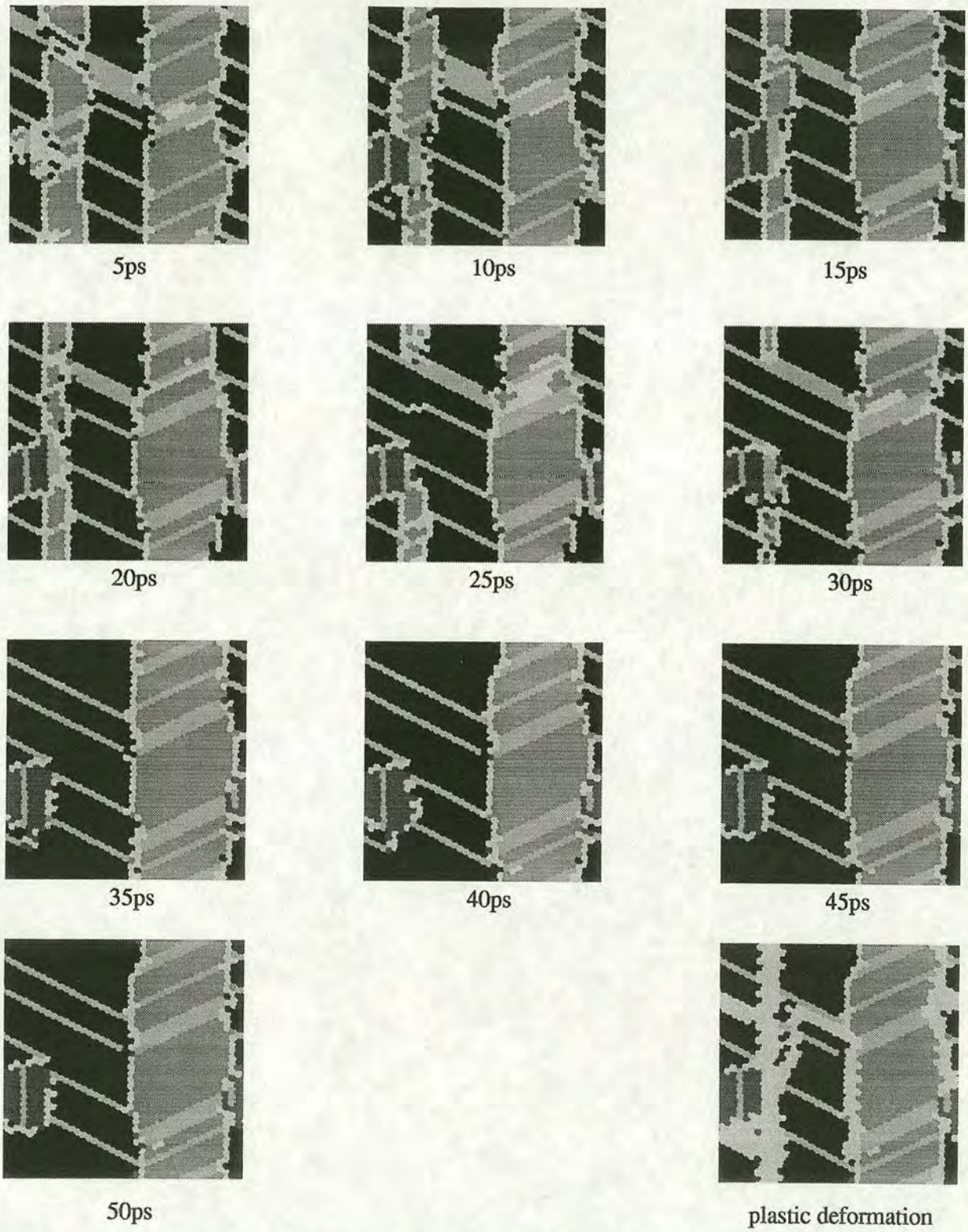

FIG. 3. Ten snapshots, taken at 5-ps intervals, of configurations quenched from the MD simulations. The black, dark gray, and mid-gray regions are hcp-coordinated variants, the light-gray regions are fcc (generally these are stacking faults) while the white are unclassifiable atoms (typically in the atomically sharp twin boundary). The final picture is from the same configuration as the tenth (50 ps), with atoms having different neighbors from their original bcc-coordination shell colored white. Further examples can be seen at http://www.ph.ed.ac.uk/may/works

mation plane (in practice, the interface between parent and martensite) and three possible hcp variants. The final microstructure involves twins comprising two variants of the hcp, i.e., $(10\bar{1}1)_{hcp}$ twins; this minimizes macroscopic strain of the crystal, and this is what is observed after some time. However, in the actual calculation we observe that a third variant is nucleated at the transition and subsequently destroyed. The microstructure also coarsens with time.

Some microscopically irreversible plastic deformation also occurs that is probably rapid motion of basal-plane partial dislocations leaving stacking faults as their signature. The driving force for this is the energy difference between the martensitic 60° incommensurate symmetric tilt twin boundaries and the 61.5° commensurate $(10\bar{1}1)_{hcp}$ twins. The effect of the dislocations is to rotate the twins, introducing microscopic irreversibility into the transformation.

This work introduces a criterion for microscopic irreversibility that may be of general relevance for creation of shape memory effect alloys, namely, the existence of metastable phases such as fcc, which may be stabilized by local strain or boundary energy considerations, and the existence of low-energy twin boundaries at angles close to, but not at, the angle dictated by the transition mechanism.

[1] Z. Nishiyama, *Martensitic Transformations* (Academic, New York, 1978).

[2] F. Willaime and C. Massobrio, Phys. Rev. B **43**, 11 653 (1991).

[3] Y.-Y. Ye, Y. Chen, K.-M. Ho, B.N. Harmon, and P.-A. Lindgård, Phys. Rev. Lett. **58**, 1769 (1987).

[4] P.-A. Lindgård and O.G. Mouritsen, Phys. Rev. Lett. **57**, 2458 (1986).

[5] T. Castán and P.-A. Lindgård, Phys. Rev. B **40**, 5069 (1989).

[6] A. Serra and D.J. Bacon, Mater. Sci. Forum **126-128**, 69 (1993).

[7] J.R. Morris, Y.-Y. Ye, K.-M. Ho, C.-T. Chan, and M.-H. Yoo, Philos. Mag. A **72**, 751 (1995).

[8] V.G. Kapinos, Y.N. Osetsky, and P.A. Platonov, J. Nucl. Mater. **195**, 83 (1992).

[9] A.G. Mikhin and Y.N. Osetsky, J. Phys.: Condens. Matter **5**, 9121 (1993).

[10] A.G. Mikhin, Y.N. Osetsky, and V.G. Kapinos, Philos. Mag. A **1**, 25 (1994).

[11] B.L. Zhang, C.Z. Wang, K.-M. Ho, D. Turner, and Y.-Y. Ye, Phys. Rev. Lett. **74**, 1375 (1995).

[12] P. Dang and M. Grujicic, Modell. Simul. Mater. Sci. Eng. **4**, 123 (1996).

[13] G.J. Ackland, Ph.D. thesis, Oxford University, 1987; M.W. Finnis, UKAEA Report No. AERE R13182, 1988 (unpublished).

[14] M.W. Finnis and J.F. Sinclair, Philos. Mag. A **50**, 45 (1984); **53**, 161 (1986).

[15] M.S. Daw and M.I. Baskes, Phys. Rev. B **29**, 6443 (1984).

[16] G.J. Ackland, S.J. Wooding, and D.J. Bacon, Philos. Mag. A **71**, 553 (1995).

[17] J.M. Ball and R.D. James, Z. Angew. Math. Mech. **76**, 389 (1996).

[18] J.M. Ball and R.D. James, Arch. Ration. Mech. Anal. **100**, 13 (1987).

[19] G.J. Ackland and U. Pinsook, in *Microscopic Simulation of Interfacial Phenomena in Solids and Liquids*, edited by S.R. Phillpot, P.D. Bristowe, D.G. Stroud, and J.R. Smith, MRS Symposia Proceedings No. 492 (Materials Research Society, Pittsburgh, 1998).

[20] G.J. Ackland, G.I. Tichy, V. Vitek, and M.W. Finnis, Philos. Mag. A **56**, 735 (1987).

[21] M.H. Yoo, Metall. Trans. A **12**, 409 (1981).

[22] J. Gavartin (private communication).

[23] S. Nose, J. Chem. Phys. **72**, 2384 (1984); W.G. Hoover, Phys. Rev. A **31**, 1695 (1985).

[24] M. Parrinello and A. Rahman, J. Appl. Phys. **52**, 7182 (1981).

[25] V. Vitek, G.J. Ackland, and J. Cserti, *Alloy Phase Stability and Design*, edited by G.M. Stocks, D.P. Pope, and A.F. Giamei, MRS Symposia Proceedings No. 186 (Materials Research Society, Pittsburgh, 1991), p. 237.

[26] We find that for any reasonable value of the fictitious box mass, the transition is too rapid for the Parrinello-Rahman MD box to change shape and thus accommodate the strain. This is consistent with the physical situation where the transition within a single grain is subject to the constraints imposed by surrounding grains.

ARTICLES

Calculation of anomalous phonons and the hcp-bcc phase transition in zirconium

U. Pinsook and G. J. Ackland
Department of Physics and Astronomy, The University of Edinburgh, Edinburgh, EH9 3JZ, Scotland, United Kingdom
(Received 13 January 1999)

Using molecular dynamics with a many-body potential fitted to properties of zirconium we study the behavior of phonons at high temperature in the bcc lattice; in particular, the T_{1N} mode which according to the Nishiyama-Wassermann mechanism is the cause of the martensitic transition to hcp in group-IV transition metals. This phonon frequency softens towards the transition but does not tend to zero frequency. In contrast to the fast kinetics of the bcc→hcp transition, the reverse process, i.e., hcp→bcc, is not observed in standard molecular dynamics: it can be induced if the T_{1N} phonon is perturbatively excited in the martensitic phase. The sluggishness of the reverse process is attributed to the fact that in the low-temperature hcp phase, the equivalent oscillation to T_{1N} involves two modes with different frequency. The bcc to hcp transition is a first-order transition and occurs in such a way that most of the reversed bcc atoms obey Nishiyama-Wassermann rules, i.e., the path of transformation is reversible. However, there is some plastic damage which is not recovered. [S0163-1829(99)10021-3]

I. INTRODUCTION

A martensitic transition is a structural phase transition which involves little movement of atoms during transformation. In group-IV transition metals, i.e., titanium, zirconium, and hafnium, a transition from body-centered-cubic to hexagonal-close-packed structure is observed on lowering the temperature. The atomistic mechanism for this transition has been described by the Nishiyama-Wassermann (NW) rules.[1–3] Zirconium is the best representative of the group for simulation purposes: unlike titanium, zirconium has no magnetic moment and the phase transition is purely mechanical.[4] The experimentally determined transition temperature T_0 is 1136 K.

The nature of the kinetics of this type of transition has been widely investigated. In 1947 Zener[5] studied β brass and proposed a soft-mode model for the stability of the bcc structure in which the shear modulus $\frac{1}{2}(C_{11}-C_{12})$ becomes lowered and approaches zero at the transition temperature. Below the transition temperature each unit cell in the lattice becomes mechanically unstable and a phase transition occurs. A similar model by Friedel concentrates on a particular short-wavelength phonon becoming unstable.[6] However, the mechanism is not always so simple: in general the phonon mode will have lower symmetry than the crystal and hence will couple to the macroscopic strain. In this case one of the single-crystal elastic constants will tend to zero at the transition, but there is no pure phonon instability. The phase transition occurs by a distortion involving both the phonon and the strain, which is in general accommodated by the formation of a microstructure.

The latter is the case in zirconium. According to the mechanism proposed by Nishiyama and Wassermann (NW), significant finite strain is required in addition to the T_{1N} phonon.

Using inelastic neutron scattering, the phonon dispersion curve of zirconium has been measured[7,8] and revised.[9,10] This shows that the T_{1N} phonon is softened a little toward the transition temperature with a slope of 0.0008 THz/K. Although the softening is consistent with the soft-mode model in which T_{1N} is the cause of the transition, this phonon has a finite frequency of about 1.08 THz at the transition temperature[9] implying a coupling with the strain. The neutron-measured phonon does not incorporate coupling to an infinite wavelength strain, this coupling explains the occurence of the transition prior to the T_{1N}-mode frequency going to zero.

Several theoretical models have been proposed in order to describe the experimental results. May, Müller, and Strauch[11] studied the vibrational properties of zirconium by using a Born-Mayer-type potential. They concluded that zirconium manifests line broadening, line shift, and interference which are the main features of a strong anharmonic system. *Ab initio* work by Ye *et al.*[12] employed the frozen phonon method and discovered that the modes along the salient phonon branch, i.e., Γ-N $\mathbf{k}=[\xi\xi 0]$, are strongly coupled. Willaime and Massobrio[13,14] derived a four-parameter embedded atom method (EAM) potential for zirconium: In harmonic and quasiharmonic regimes, the T_{1N} phonon becomes unstable, but using molecular dynamics they found that the phonon is dynamically stable and has a finite frequency at higher temperature. From the fact that the anharmonic effect is fully included via the interatomic potential, this result confirms that the anharmonic effect has an important role for stabilizing the bcc lattice.

From the thermodynamic point of view, theoretical approaches such as Landau-type theory, mean-field theory,[15] and self-consistent phonon theory[16,17] led to the same conclusion that the excess vibrational entropy stabilizes the high-temperature phase. This can be explained as follows: First, the T_{1N} phonon has a peculiar low frequency and thus

can be excited easily.[16,17] Consequently, the vibrational entropy of the system becomes large enough to stabilize the bcc structure. Second, at the transition temperature, the frequency of the phonon is still finite but magnitude of the fluctuation is decreasing and therefore its vibrational entropy is no longer sufficient to stabilize the bcc structure and the transition to hcp structure takes place. This is in a good agreement with the experimental results. The phonon density of states in a low-frequency region around 1.69 THz is lowered with decreasing temperature.[9] The argument of excess entropy stabilizing the high-temperature phase is also applied to the similar martensitic transition in NiAl alloys,[18] however, since the transition in zirconium occurs above the Debye temperature the phonon entropy argument should be treated with caution.

Based on these observations, Lindgård and Mouritsen[2,19] used strain components as order parameters in a Landau theory to study martensitic transition in zirconium. A similar method is applied by Gooding and Krumhansl[20] to study the bcc$\rightarrow 9R$ transition in Li. They used a corresponding phonon as an order parameter and combined the phonon with strain components. Both works show that the transition is first order and stacking faults can be formed as a metastable state.

Ab initio calculations have shown that the density of states at the Fermi energy in bcc is higher than in hcp.[4,21,22] It is therefore possible that the phase transition is due to excess electronic entropy. However, as we show here, and as is known from the electronic structure calculations, the effect of this high density of states is to destabilize the ideal bcc structure (i.e., all atoms on their lattice positions) used to calculate the density of states. Thus the density of states derived from this ideal structure may no longer be a good model for the high-pressure structure.

Despite this clear picture of how and why the bcc structure transforms into the hcp, there is no further study of the T_{1N} phonon mode in the low-temperature phase. It is suggested that the phonon mode might split into several modes in the hcp[23] and become much stiffer.[16,17] However, there is no systematic proof of this relation. Moreover, the role of T_{1N}-equivalent mode in hcp to the reverse transition remains unsolved.

In the present work, we use molecular dynamics to calculate the phonon properties of the bcc structure in zirconium using a many-body potential which is known to reproduce the phase transition via the NW mechanism.

Simulations in which the temperature is lowered through T_c are performed in order to allow the phase transition. The evolution of T_{1N} phonon is monitored. We attempt to raise the temperature to investigate the reverse transition, but in the limit of our finite-size molecular dynamics, the reversed process is not observed. Nevertheless, we can induce the hcp to bcc transition by exciting the T_{1N} equivalent mode in the martensitic microstructure.

Throughout this paper we use the term martensite microstructure to mean the twinned hcp microstructure which has been produced from the bcc phase via the phase transition. It is not a pure single crystal, but contains several hcp variants, twin boundaries, and some stacking faults[3] which one might expect to act as nucleation centers for the reverse transition. In Ref. 3 it was shown that the transformation path is not perfectly microscopically reversible in the sense that a minority of the atoms in the hcp structure have different neighbors than would be predicted from the NW mechanism, having moved relative distances of order of the lattice parameter. Although this microscopic irreversibility is at variance with the Nishiyama-Wassermann mechanism, the majority of the atoms were found to have the expected neighbors.

II. MOLECULAR DYNAMICS

In our simulations we use a Finnis-Sinclair-type potential[24] which has the form

$$E_i=\frac{1}{2}\sum_j V(r_{ij})-\sqrt{\sum_j \phi(r_{ij})}, \tag{1}$$

where $V(r_{ij})$ represents the pair repulsive energy, ϕ_i is a parameterized pairwise interaction representing the square of the tight-binding hopping integral, and its square root represents the cohesive energy of a partialy filled band in the assumption of local charge neutrality.[25] The cubic spline functional form is chosen for $V(r_{ij})$ and ϕ_i.[26] The potential was fitted to properties of the hcp structure only, namely the anisotropic elastic properties of zirconium, the 1.595 nonideal c/a ratio, the lattice parameter, vacancy formation, and cohesive energy of the hcp structure.[27] Although fitted only to the hcp phase, the potential is known to reproduce a good description of both bcc and hcp phases: in particular, the transition temperature observed by classical molecular dynamics at large system size lies between 1330 and 1390 K,[3] depending slightly on choice of boundary conditions and thermostats. Further details of the potential are discussed elsewhere.[27]

We solve Newton's equations of motion by using a molecular-dynamics code.[28,29] The integration scheme is a fourth-order Gear predictor-corrector algorithm. The time step is equal to 1 fs. Temperature is regulated by a Nose-Hoover[30–32] thermostat. The initial configuration is a homogeneous bcc lattice with the equilibrium value of the lattice parameter corresponding to the thermal expansion predicted by the potential at each temperature, as found by a preliminary series of constant pressure simulations. This variation of bcc lattice parameter with temperature is shown in Fig. 1. In all calculations, the unit cell is oriented along $(100)_{bcc}$, $(010)_{bcc}$, and $(001)_{bcc}$, unless otherwise stated.

III. NORMAL-MODE CALCULATION IN THE BCC PHASE

In order to study a particular vibrational mode in a crystal, we first define the eigenvector of that mode. To do this the displacements of atoms in solid are written in terms of a complete set of independent coordinates[33] as

$$\alpha_{\mathbf{k}}(t)=\sum_i [\mathbf{r}_i(t)-\mathbf{l}_i]\cdot \mathbf{e}_{\mathbf{k}} \cos(\mathbf{k}\cdot\mathbf{l}_i), \tag{2}$$

where $\mathbf{k}$ is a wave vector, $\mathbf{e}_{\mathbf{k}}$ is a corresponding eigenvector of the mode $\mathbf{k}$, $\mathbf{l}_i$ is a lattice vector, and $\mathbf{r}_i$ is the position of atom i. These coordinates are chosen to be the normal modes of the bcc crystal, with $\mathbf{e}_{\mathbf{k}}$ determined from a lattice-dynamics calculation at 0 K. Consequently, their vibrations are classical objects analogous to phonons (which are quan-

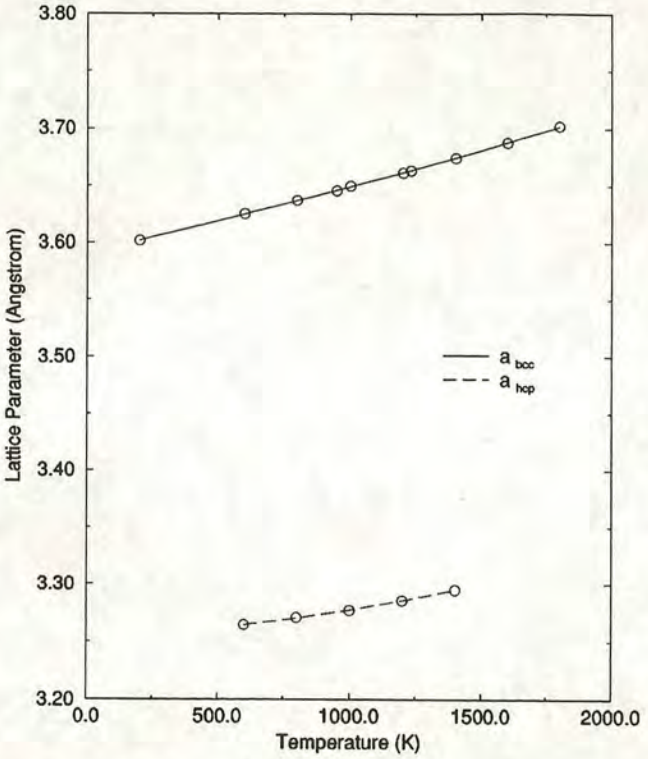

FIG. 1. Variation of the equilibrium bcc lattice parameter against temperature. Each point was calculated from a constant pressure molecular-dynamics calculation. Below the transition pressure the data is collected for a supercooled bcc phase which remains stable for a few ps.

tized) and with the same frequency, and can be compared directly to neutron-scattering data.

If the crystal were perfectly harmonic, the evolution of the normal coordinates could be written as

$$\alpha_{\mathbf{k}}(t)=A\cos(\omega_{\mathbf{k}}t+\varphi_{\mathbf{k}}), \tag{3}$$

where A is an amplitude, $\omega_{\mathbf{k}}$ is the frequency of the mode, and $\varphi_{\mathbf{k}}$ is a phase factor.

We define the autocorrelation function for this mode as $\langle\alpha_{\mathbf{k}}(t)\alpha_{\mathbf{k}}(0)\rangle$. In the harmonic case its Fourier transform is then simply a delta function at $\omega_{\mathbf{k}}$.

At high temperatures, anharmonic effects cause the evolution of the modes to depend on the excitation of other modes. Now the Fourier transform of the autocorrelation function will exhibit a peak at $\omega_{\mathbf{k}}$, broadened by these coupling effects. Moreover, if the mode itself is anharmonic, further broadening will occur and the peak position will be dependent on temperature.

Finally, if $e_{\mathbf{k}}$ is not a normal mode, the Fourier transform will consist of peaks at each of the normal modes of which $e_{\mathbf{k}}$ is comprised. For example, if we take $e_{\mathbf{k}}=1$, there will be a peak for each phonon with wave vector $\mathbf{k}$.

In the simulation box, there are only a certain number of wave vectors that are allowed due to the finite number of atoms. The possible wave vectors are given by integers n_k, n_l, and n_m such that

$$\mathbf{k}=\left(\frac{2\pi n_k}{a},\frac{2\pi n_k}{b},\frac{2\pi n_k}{c}\right), \tag{4}$$

TABLE I. $\mathbf{k}_1=[\xi\xi 2\xi]$.

ξ	T_1	T_2	L
0.0625	0.52	0.86	1.86
0.1250	1.06	1.75	3.50
0.1875	1.56	2.84	4.57
0.2500	1.57	3.86	5.17
0.3125	1.91	4.49	4.79
0.3750	1.79	5.09	4.21
0.4375	1.20	5.40	3.60
0.5000	0.53	5.51	3.33

where a, b, and c are the lengths of the axes of the orthorhombic simulation cell. The maximum allowed value of n_k, n_l, and n_m is determined by the number of bcc primitive unit cells along each axis.

Thus once the vibrations of the structure are projected onto these normal modes, it is straightforward to extract the frequency of a specific phonon at a particular temperature by Fourier transforming the ensemble-averaged position $\langle\alpha_{\mathbf{k}}(0)\cdot\alpha_{\mathbf{k}}(t)\rangle$ or velocity $\langle\dot{\alpha}_{\mathbf{k}}(0)\cdot\dot{\alpha}_{\mathbf{k}}(t)\rangle$ autocorrelation function. We will use this method to determine the finite-T phonon dispersion relation from our molecular-dynamics (MD) simulation.

A difficulty arises when a harmonic mode basis is applied to study a strongly anharmonic system because vibrations of the normal-mode coordinates are no longer independent: in quantum language the phonons are scattered. However, in the present case we found it was always possible to unambiguously identify the peaks in the Fourier transform.

An alternative approach led Dickey and Paskin[33] to introduce a perturbative normal-mode calculation in which a phonon is artificially excited at a particular time. The perturbation is defined as

$$\mathbf{r}_i'(t)=\mathbf{r}_i(t)+\epsilon\cos(\mathbf{k}\cdot\mathbf{l}_i)\mathbf{e}_{\mathbf{k}}, \tag{5}$$

where $\mathbf{r}'$ and $\mathbf{r}$ are perturbed and unperturbed atomic position, respectively. The advantages of this method are that both the phonon frequency and its lifetime can be calculated within a short simulation period. This is because the additional energy of the perturbed mode is dispersed into other modes soon after the perturbation. However, when Willaime and Massobrio[13,14] used this method to study T_{1N} phonon in the bcc structure they found that the frequency of the phonon is dependent on the strength of the perturbation ϵ, showing that the phonon itself is strongly anharmonic.

Since our calculations are designed to study very anharmonic phonons, we avoid all these difficulties and ensure the statistical reliability by calculating phonon frequencies direct from the time evolution of normal-mode coordinates from a long simulation, i.e., 40 ps and averaging over six samples. We will adopt the perturbative approach later when considering the reverse transition from hcp to bcc.

Thus we construct the finite temperature phonon dispersion curve. We simulate 8192 bcc atoms at 1400 K and present the phonon-dispersion relation along four branches which are $\mathbf{k}_1=[\xi\xi 2\xi]$, $\mathbf{k}_2=[\xi\xi 0]$, $\mathbf{k}_3=[00\xi]$, and $\mathbf{k}_4=[\xi\xi\xi]$. The results are shown in Tables I–IV and compared with the experimental[9] data for zirconium in Fig. 2.

TABLE II. $\mathbf{k}_2=[\xi\xi 0]$.

ξ	T_1	T_2	L
0.0625	0.08	1.06	0.58
0.1250	0.16	2.10	1.16
0.1875	0.32	3.14	1.69
0.2500	0.40	3.92	2.18
0.3125	0.49	4.66	2.71
0.3750	0.59	5.12	3.02
0.4375	0.56	5.38	3.19
0.5000	0.53	5.51	3.33

The results are generally in good agreement with the experiment: since the potential was not fitted to any properties of this bcc structure this gives us confidence to proceed. The only discrepancy is in the value of the Γ-N branch phonons which are somewhat lower than experiment. This is consistent with the fact that the phase-transition temperature for the potential is higher than for real zirconium.

It is also possible to obtain phonon-dispersion relations by lattice dynamics.[34] Force constants and dynamical matrix elements can be obtained analytically from doubly differentiating the potential which introduces slight complications due to its many-body nature.[35] Unlike experiment and MD, which measure correlation functions, lattice dynamics directly measures the harmonic term in the potential-energy surface: no anharmonic effects are incorporated, although in the quasiharmonic approach the lattice dynamics is performed at different lattice parameters according to the temperature.

Lattice dynamics results for the current potential at a bcc lattice parameter of 3.67 Å (corresponding to 1400 K) are plotted in Fig. 1. Again, good agreement with both experiment and MD can be seen with the dramatic exception of the T_{1N} branch, where the harmonic phonon frequency is imaginary—i.e., the expanded bcc lattice is unstable with respect to this distortion.

The failure of the lattice dynamics calculation to reproduce the experimentally observed behavior provides dramatic evidence for the importance of anharmonicity in the system. Moreover, it explains why the visualization method used in Ref. 3—quenching the structure to 0 K and examining the neighbors of each atom—never gives any bcc-coordinated atoms.

A further failing of the quasiharmonic approach is that it predicts that the T_{1N} phonon becomes stiffer with reduced volume (i.e., reduced temperature). Indeed, it is actually stable at the zero-temperature equilibrium volume for (metastable) bcc zirconium. This suggests that the high-pressure bcc phase in the zirconium phase diagram has a quite different character from the dynamically stabilized high-T bcc phase.

TABLE III. $\mathbf{k}_3=[00\xi]$.

ξ	T	L
0.1250	0.85	1.25
0.2500	1.69	2.46
0.3750	2.64	3.39
0.5000	3.43	4.13
0.6250	4.13	4.53
0.7500	4.49	4.65
0.8750	4.72	4.84
1.0000	4.76	4.76

TABLE IV. $\mathbf{k}_4=[\xi\xi\xi]$.

ξ	T	L
0.1250	0.86	2.63
0.2500	1.97	4.43
0.3750	3.23	5.00
0.5000	4.26	4.26
0.6250	4.38	2.18
0.6666	4.60	1.79
0.7500	4.80	2.34
0.8750	5.03	4.07
1.0000	4.76	4.76

The frequency of T_{1N} phonon is calculated by MD in constant volume and constant temperature mode at 1400, 1600, and 1800 K as shown in Fig. 3. The slope is 0.0003 THz/K.

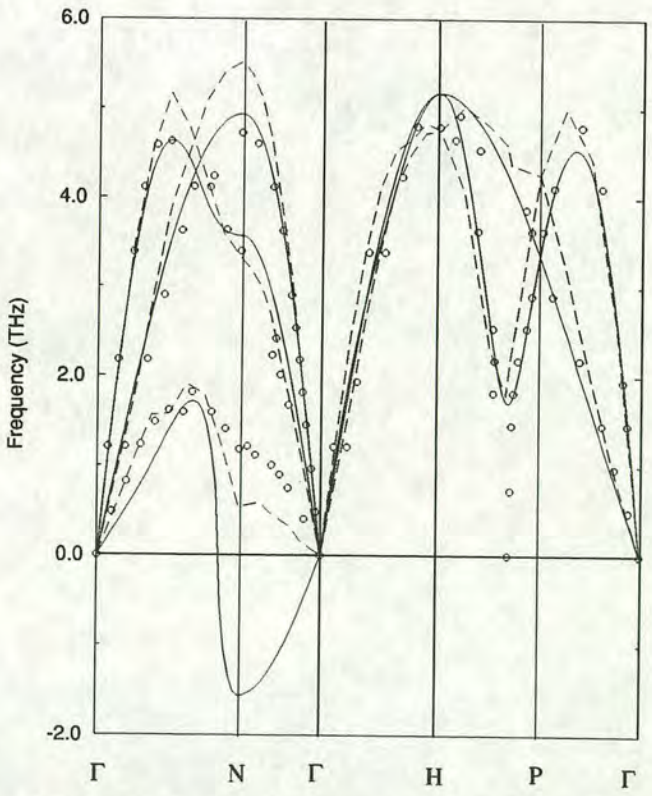

FIG. 2. Phonon dispersion curve at $T=1400$ K. Dashed lines are the results of the MD calculation as described in the text. Circles are experimental results taken from Ref. 9. Solid lines represent quasiharmonic lattice-dynamics calculations for perfect bcc at the volume implied by the MD thermal expansion in Fig. 1. Imaginary frequencies corresponding to unstable phonons are shown as negative.

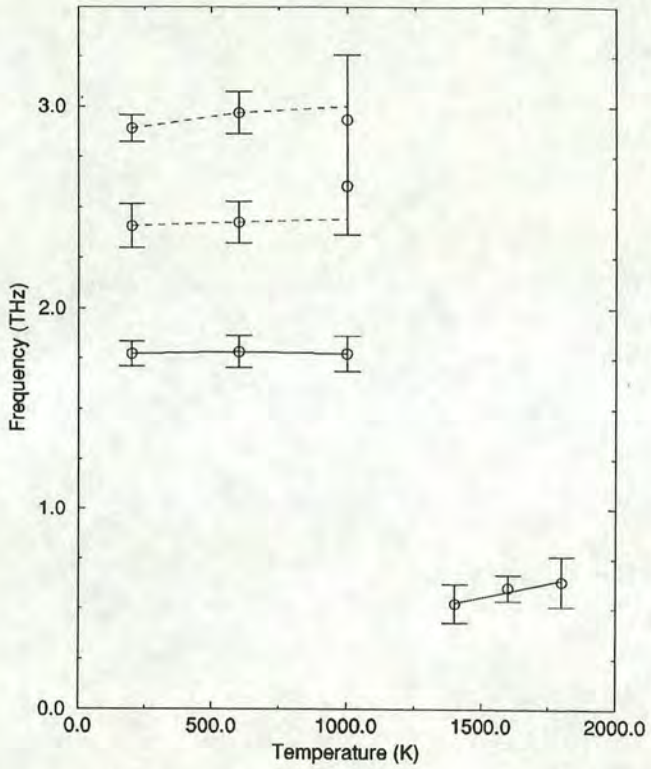

FIG. 3. Temperature dependence of T_{1N} phonon in the bcc phase at $T>1390$ K and the peaks of the Fourier transform for the equivalent mode in the hcp phase at $T<1390$ K. Each point is taken from an average over several MD runs, and the error bars reflect the spread of the results. At 1000 K for some microstructures it proved impossible to distinguish between the two highest frequency peaks.

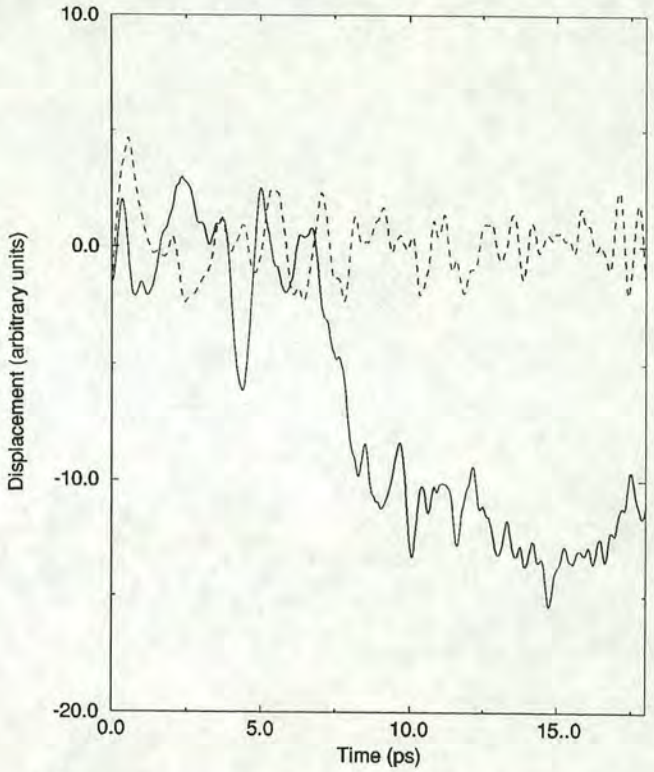

FIG. 4. Time evolution of the α_N coordinate following rapid cooling from 1400–1000 K, showing large fluctuations in the unstable bcc phase, followed by a discrete shift of the mean at the phase transition and subsequent stable oscillations in the hcp phase.

IV. THE "T_{1N} MODE" IN THE HCP STRUCTURE

When the system undergoes a phase transition to the low-temperature hcp structure, there are six possible martensitic variants which could occur, each corresponding to an NW transition involving a particular T_{1N} mode.[36] In practice, a subset of three of these are selected, depending on the specific martensite growth plane, and a strain compensating microstructure involving these three hcp variants is formed.[3]

While taking the material through its phase transition, we have continued to evaluate the time evolution the coordinate $\alpha_N(t)$, which corresponds to the T_{1N} mode. According to the NW mechanism, within a single variant, one of the sets of $[011]_{bcc}$ planes becomes the basal planes in hcp, four become pyramidal planes, and one becomes prism planes.

Figure 4 shows typical plots of the $\alpha_N(t)$ associated with the operative NW mechanism through the phase transition. In the bcc phase, the fluctuation of those planes is (by construction) around zero displacement $\int \alpha_N(t)dt=0$. After the transition, the fluctuation is displaced away from zero point indicating the structural change. This shows that in spite of the appearance of microstructure $\langle \alpha_N(t) \rangle$ is a good order parameter for the transition.

When the system reached an equilibrium in the martensite phase, the T_{1N} "phonon" is projected out at 200, 600, and 1000 K. To investigate the T_{1N}-equivalent mode in the hcp phase we continue to follow the fluctuation and displacement of the coordinate α_N. After the transition we took a Fourier transform of the $\alpha_N(t)$ autocorrelation function in the hcp phase. The data is rather noisy, so we have applied a maximum entropy procedure across various runs which enables us to distinguish the peaks corresponding to the hcp phonons which make up $\alpha_N(t)$.

The discrete Fourier transforms of the time evolution of $\langle \alpha_N(t) \rangle$ in the hcp phase are shown Figs. 5 and 6, together with the maximum entropy smoothing and the actual data in the insets.

For three of the modes (typified by Fig. 5) we find that the time averaged $\langle \alpha_N(t) \rangle$ changes from zero to a finite value at the transition. This value is related to the amount of each variant in the resulting microstructure, but not in a straightforward way because both positive and negative $\alpha_N(t)$ give rise to equivalent hcp variants. For the α_N involved in the transition there is a large peak centered on zero corresponding to the slow evolution of the microstructure and the coupling of the mode to the strain. There are also two distinct peaks at relatively low frequency, showing that the coordinate α_N no longer represents a normal mode.

A typical example of one of the three T_{1N} modes which are related to variants which do not appear in the microstructure is shown in Fig. 6. This has has a time-averaged value of $\int \alpha_k(t)dt=0$ and shows two peaks in the smoothed Fourier transform. This indicates that there is no normal mode in the hcp which is equivalent to the mode in bcc which is responsible for the transition.

Figure 3 shows frequencies of these modes evaluated at different temperatures. Unlike the T_{1N} mode in bcc no clear temperature dependence can readily be determined.

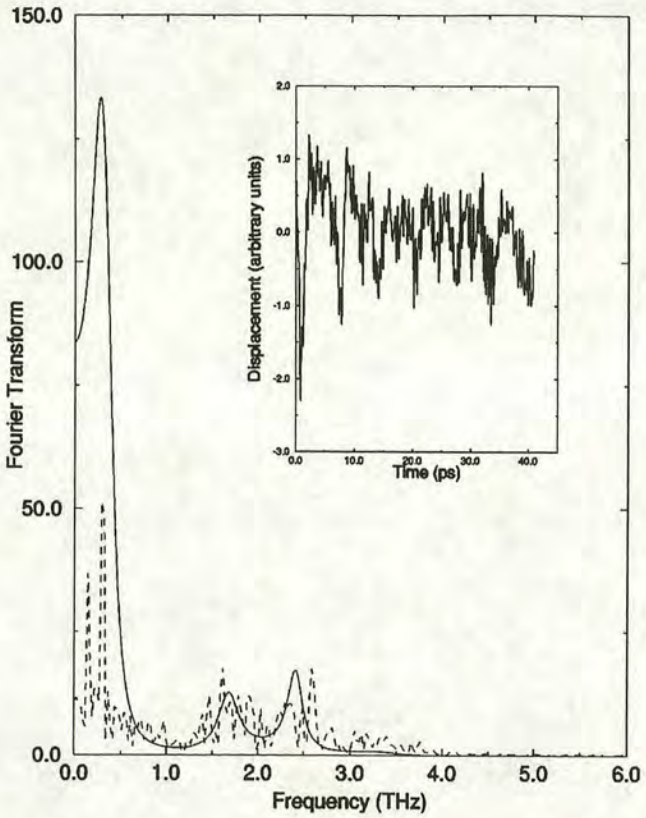

FIG. 5. Typical time evolution of the α_N coordinate for a T_{1N} mode in the hcp phase which is involved in the transition via the NW mechanism following rapid cooling from 1400–1000 K. The main figure shows the discrete Fourier transform of the data (dotted line) and the result of a maximum entropy smoothing of this data (solid line), while the inset shows the data $\alpha_N(t)$ itself from which a constant is subtracted to make the mean value zero prior to taking the Fourier transform.

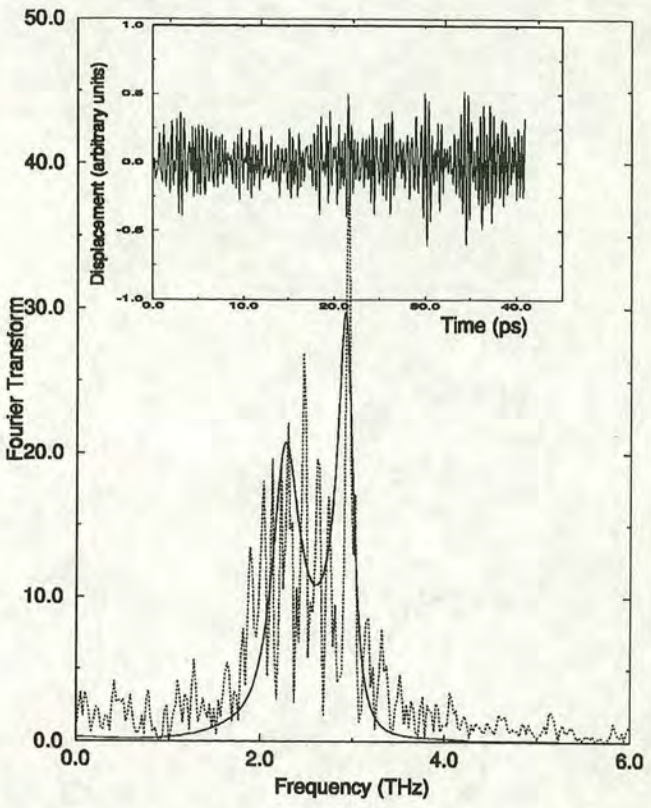

FIG. 6. Typical time evolution of the α_N coordinate for a T_{1N} mode which is not involved in the transition following rapid cooling from 1400–1000 K. The main figure shows the discrete Fourier transform of the data (dotted line) and the result of a maximum entropy smoothing of this data (solid line), while the inset shows the data $\alpha_N(t)$ itself.

V. THE REVERSE PHASE TRANSITION, HCP-BCC

To investigate the hcp-bcc transition we carried out a series of simulations comprising up to 75 000 atoms, initially in the pure hcp structure or the martensitic hcp microstructure. Simulations lasted 50 ps and involved heating to temperatures between the transition temperature and the point at which the crystal melts. Twenty calculations were performed at varying final temperatures and starting conditions. The hcp to bcc transition has not been observed at any temperature, no matter how hcp structure is defined, i.e., pure hcp or martensite microstructure.

The possible explanation is that the T_{1N} phonon splits into two or three normal modes in the hcp phase with different frequencies. Furthermore, it becomes stiffer as discussed in the last section. Thus to obtain the bcc phase via the reverse Nishiyama-Wassermann mechanism, the transition dynamics require simultaneous coherent fluctuation from several normal modes, rather than one. Since the normal modes have different frequencies, the required vibrations cannot remain in phase and the phonon-driven transition mechanism cannot function. In fact, even if the normal modes had the same frequency, the fact that the excited eigenvector, a linear combination of the degenerate eigenvectors, may not be exactly the right combination to cause the transition.

The above reasoning does suggest that if we can artificially stimulate the vibration corresponding to the T_{1N} phonon, and if the stimulation is strong enough, it might be possible to induce the hcp to bcc transition. To prove this, we impose the perturbation scheme defined by Eq. (5) to excite the T_{1N} phonon in the martensitic phase and perform the simulation at 1400 K where the bcc phase is stable. We use the martensitic hcp phase because we know exactly which $\mathbf{e_N}$ eigenvector corresponds to the T_{1N} phonon which was involved in the transition. We found that the strength of perturbation ϵ required to induce the hcp to bcc transition is 5.7% of the lattice parameter.

The eigenvector $\mathbf{e_N}$ is common to the entire Γ-N branch and so we tried exciting a phonon at $\mathbf{k}=0.56\mathbf{k_N}$ to see if it could induce the transition. Again this was successful, although the size of perturbation required was much larger, 28.3% of the lattice parameter.[37]

It is interesting that this is sufficient to induce the hcp to bcc process, because in the previous work,[13,14] perturbation strengths of up to 8.5% of the lattice parameter were used to study the T_{1N} phonon frequency.

The question of whether the high-temperature structure is bcc or hcp structures can be addressed in a number of ways. One is to consider thermodynamic properties of the whole system, the difference in cohesive energy is 0.03 eV/atom, the difference in volume is 0.6 Å^3/atom. In constant volume simulation, the stress tensor will change. In constant stress, the box components will change. All these features are in-

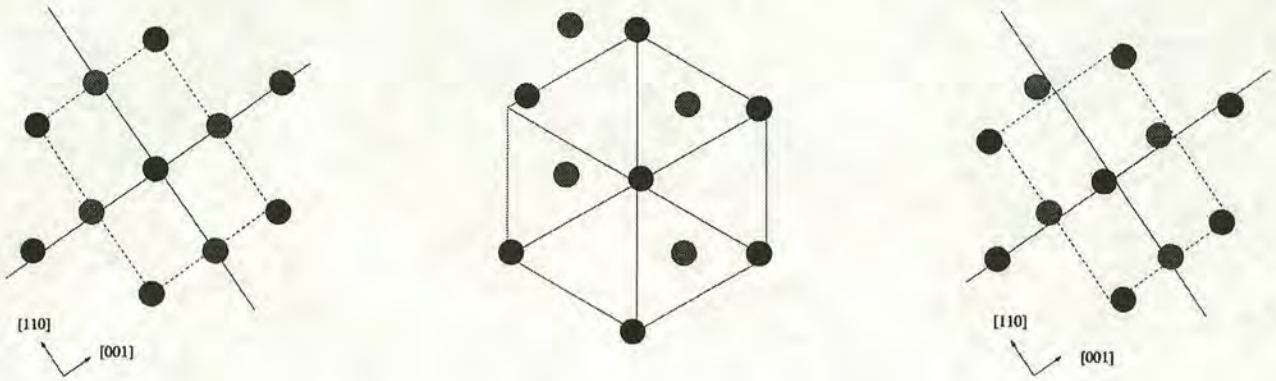

FIG. 7. Atomic pictures taken from a typical simulation of the bcc to hcp and the hcp to bcc transition. (a) Initial bcc structure; (b) microstructure after the martensitic transition; (c) induced bcc phase. Notice that it has some thermal fluctuation. Black and grey circles label different layers.

dicative of the phase under observation, and their discontinuous change suggests the phase transition, but the most important tools are the radial distribution function, the nearest-neighbor angular distribution function, and the assignment of a local crystal structure to each atom by fitting a template to a snapshot of its local environment.[3] Figure 7 shows typical local ordering of a few atoms through the complete bcc $\rightarrow$martensite$\rightarrow$bcc phase transition cycle. In Fig. 8 this cycle is further studied by quenching configurations to zero kelvin and measuring the "local crystal structure" of each atom. Figure 8(a) shows the perfect bcc lattice used as a starting condition. Figure 8(b) shows the characteristic strain-compensating hcp microstructure, while Fig. 8(c) shows that the induced bcc phase contains predominantly bcc atoms but that significant numbers now have locally hcp-type order.

VI. CONCLUSIONS

We have used molecular-dynamics simulation to study the properties of the phonons in the high-temperature bcc-phase of zirconium. The high-temperature phonon dispersion relation in the bcc lattice is established and it is in a good agreement with the experimental results. The frequency of the T_{1N} phonon is 0.53 THz at 1400 K with a temperature dependence of 0.0003 THz/K. Quasiharmonic lattice dynamics is shown to be inadequate to describe this phonon, predicting it to be unstable at the volume of the simulation. Lattice dynamics does show that the phonon becomes stable as the volume is reduced. This indicates that while the high-temperature bcc phase is dynamically stabilized by anharmonic effects against the T_{1N} mechanical instability, the high-pressure bcc phase is likely to be a conventional harmonic crystal. It would be interesting to investigate zirconium at simultaneous high temperature and pressure to see whether an isostructural transition exists between these two phases.

Although the phonon softens toward the transition, its frequency does not go to zero. Thus the transition is first order and must be nucleated by a large fluctuation in the phonon amplitude, together with a coupling to the strain. Of course,

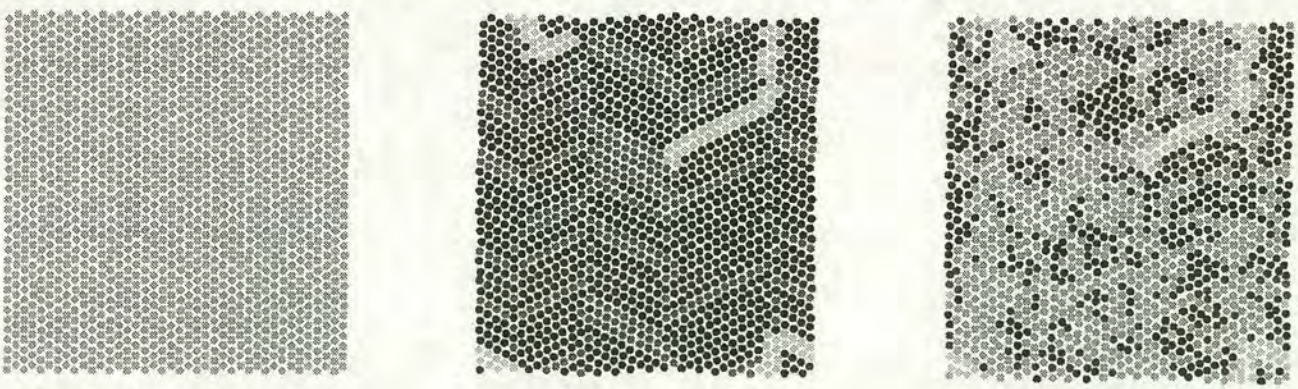

FIG. 8. Snapshots of a slice through the simulation cell showing the transformation from bcc to hcp by cooling, and the reverse transition by heating and excitation of the approprite vibrational mode. The coloring of the atoms is determined by fitting a template of the nearest-neighbor shell expected for bcc, fcc, or hcp to each atom. The atoms are then shaded as follows: black atoms have local hcp coordination with neighbors as expected from the NW transition mechanism; dark grey atoms have local fcc coordination; mid grey atoms have bcc coordination while light grey atoms have a different set of neighbors from their original 14, indicating irreversible plastic deformation. (a) Initial bcc; (b) martensitic hcp; (c) induced bcc.

it is the compensation for this strain which gives rise to the martensitic microstructure.

We have continued to study the fluctuation of atomic planes that used to be the T_{1N} phonon after the phase transition to a martensitic hcp occurs at around 1350 K. It is no longer a pure phonon mode. This means that the reverse Nishiyama-Wassermann mechanism cannot operate by phonon fluctuations since it would require two phonons to be excited simultaneously and coherently. Statistically, this is a far less likely scenario than the single mode excitation required for transition from bcc, and consequently we observe that the reverse transition can only occur (on the time scale of our simulations) if such a simultaneous, phonon excitation is induced artificially. We believe that this may be a rather general result in a wide class of martensitic transitions, and may explain, for example, the different mechanisms observed for the forward and back transitions in iron where it has been reported that the fcc-bcc transition occurs via the Bain deformation while the reverse bcc-fcc transition follows the Burgers path.[38]

ACKNOWLEDGMENTS

This work was supported by the EPSRC and the Royal Thai government through the IPST.

[1] Z. Nishiyama, *Martensitic Transformations* (Academic Press, New York, 1978).
[2] P.-A. Lindgård and O. G. Mouritsen, Phys. Rev. Lett. **57**, 2458 (1986).
[3] U. Pinsook and G. J. Ackland, Phys. Rev. B **58**, 11 252 (1998).
[4] R. Ahuja, J. M. Wills, B. Johansson, and O. Eriksson, Phys. Rev. B **48**, 16 269 (1993).
[5] C. Zener, Phys. Rev. **71**, 846 (1947).
[6] J. Friedel, J. Phys. (Paris) **35**, L59 (1974).
[7] C. Stassis, J. Zarestky, and N. Wakabayashi, Phys. Rev. Lett. **41**, 1726 (1978).
[8] C. Stassis and J. Zarestky, Solid State Commun. **52**, 9 (1984).
[9] A. Heiming, W. Petry, J. Trampenau, M. Alba, C. Herzig, H. R. Schöber, and G. Vogl, Phys. Rev. B **43**, 10 948 (1991).
[10] O. Dubos, W. Petry, J. Neuhaus, and B. Hennion, Eur. Phys. J. B **3**, 447 (1998).
[11] T. May, W. Müller, and D. Strauch, Phys. Rev. B **57**, 5758 (1998).
[12] Y.-Y. Ye, Y. Chen, K.-M. Ho, B. N. Harmon, and P.-A. Lindgård, Phys. Rev. Lett. **58**, 1769 (1987).
[13] F. Willaime and C. Massobrio, Phys. Rev. Lett. **63**, 2244 (1989).
[14] F. Willaime and C. Massobrio, Phys. Rev. B **43**, 11 653 (1991).
[15] W. C. Kerr and M. J. Rave, Phys. Rev. B **48**, 16 234 (1993).
[16] J. R. Morris and R. J. Gooding, Phys. Rev. B **43**, 6057 (1991).
[17] J. R. Morris and R. J. Gooding, Phys. Rev. B **46**, 8733 (1992).
[18] S. Rubini and P. Ballone, Phys. Rev. B **48**, 99 (1993).
[19] P.-A. Lindgård and O. G. Mouritsen, Phys. Rev. B **41**, 688 (1990).
[20] R. J. Gooding and J. A. Krumhansl, Phys. Rev. B **38**, 1695 (1988).
[21] P. J. Craievich, J. M. Sanchez, R. E. Watson, and M. Weinert, Phys. Rev. B **55**, 787 (1997).
[22] E. G. Moroni, G. Grimvall, and T. Jarlborg, Phys. Rev. Lett. **76**, 2758 (1996).
[23] J. Gavartin (private communication).
[24] M. W. Finnis and J. F. Sinclair, Philos. Mag. A **50**, 45 (1984); **53**, 161 (1986).
[25] G. J. Ackland, M. W. Finnis, and V. Vitek, J. Phys. F **18**, L153 (1988).
[26] G. J. Ackland, G. I. Tichy, V. Vitek, and M. W. Finnis, Philos. Mag. A **56**, 735 (1987).
[27] G. J. Ackland, S. J. Wooding, and D. J. Bacon, Philos. Mag. A **71**, 553 (1995).
[28] G. J. Ackland, Ph.D. thesis, Oxford University, 1987.
[29] M. W. Finnis, UKAEA Report No. AERE R13182, 1988 (unpublished).
[30] S. Nosé, Mol. Phys. **50**, 255 (1984).
[31] S. Nosé, J. Chem. Phys. **81**, 511 (1984).
[32] W. G. Hoover, Phys. Rev. A **31**, 1695 (1985).
[33] J. M. Dickey and A. Paskin, Phys. Rev. **188**, 1407 (1969).
[34] M. Born and K. Huang, *Dynamical Theory of Crystal Lattices* (Oxford University Press, London, 1956).
[35] G. J. Ackland, in *Alloy Modeling and Design* (TMS93 proceedings), edited by G. M. Stocks and P. E. A. Turchi (TMS, The Minerals, Metals and Materials Society, Warrendale, PA, 1993), p. 149.
[36] There are 12 symmetrically equivalent N points in the bcc Brillouin zone, but because of inversion symmetry these give rise to only six inequivalent martensitic variants.
[37] At 1400 K the bcc structure remains stable for only a few picoseconds before returning to hcp. The reason for this is unclear: it is possible that the strain on the unit cell is unable to relax quickly enough to fully stabilize the bcc. The microstructure of the recovered hcp is the same as the starting martensite configuration, indicating that the structure has retained some memory of its previous structure.
[38] Y. N. Osetsky and A. Serra, Phys. Rev. B **57**, 755 (1998).

Bibliography

[1] Z.Nishiyama, *Martensitic transformations*, (Academic, New York, 1978).

[2] A.L.Roytburd, *J. Phys. (France) IV* **C8**, 21 (1995).

[3] P.Haasen, editor, *Phase Transformations in Materials*, volume 5 of *Materials Science and Technology: a comprehensive treatment*, (VCH, New York, 1996), p.343-404.

[4] K.H.Matucha, editor, *Structure and Properties of Nonferrous Alloys*, volume 8 of *Materials Science and Technology: a comprehensive treatment*, (VCH, New York, 1996), p.399-468.

[5] J.Emsley, *The Elements*, 3rd ed., (Clarendon Press, Oxford, 1998), p232-233.

[6] R.Ahuja, J.M.Wills, B.Johansson and O.Eriksson, *Phys. Rev. B* **48**, 16269 (1993).

[7] A.Heiming, W.Petry, J.Trampenau, M.Alba, C.Herzig, H.R.Schöber and G.Vogl, *Phys. Rev. B* **43**, 10948 (1991).

[8] P.Haasen, *Physical Metallurgy*, 3rd ed., (Cambridge University Press, Cambridge, 1996), p.327-352.

[9] C.Zener, *Phys. Rev.* **71**, 846 (1947).

[10] C.Stassis, J.Zarestky and N.Wakabayashi, *Phys. Rev. Lett.* **41**, 1726 (1978).

[11] C.Stassis and J.Zarestky, *Solid State Commun.* **52**, 9 (1984).

[12] T.May, W.Müller and D.Strauch, *Phys. Rev. B* **57**, 5758 (1998).

[13] Y.-Y.Ye, Y.Chen, K.-M.Ho, B.N.Harmon and P.-A.Lindgård, *Phys. Rev. Lett.* **58**, 1769 (1987).

[14] F.Willaime and C.Massobrio, *Phys. Rev. B* **43**, 11653 (1991).

[15] W.C.Kerr and M.J.Rave, *Phys. Rev. B* **48**, 16234 (1993).

[16] J.R.Morris and R.J.Gooding, *Phys. Rev. B* **43**, 6057 (1991).

[17] J.R.Morris and R.J.Gooding, *Phys. Rev. B* **46**, 8733 (1992).

[18] P.J.Craivich, J.M.Sanchez, R.E.Watson, and M.Weinert, *Phys. Rev. B* **55**, 787 (1997).

[19] E.G.Moroni, G.Grimvall and T.Jarlborg, *Phys. Rev. Lett.* **76**, 2758 (1996).

[20] A.Y.Liu, A.A.Quong, J.K.Freericks, E.J.Nicol and E.C.Jones, *Phys. Rev. B* **59**, 4028 (1999).

[21] S.Rubini and P.Ballone, *Phys. Rev. B* **48**, 99 (1993).

[22] F.M.Wang and R.Ingalls, *Phys. Rev. B* **57**, 5647 (1998).

[23] W.G.Burgers, *Physica* **1**, 561 (1934).

[24] P.-A.Lindgård and O.G.Mouritsen, *Phys. Rev. Lett.* **57**, 2458 (1986).

[25] U.Pinsook and G.J.Ackland, *Phys. Rev. B* **58**, 11252 (1998).

[26] J.Crépin, T.Bretheau and D.Caldemaison, *Acta Metall. Mater.* **43**, 3709 (1995).

[27] A.V.Dobromyslov and N.I.Taluts, *Fiz. Metall. I Metallov.* **67**, 1138 (1989).

[28] J.P.Langeron and P.Lehr, *Mem. Scient. Revue Metall. LVI* **3**, 307 (1959).

[29] R.A.Holt, *J. Nucl. Mater.* **35**, 322 (1970).

[30] S.G.Song and G.T.Gray III, *Acta Metall. Mater.* **43**, 2339 (1995).

[31] P.-A.Lindgård and O.G.Mouritsen, *Phys. Rev. B* **41**, 688 (1990).

[32] R.J.Gooding and J.A.Krumhansl, *Phys. Rev. B* **38**, 1695 (1988).

[33] T.Castán and P.-A.Lindgård, *Phys. Rev. B* **40**, 5069 (1989).

[34] P.Dang and M.Grujicic, *Modeling Simul. Mater. Sci. Eng.* **4**, 123 (1996).

[35] H.Numakura, Y.Minonishi and M.Koiwa, *Phil. Mag. A* **63**, 1077 (1991).

[36] M.H.Yoo, *Metall. Trans. A* **12**, 409 (1981).

[37] A.M.Garde, E.Aigeltinger and R.E.Reed-Hill, *Metall. Trans.* **4**, 2461 (1973).

[38] A.Serra and D.J.Bacon, *Mater. Sci. Forum* **126-128**, 69 (1993).

[39] N.E.Paton and W.A.Backofen, *Metall. Trans. A* **1**, 2839 (1970).

[40] P.Mohn, K.Schwarz and P.Blaha, *J. Phys.: condens. matter* **8**, 817 (1996).

[41] Y.N.Osetsky and A.Serra *Phys. Rev. B* **57**, 755 (1998).

[42] J.Gui, Y.Cui, S.Xu, Q.Wang, Y.Ye, M.Xiang and R.Wang, *J. Phys.: condens. matter.* **6**, 4601 (1994).

[43] J.R.Morris, Y.-Y.Ye, K.-M.Ho, C.-T.Chan and M.-H.Yoo, *Phil. Mag. A* **72**, 751 (1995).

[44] R.C.Pond, D.J.Bacon and A.Serra, *Phil. Mag. Lett.* **71**, 275 (1995).

[45] A.G.Mikhin and Y.N.Osetsky, *J. Phys.: condens. matter* **5**, 9121 (1993).

[46] A.G.Mikhin, Y.N.Osetsky, and V.G.Kapinos, *Phil. Mag. A* **1**, 25 (1994).

[47] G.J.Ackland and U.Pinsook, *MRS Symp. Proc.* **492**, S7.7 (1997).

[48] U.Pinsook and G.J.Ackland, *Phys. Rev. B* **59**, 13642 (1999).

[49] J.M.Ziman, editor, *Electrons*, volume 1 of *Physics of Metals*, (Pergamon, London, 1969).

[50] A.P.Sutton, *Electronic Structure of Materials*, (Clarendon Press, Oxford, 1993), p.172-193.

[51] C.S.Nichols, *Structure and Bonding in Condensed Matter*, (Cambridge University Press, Cambridge, 1995), p.246-255.

[52] M.W.Finnis and J.F.Sinclair, *Phil. Mag. A* **50**, 45 (1984).

[53] M.W.Finnis and J.F.Sinclair, *Phil. Mag. A* **53**, 161 (1986).

[54] G.J.Ackland, D.Phil thesis, Oxford University (1987):
M.W.Finnis, UKAEA Report AERE R13182 (1988).

[55] G.J.Ackland, G.I.Tichy, V.Vitek, and M.W.Finnis, *Phil. Mag. A* **56**, 735 (1987).

[56] G.J.Ackland, *Phil. Mag. A* **66**, 917 (1992).

[57] G.J.Ackland, S.J.Wooding and D.J.Bacon, *Phil. Mag. A* **71**, 553 (1995).

[58] M.P.Allen and D.J.Tildesley, *Computer Simulation of Liquids*, (Clarendon Press, Oxford, 1987).

[59] H.Goldstein, *Classical Mechanics*, 2nd ed., (Addison-Wesley, Reading, Mass. Wokingham, 1980).

[60] S.Nosé, *Mol. Phys.* **50**, 255 (1984).

[61] S.Nosé, *J. Chem. Phys.* **81**, 511 (1984).

[62] W.G.Hoover, *Phys. Rev. A* **31**, 1695 (1985).

[63] H.C.Andersen, *J.Chem.Phys.* **71**, 4974 (1979).

[64] M.Parrinello and A.Rahman, *J. Appl. Phys.* **52** 7182 (1981).

[65] G.J.Martyna, M.J.Klein and M.Tuckerman, *J. Chem. Phys.* **97**, 2635 (1992).

[66] G.J.Martyna, D.J. Tobias and M.J.Klein, *J. Chem. Phys.* **101**, 4177 (1994).

[67] W. Smith and T.R. Forester, *J. Molec. Graphics* **14**, 136 (1996): W. Smith and T.R. Forester, DL_POLY Reference Manual.

[68] W.H.Press, B.P.Flannery, S.A.Teukolsky and W.T.Vetterling, *Numerical Recipes*, (Cambridge University Press, Cambridge, 1986).

[69] C.W.Gear, *Numerical Initial Value Problems in Ordinary Differential Equations*, Chapter 9, (Prentice-Hall, Englewood Cliffs, New Jersey, 1971).

[70] D.Fincham and D.M.Heyes, *Dynamical Processes in Condensed Matter, Advances in Chemical Physics vol. LXIII*, (Wiley, New York, 1985), p 493-575.

[71] W.Cochran, *The Dynamics of Atoms in Crystals*, volume 3 of *The Structure and Properties of Solids*, (Edward Arnold, London, 1973).

[72] J.M.Dickey and A.Paskin, *Phys. Rev.* **188**, 1407 (1969).

[73] G.H.Wannier, *Statistical Physics*, (Wiley, New York, 1966), p.479.

[74] R.Meyer and P.Entel, *Phys. Rev. B* **57**, 5140 (1998).

[75] G.L.Squires, *Introduction to the Theory of Thermal Neutron Scattering*, (Cambridge University Press, Cambridge, 1978).

[76] S.W.Lovesey, *The Theory of Neutron Scattering from Condensed Matter*, vol.1, (Clarendon, Oxford, 1984).

[77] W.Petry, A.Heiming, J.Trampenau, M.Alba, C.Herzig, H.R.Schöber and G.Vogl, *Phys. Rev. B* **43**, 10933 (1991).

[78] C.Stassis, J.Zarestky, D.Arch, O.D.McMasters and B.N.Harmon, *Phys. Rev. B* **18**, 2632 (1978).

[79] M.Born and K.Huang, *Dynamical Theory of Crystal Lattices*, (Clarendon Press, Oxford, 1954), p.213-225.

[80] G.J.Ackland, *Alloy Modelling and Design*, TMS93 proc., eds. G.M.Stocks and P.E.A.Turchi, 149 (1993).

[81] G.J.Ackland (Unpublished).

[82] D.Frenkel and B.Smit, *Understanding Molecular Simulation: from algorithms to applications*, (Academic Press, London, 1996), p.82.

[83] P.J.Craievich, J.M.Sanchez, R.E.Watson and M.Weinert, *Phys. Rev. B* **55**, 787 (1997).

[84] S.A.Ostanin, E.I.Salamatov and V.Yu.Trubitsin, *Phys. Rev. B* **57**, 5002 (1998).

[85] V.A.Chernenko, C.Seguí, E.Cesari, J.Pons, V.V.Kokorin, *Phys. Rev. B* **57**, 2659 (1998).

[86] M.L.Boas, *Mathematical Methods in the Physical Sciences*, 2nd ed. (J.Wiley and Sons Inc., Singapore, 1983), p.435-446.

[87] D.R.Lovett, *Tensor Properties of Crystals* (IOP, Bristol, 1994), p.50-70.

[88] A.Serra, R.C.Pond and D.J.Bacon, *Acta Metall. Mater.* **39**, 1469 (1991); A.Serra and D.J.Bacon, *Acta Metall. Mater.* **43**, 4465 (1995) and references therein.

[89] J.K.Liakos and G.A.Saunders, *Phil. Mag. A* **46**, 217 (1982).

[90] M.Igarashi, M.Khantha and V.Vitek, *Phil. Mag. A* **63**, 603 (1991).

[91] C.Kittel, *Introduction to Solid State Physics*, 6th ed. (J.Wiley and Sons Inc., New York, 1986).

[92] V.Vitek and M.Igarashi, *Phil. Mag. A* **63**, 1059 (1991).

[93] This is a numerical method to find a local minimum in multidimension problems, see also [68]. The method is powerful, fast and requires optimum computer resources, i.e. memory and CPU time. Moreover, it gives a high precision solution. This method cannot search for a global minimum. However, the local minimum solution is good enough for the purpose of determination of the microstructure.

[94] D.A.Porter and K.E.Easterling, *Phase Transformations in Metals and Alloys*, (Van Nostrand Reinhold (UK), Berkshire, 1984).

[95] V.Gerold, editor, *Structure of Solids*, volume 1 of *Materials Science and Technology: a comprehensive treatment*, (VCH, New York, 1993).

[96] M.H.Yoo and J.K.Lee, *Phil. Mag. A* **63**, 987 (1991).

[97] S.Naka, L.P.Kubin and C.Perrier, *Phil. Mag. A* **63**, 1035 (1991).

[98] A.Serra and D.J.Bacon, *Phil. Mag. A* **73**, 333 (1996).

[99] A.Serra and D.J.Bacon, *Phil. Mag. A* **63**, 1001 (1991).

[100] D.J.Bacon and A.Serra, *MRS Symposium* **Cb** (1991).

[101] M.A.Fradkin, *Phys. Rev. B* **50**, 16 326 (1994).

[102] G.R.Barsch and J.A.Krumhansl, *Phys. Rev. Lett.* **53**, 1069 (1984).

[103] A.Mazor and A.R.Bishop, *Phys. Rev. B* **40**, 5084 (1989).

[104] B.Horovitz, G.R.Barsch and J.A.Krumhansl, *Phys. Rev. B* **43**, 1021 (1991).

[105] A.E.Jacobs, *Phys. Rev. B* **52**, 6327 (1995).

[106] Ch.Maier, O.Blaschko and W.Pichl, *Phys. Rev. B* **55**, 12062 (1997).